Quantum Chemical Studies of Reaction Pathways and Thermophysical Properties of Materials

by

Minh Nguyen Vo

Bachelor of Science in Chemical Engineering, Bucknell University, 2014

Master of Science in Chemical Engineering, University of Pittsburgh, 2017

Submitted to the Graduate Faculty of the

Swanson School of Engineering in partial fulfillment

of the requirements for the degree of

Doctor of Philosophy

University of Pittsburgh

2020

UNIVERSITY OF PITTSBURGH

SWANSON SCHOOL OF ENGINEERING

This dissertation was presented

by

Minh Nguyen Vo

It was defended on

March 9, 2020

and approved by

J. Karl Johnson, Ph.D., William Kepler Whiteford Professor, Department of Chemical and Petroleum Engineering

John A. Keith, Ph.D, Associate Professor , Department of Chemical and Petroleum Engineering

Giannis Mpourmpakis, Ph.D., Associate Professor, Department of Chemical and Petroleum Engineering

Peng Liu, Ph.D., Associate Professor, Department of Chemistry

Cliff Kowall, PE, Department of Chemical and Petroleum Engineering

Dissertation Director: J. Karl Johnson, Ph.D., William Kepler Whiteford Professor, Department of Chemical and Petroleum Engineering

Quantum Chemical Studies of Reaction Pathways and Thermophysical Properties of Materials

Minh Nguyen Vo, PhD

University of Pittsburgh, 2020

Owing to developments in computer power and algorithmic efficiencies, quantum chemical methods have become essential tools for both fundamental scientific research and industrial problem solving. Quantum mechanics is routinely used in multiple industries including pharmaceuticals, polymers, specialty chemical production, and national defense. Knowledge of reaction pathways and material properties are essential for improving and developing new materials and processes. This dissertation consists of three major projects that employ quantum chemical methods to provide insight into important chemical and physical processes.

The first project elucidated the cationic polymerization mechanism of polyisobutylene. Polyisobutylenes have been produced industrially for over 60 years, but no validated molecular-level understanding of the reaction mechanism exists. With the aid of a powerful reaction pathway finding technique, the growing string method (GSM), we identified an initiator complex that produces low-energy barrier pathways for both initiation and propagation steps. Additionally, we found that it is the extreme acidity of the complex that is crucial for initiating the reaction of polyisobutylene.

The second project studied the reaction mechanism between dimethyl methyl phosphonate (DMMP), a chemical warfare agent (CWA) simulant and different Zr_6-based metal-organic frameworks (MOFs). It has been shown experimentally that MOFs containing zirconium secondary building units (SBUs), such as $Zr_6O_4(OH)_4$ found in UiO-67 and related MOFs, are highly active for neutralizing both DMMP and actual CWAs. We used both fully periodic models and cluster models to study reaction pathways on UiO-67 with multiple defects per SBU. We found that multiple defects can dramatically lower the reaction barrier for DMMP decomposition. Additionally, we found that UiO-67 with multiple defects has lower reaction barriers than Zr-based MOFs having zirconium sites that are inherently undercoordinated due to a lower number of linkers per SBU.

In the third project, we presented a formalism for accurate estimation of dipole moments for complex molecules having conformational degrees of freedom. Dipole moments of complex molecules are often needed for use in correlations for estimating viscosities and other thermophysical properties. We showed that proper accounting of the conformation-dependent dipole moment may be required to achieve an acceptably accurate estimate of the experimental dipole moment.

Table of Contents

1.0 Introduction 1

1.1 Polymerization of Isobutylene 2

1.2 Hydrolysis of CWA simulants with Zr-based MOF 4

1.3 Dipole Moment Estimation for Complex Molecules 6

2.0 The Mechanism of Isobutylene Polymerization 8

2.1 Introduction 8

2.2 Calculation Method 9

2.2.1 Electronic Structure Calculations 9

2.2.2 Reaction Pathway Search and Activation Energies Estimation 10

2.2.3 Ab Initio Molecular Dynamic (AIMD) Simulations 11

2.3 Reaction Pathway with $AlCl_3OH_2$ 12

2.4 Reaction Pathway with $AlCl_3HOHAlCl_3$ 15

2.4.1 Initiation Reaction 15

2.4.2 Propagation Reaction 18

2.4.3 AIMD Simulations 21

2.5 Conclusion 22

3.0 Impact of Defects on the Decomposition of Chemical Warfare Agent Simulants in Zr-based Metal Organic Frameworks 24

3.1 Introduction 24

3.2 Method 26

3.3 Hydrolysis of DMMP with Defective UiO-67 28

3.3.1 1-missing linker defect 28

3.3.2 2-missing linker defect 32

3.4 Hydrolysis of DMMP with Inherently Undercoordinated Zr-based MOF............ 34

3.5 Conclusion 37

4.0 Method for Predicting Dipole Moments of Complex Molecules for Use in Thermophysical Property Estimation 38

4.1 Introduction 38

4.2 Method 40

4.2.1 Electronic Structure Calculations 40

4.2.2 Conformer Generations...41

4.2.3 AIMD Simulations 41

4.2.4 Gas-phase Viscosity and Thermal Conductivity Estimation 42

4.3 Basis Set and Level of Theory 42

4.4 Conformational Effects 44

4.5 AIMD Simulation 48

4.6 Thermophysical Properties Estimation 54

4.6.1 Vapor Viscosity 54

4.7 Conclusion 59

5.0 Future Work 61

5.1 Investigate the effect alkyl chain length on dipole moment of aliphatic oligomers 61

6.0 Summary of Publications from Ph.D. 65

6.1 Published Work 65

6.2 Manuscript in preparation 65

Appendix A Mechanism of Isobutylene Polymerization 66

Appendix A.1 Theory and Basis Set Comparison 66

Appendix A.2 Bond Distances 70

Appendix A.3 Propagation Reaction with $AlCl_3OH_2$ 71

Appendix A.4 Reaction Pathway with $AlCl_3/H_2O$ Complexes 72

Appendix A.5 Propagation Reaction Pathway with Complex 1 via Syn-addition 75

Appendix A.6 Reaction Pathway of IB + IBH^+ 76

Appendix A.7 pK_a Comparison 77

Appendix A.8 AIMD Simulation Summary 79

Appendix A.9 Coordinates of Initiator Complex 80

Appendix B Impact of Defects on the Decomposition of Chemical Warfare Agent Simulants in Zr-based Metal Organic Frameworks 82

Appendix B.1 Reaction in Periodic System 82

Appendix B.1.1 1-defect UiO-67 82

Appendix B.1.2 2-defect UiO-67 83

Appendix B.2 PCN-700 Topology 84

Appendix C Method for Predicting Dipole Moments of Complex Molecules for Use in Thermophysical Property Estimation 86

Appendix C.1 CONFAB Modification 86

Appendix C.2 Dimethyl Carbonate Bond Rotation Energy 87

Appendix C.3 AIMD Results 88

Appendix C.4 Thermophysical Properties 90

Bibliography 98

List of Tables

Table 1. Comparison of calculated vapor phase dipole moment (units in Debye) with data from the NIST database 44

Table 2. Boltzmann averaged dipole moments and dipole moments of the lowest-energy structure and their errors (units in Debye) 49

Table 3. Summary of dipole moments computed from con-formers generated from AIMD simulations, com-pared with experiments and computed values from the BWA and LES methods (units in Debye) 51

Table 4. Summary of mean average error of thermal conduc-tivity estimation when using μ = BWA and μ = 0........ 59

Appendix Table 1. Summary of ΔE_a and ΔE_{rxn} (kJ/mol) at different levels of theory 68

Appendix Table 2. pK_a for initiator complexes studied........ 77

Appendix Table 3. Summary of isothermal-isochoric ensemble simulation performed with different initiator complexes 79

Appendix Table 4. Estimated Vapor Viscosities (cP) from the Lucas method 90

Appendix Table 5. Vapor viscosities (cP) computed from the Chung et al. method 92

Appendix Table 6. Vapor viscosities (cP) computed from the Reichenberg method 93

Appendix Table 7. Vapor viscosities (cP) computed from the Chapman et al. method........ 95

Appendix Table 8. Estimated Thermal Conductivity (10^{-3} $Wm^{-1}K^{-1}$) calculated from the Chung et al. method........ 96

List of Figures

Figure 1. a) Terminal group of conventional PIB when catalyzed with AlCl3 and b) high reactive PIB terminal group when catalyzed with BF3. 3

Figure 2. The putative initiator complex, $AlCl_3OH_2$. 12

Figure 3. Potential energy surface for the initation reaction with $AlCl_3OH_2$. 14

Figure 4. Identified initiator complex, $AlCl_3HOHAlCl_3$, denoted as 1. 16

Figure 5. Potential energy surface for the IB initiation reaction with 1. 17

Figure 6. Potential energy surface for the first propagation reaction starting from 1 as the initiator complex. 19

Figure 7. Potential energy surface for the second propagation reaction with 1. 20

Figure 8. Summary of the propsed initiation and propagation mechanism with 1 21

Figure 9. AIMD simulation snapshots showing the progression of the initiation reaction of IB with 1 from Figure 4. The proton of interest is colored blue for clarity and non-reacting IB molecules shown as stick models. 22

Figure 10. Cluster energy reaction paths for DMMP hydrolysis via adjacent OH elimination with one missing linker defect UiO-67 computed from different levels of theory and energies reported by Wang et al.[14] 29

Figure 11. Transition state (TS) and product state (PS) of defective UiO-67 pathways. (a) TS and (b) PS of 1-defect adjacent OH elimination. (c) TS and (d) PS of 1-defect μ_3-OH elimination. (e) TS and (f) PS of 2-defect μ_3-OH elimination. 31

Figure 12. Lowest cluster energy pathways for DMMP hydrolysis on defective UiO-67 computed at BP86/def2-TZVP//BP86/def2-TZVP. 33

Figure 13. Lowest energy pathways of DMMP hydrolysis on cluster models of pristine PCN-700 and MOF-808 computed at BP86/def2-TZVP. The pathway for the 2-defect UiO-67 is also shown for comparison. 35

Figure 14. Transition state (TS) and product state (PS) of pristine PCN-700 and MOF-808 shown in Figure 13. (a) TS and (b) PS of PCN-700 μ_3-OH elimination. (c) TS and (d) PS of MOF-808 μ_3-OH elimination. 36

Figure 15. Two conformations of octanoic acid having very different dipole moments. 40

Figure 16. Benchmark molecules with available experimental dipole moments examined in this work. 43

Figure 17. Molecules studied in this work. Condensed phase species refer to molecules with only experimental condensed phase dipole moment reported in the literature. 46

Figure 18. Comparison of Boltzmann averaged dipole moments and dipole moments of the CONFAB generated lowest-energy structure to experimentally measured dipole moments for a) vapor phase and b) condensed phase molecules. 47

Figure 19. Two major conformations of dimethyl carbonate. 50

Figure 20. (a) RMSD of structures of di-n-propyl ether with respect to lowest energy structure generated by CONFAB (b) with respect to an arbitrary structure generated by CONFAB (1.05 D, ΔE = 4.5 kJ/mol) 53

Figure 21. (a) Mean absolute error in the viscosities calculated from the Lucas method using BWA calculated dipole moments and $\mu = 0$. The viscosities computed using the experimental dipole moments were used as reference. (b) Comparison of reduced dipole moments as defined by Lucas method. Dashed lines mark the boundary limits in the piece-wise function for $Fp°$ in eq (2) of μr = 0.022 and 0.075. Molecules evaluated (ordered in

increasing dipole moment) are: dimethyl carbonate, diethyl carbonate, diethyl ether, dimethyl ether, methyl acetate, ethyl acetate, and methyl ethyl ketone. 56

Figure 22. Comparison of experimental and calculated vapor viscosities (in micropoise, µP) for selected molecules. Vapor viscosities are reported at specific temperature based on literature values: Methyl acetate (125, 200°C), dimethyl ether (20, 100°C), diethyl ether (125, 200, 300°C), and ethyl acetate (125, 200, 300°C) 58

Figure 23. Structure of PIBSA.. 62

Figure 24. Dipole monent of PIBSA for n = 0 to n = 9.. 63

Figure 25. Dipole distribution for PIBSA with different chain length. n = 0, 2, 4, 6, 8, and 9 64

Appendix Figure 1. Potential energy surfaces (PES) for the initiation reaction with complex 1 at different level of theory and basis sets for double-ended GSM, and post-GSM single-point energy calculations. 66

Appendix Figure 2. a) PES for the formation of complex 1 at BP86/6-31G** and b) at different levels of theory 67

Appendix Figure 3. PES for the initiation reaction with $AlCl_3OH_2$ at different levels of theory 67

Appendix Figure 4. Labeled bond distance structure of a) tert-butanol, b) $(AlCl_3OH)(IBH)$ complex , and c) complex 1. All bond distances are in Å. C-H bond distances are omitted. 70

Appendix Figure 5. Potential energy surface (PES) for the propagation reaction with $AlCl_3OH_2$. E_a = 217.2 kJ/mol E_{rxn} = -31.3 kJ/mol 71

Appendix Figure 6. PES for the initiation reaction with $AlCl_3(OH_2)_2$................................. 72

Appendix Figure 7. PES for the initiation reaction with $AlCl_3(OH_2)_6$. 73

Appendix Figure 8. PES for the initiation reaction with $(AlCl_3)_2OH_2$. E_a = 80.3 kJ/mol E_{rxn} = -35.2 kJ/mol. 73

Appendix Figure 9. PES for the initiation reaction with $(AlCl_3)_3OH_2$. E_a = 86.8 kJ/mol E_{rxn} = -20.1 kJ/mol 74

Appendix Figure 10. PES for the initiation reaction with $(AlCl_3)_4OH_2$. E_a = 68.6 kJ/mol E_{rxn} = -8.8 kJ/mol 74

Appendix Figure 11. PES for the propagation reaction via syn-addition with complex 1. E_a = 14 kJ/mol and E_{rxn} = -46.0 kJ/mol 75

Appendix Figure 12. PES for the reaction of IB + IBH^+ 76

Appendix Figure 13. Cluster and periodic energy reaction paths for DMMP hydrolysis via adjacent OH elimination with one missing linker defect UiO-67 82

Appendix Figure 14. Cluster and periodic energy reaction paths for DMMP hydrolysis via µ3-OH elimination with 2-defect UiO-67 83

Appendix Figure 15. Topology of pristine PCN-700. Dotted blue outlines show pairs of OH and water molecules occupy the undercoordinated sites. Shaded yellow areas show the location that DMMP would adsorb to reaction with the OH groups (shaded blue) to follow the 2-adjacent missing linker UiO-67 pathway. The shaded green area shows the linkers that sterically hinder the 2-djacent missing linker pathway. 84

Appendix Figure 16. Potential energy surface of rotating the methyl group in dimethyl carbonate along the dihedral angle to transform cis-cis to cis-trans configuration. 87

Appendix Figure 17. Distribution of dimethyl carbonate dipole moment from AIMD simulation. (a) starting with cis-cis configuration (b) cis-trans configuration 88

Appendix Figure 18. Distribution of diethyl carbonate dipole moment from AIMD simulation(a) starting with cis-cis configuration (b) cis-trans configuration 88

Appendix Figure 19. Distribution of di-n-propyl ether dipole moment from AIMD simulation 89

Appendix Figure 20. Distribution of sulfurous acid dimethyl ester dipole moment from AIMD simulation 89

1.0 Introduction

Owing to developments in computer power and algorithmic efficiencies, quantum chemical methods have become essential tools for both fundamental scientific research and industrial problem solving. Quantum mechanics is routinely used in multiple industries including pharmaceuticals, polymers, specialty chemical production, and national defense. This dissertation will showcase the application of quantum chemical methods for studying catalysis and predicting important physical and chemical properties through three different projects. The first project goal is to understand the polymerization reaction mechanism of isobutylene with aluminum trichloride ($AlCl_3$). The second project focuses on understanding the role of defects in Zr-based metal organic frameworks (MOFs) for neutralizing chemical warfare agent (CWA) simulants. The last project is the development of a formalism for accurate dipole moment estimation using quantum mechanics coupled with conformational sampling for complex molecules.

Quantum chemical methods are useful for studying reaction mechanisms. They are often used in conjunction with transition state (TS) locating methods to estimate elementary reaction barriers and provide insight into reaction mechanisms at the molecular level. Two commons TS locating methods are the single-ended and the double-ended growing string methods (GSM)[1-3]. The single-ended growing string method systematically adjusts geometries of reactants until they reach the TS. Once the TS is found, additional nodes are added to locate the product state. The double-ended method relies on the input of the initial and final states to construct a reaction pathway that is connected by a TS. Single-ended methods are extremely useful for studying reaction mechanism because they do not require the knowledge of the end products. GSM was used extensively to study the reaction mechanism of isobutylene polymerization and the decomposition of DMMP on Zr-based MOFs.

1.1 Polymerization of Isobutylene

The production of polyisobutylene with Lewis acid catalysts has been in wide-spread use for over 60 years, but no validated molecular-level understanding of the reaction mechanism exists. Polyisobutylene are typically produced through cationic polymerization. Cationic polymerization typically involves the use of a Lewis acid as the catalyst (e.g., $AlCl_3$, BF_3, $TiCl_4$).[4] Another important component is the proton donor, such as water, hydrogen halide, or alcohol. The choice of catalyst can greatly affect the terminal groups on PIBs. The $AlCl_3$-catalyzed process produces conventional PIBs, which contain up to 90% of internal double bond end groups (trisubstituted, tetrasubstituted), shown in Figure 1a. In contrast, the BF_3-catalyzed process produces PIBs having a high content of terminal vinylidene (exo) groups, shown in Figure 1b. PIBs having a high percentage of exo groups are known as highly reactive (HR) PIBs. With the terminal vinylidene group, HR PIBs react readily with maleic anhydride to form PIB succinic anhydride, which can react with oligoalkylenamines to produce dispersants.[5-6] Conventional PIBs have low reactivity because of the internal double bond and therefore require a promoter (e.g., Cl_2) to react with maleic anhydride.

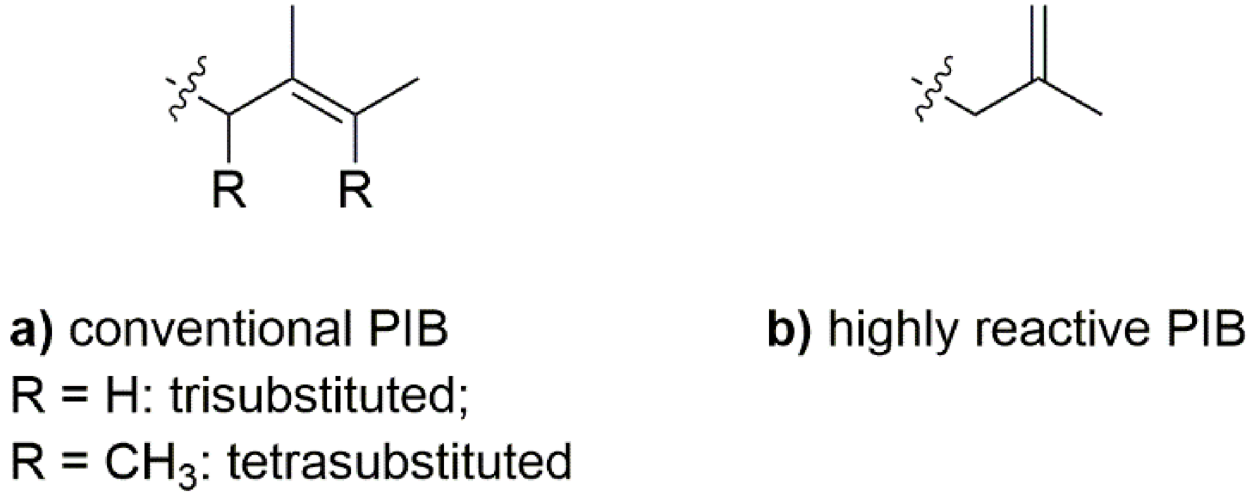

a) conventional PIB
R = H: trisubstituted;
R = CH_3: tetrasubstituted

b) highly reactive PIB

Figure 1. a) Terminal group of conventional PIB when catalyzed with AlCl3 and b) high reactive PIB terminal group when catalyzed with BF3.

It is well known that neat $AlCl_3$ and BF_3 are not active initiators. The presence of adventitious water or another proton donor is essential for catalyzing the polymerization reaction.[5-8] The putative mechanism reported in the literature proceeds as follows:[4, 6, 9-10]

$$\mathrm{AlCl_3 + H_2O \rightleftharpoons AlCl_3 \cdot OH_2} \tag{1-1}$$

$$\mathrm{AlCl_3 \cdot H_2O +\ (CH_3)_2CCH_2\ \longrightarrow (CH_3)_3C^+(AlCl_3OH)^-} \tag{1-2}$$

$$\begin{aligned}&\mathrm{[(CH_3)_3C(CH_2C(CH_3)_2)_{\mathit{n}}]^+(AlCl_3OH)^- + (CH_3)_2CCH_2}\\ &\quad \rightarrow \mathrm{[(CH_3)_3C(CH_2C(CH_3)_2)_{\mathit{n}+1}]^+(AlCl_3OH)^-}\end{aligned} \tag{1-3}$$

The first step in this process involves a reaction between a Lewis acid ($AlCl_3$) and a proton donor (H_2O) to form the initiator complex ($AlCl_3OH_2$), which is often represented as $[H]^+[AlCl_3OH]^-$. Consequently, $AlCl_3OH_2$ is believed to be the active catalyst. Next, the initiator complex donates a proton to an isobutylene (IB) to form the t-butyl cation (IBH^+) and the counterion ($AlCl_3OH^-$), as indicated in Eq. 2. The reaction propagates as additional IBs are added to the chain, as shown in Eq. 3. The termination step can occur through chain breaking or chain transfer, depending on the operating temperature and choice of catalyst.[11]

We have computed initiation and propagation reaction pathways for isobutylene polymerization with an $AlCl_3/H_2O$ initiator from density functional theory (DFT) calculations. The initiator/catalyst complex we identified is fundamentally different from the putative complex identified in the literature, which typically assumes that the $AlCl_3OH_2$ complex is the active catalyst. We found that the reaction pathway with the $AlCl_3OH_2$ complex is infeasible due to unreasonably high-energy barriers. Our calculations indicate that a minimum of two $AlCl_3$ groups and one H_2O molecule is required to initiate the reaction and that the complex must produce a highly acidic proton. It is the extreme acidity of the complex that is crucial for successful initiation of the reaction. The active catalyst moiety we identified produces low-energy barrier pathways for both initiation and propagation steps. This complex was identified using the growing-string method to identify possible reaction pathways with various $AlCl_3/H_2O$ complexes. The initiation reaction with our proposed complex was observed to occur naturally in an ab initio molecular dynamics simulation under typical operating conditions, confirming the activity of the complex. The results are discussed in Chapter 2.

1.2 Hydrolysis of CWA simulants with Zr-based MOF

Designing and developing new material for decomposition of CWA is one of the top priorities for the military. MOF, a novel class of material, is a potential promising solution for decomposing CWA.[12-13] An advantage of MOFs is that their properties can easily be tuned by changing the metal-containing secondary building unit (SBU) and the organic linkers to serve different applications. In the area of neutralizing CWA, Zirconium-based MOFs have received `most attention because they showed fast decomposition of organophosphorus compounds that mimic nerve agents. Dimethyl methyl phosphonate (DMMP) is widely used experimentally as a key CWA simulant. It has been reported that UiO-67 MOF can decompose DMMP into less harmful methyl phosphonic acid (MMPA). The motivation for this work comes from two opposing experimental observations of reaction between DMMP and UiO-67 at similar experimental conditions. Wang and colleagues observed[14] reaction between DMMP and UiO-67 under ultra-high vacuum environment. Ruffley and colleagues,[15] however, did not observe any reaction under similar conditions. It is known that missing linker defects are required for the reaction to proceed in UiO-67 because the UiO series has 12 linkers per SBU, which fully coordinate the zirconium atoms. However, it is not known if a single isolated missing linker defect is sufficient to produce low-barrier pathways, or if multiple defects are required for facile decomposition of DMMP and CWAs in this material. The differences from the two experiments may due to the different concentrations and types of defects in the sample. Studying the reaction mechanism of Zr-based MOF and DMMP at molecular level will provide valuable insights and aid the advancement of MOF design for decomposing CWA. We use both fully periodic models and cluster models to study reaction pathways on UiO-67 with multiple defects per SBU. We find that multiple defects can dramatically lower the reaction barrier for DMMP decomposition. Additionally, we find that UiO-67 with multiple defects has lower reaction barriers than undercoordinated Zr-based MOFs having zirconium sites that are inherently undercoordinated due to a lower number of linkers per SBU. We have specifically examined PCN-700 and MOF-808, which have similar numbers of undercoordinated zirconium atoms compared with defective UiO-67. Hence, we conclude that the topology of the open metal sites, in addition to the number of sites, is an important parameter in controlling the reaction barrier, at least under UHV conditions. The results for this work are discussed in Chapter 3.

1.3 Dipole Moment Estimation for Complex Molecules

The knowledge of thermophysical properties for a wide range of molecules is also crucial for industrial applications. Vapor viscosity and thermal conductivity, for example, are essential parameters for sizing equipment including but not limited to pipeline, compressor, and heat exchanger. However, such properties are often not available for many species of interest, especially for proprietary compounds. Experimental measurement is expensive and time-consuming. Thermophysical property estimation methods are available[16-17] that depend in part on the value of the gas phase dipole moment, which is also difficult to measure experimentally. The motivation of this work is to develop a systematic procedure to accurately calculate the gas phase dipole moment for molecules so that it could be used for estimating thermophysical properties of materials. It has been shown that quantum chemical methods such as density functional theory (DFT) can be used to accurately estimate the dipole moment vector for simple molecules[18-19]. In DFT, the dipole moment vector, $\boldsymbol{\mu}$, is calculated using the following equation:

$$\boldsymbol{\mu} = \int_V \boldsymbol{r}\rho(\boldsymbol{r})d\boldsymbol{r} \tag{1-4}$$

Where $\boldsymbol{r}$ is the vector spatial coordinate over all volume, V, and $\rho(\boldsymbol{r})$ is the charge density at position $\boldsymbol{r}$, which is computed from the Kohn-Sham orbitals. However, dipole moments for molecules having a large number of conformational degrees of freedom have been very challenging to calculate. This is because the conformation of the molecule can greatly affect its dipole moment. Molecular conformations can be efficiently explored through a variety of methods (e.g., ab initio molecular dynamics, random configuration generation, etc.). The goal of this work is to assess the accuracy of different computational methods to calculate the gas phase dipole moment of molecules for use in thermophysical property estimation. We show that proper accounting of the conformation-dependent dipole moment may be required to achieve an acceptably accurate estimate of the experimental dipole moment and provide recommendations on efficient estimation techniques. We also demonstrate that for molecules with dipole moments above about 1.3 Debye reasonably accurate estimation of the dipole moment is required for reliable prediction of vapor phase viscosity, whereas estimation of thermal conductivity is less sensitive to the dipole moment. The results are discussed further in Chapter 4.

2.0 The Mechanism of Isobutylene Polymerization

This work was published as: Vo, M. N.; Basdogan, Y.; Derksen, B. S.; Proust, N.; Cox, G. A.; Kowall, C.; Keith, J. A.; Johnson, J. K (2018). Mechanism of Isobutylene Polymerization: Quantum Chemical Insight into $AlCl_3/H_2O$-Catalyzed Reactions. ACS Catal. 8, 8006-8013

2.1 Introduction

Polyisobutylenes (PIBs) are highly versatile materials, having properties that can be tuned for specific applications by varying the molecular weight (M_n) and chain termination. High molecular weight PIBs ($M_n > 10^5$ g mol^{-1}) have high viscosity and are commonly used for the synthesis of rubber products, such as chewing gum and car tires. Medium molecular weight PIBs ($5 \times 10^3 < M_n < 3 \times 10^4$ g mol^{-1}) vary from viscous liquid to tacky semisolids and can be found in sealant and caulking products. Low molecular weight PIBs ($M_n < 5 \times 10^3$ g mol^{-1}) are used as precursors for making adhesives and lubricants, and as additives for motor oils and fuels. PIBs are produced through exothermic cationic polymerization. The molecular weight distribution is typically controlled through the reaction temperature. Low molecular weight PIBs are polymerized between -40 to 10°C and high molecular weight PIBs require even lower temperatures of about -100 to -90°C.[20]

PIBs have been produced industrially for over 60 years, but no validated molecular-level understanding of the reaction mechanism exists. To the best of our knowledge, there is only one molecular-level study of the cationic polymerization of IB in the literature. Chaffey-Millar and

Kühn studied the PIB initiation mechanism with manganese complexes as catalysts using density functional theory coupled with second order Møller-Plesset (MP2) perturbation theory to compute reaction pathways and barriers.[21] However, that study failed to identify any feasible pathways for the proposed initiation mechanisms. In this work, we will show that a complex of one $AlCl_3$ and one H_2O cannot be the active catalyst for IB polymerization, in contradiction to the putative mechanism. More importantly, we have identified an initiator complex consisting of two $AlCl_3$ groups combined with one H_2O that facilitates low-barrier reaction pathways for both the initiation and propagation steps in the polymerization of IB. Crucially, this complex contains a highly acidic proton that gives an acceptably low barrier to the initiation reaction. It is the extreme acidity of the complex that is the distinguishing characteristic of a viable catalyst; this super acidity requirement has been overlooked in describing the reaction pathway for Lewis acid cationic polymerization until now.

2.2 Calculation Method

2.2.1 Electronic Structure Calculations

Electronic structure calculations were performed with the ORCA program.[22] Optimizations were performed at the BP86[23]/def2-SVP[24] level of theory with the RI-J approximation[25] and Grimme's D3 dispersion corrections.[26] Frequency calculations were performed at the same level of theory and basis set to verify that initial and final state geometries were at local minima, that the transition state had only one imaginary frequency, and to compute zero point energies and thermal corrections. Vibrational frequencies lower than 60 cm^{-1} were raised to 60 cm^{-1}, following the approximation proposed by Truhlar et al.[27] to correct for the well-known breakdown of the harmonic oscillator model for free energies of low-frequency vibration modes. Single-point energy calculations were performed using the BP86/def2-TZVP[24] level of theory.

The gas phase Gibbs free energy (G_g) for each species at T = 298 K was computed from

$$G_\mathrm{g} = E_\mathrm{SCF} + ZPE + \Delta H_{0\rightarrow 298} - TS \tag{2-1}$$

Where E_SCF is the single-point electronic energy calculated from Kohn-Sham density functional theory (DFT) or a higher level of theory, ZPE is the zero-point energy, $\Delta H_{0\rightarrow 298}$ is the change in enthalpy due to changing the temperature from 0 to 298 K, and S is the entropy at 298 K and a pressure of 1 bar. All calculations used the standard ideal gas, rigid rotor, and harmonic oscillator approximations. The polymerization reaction often takes place in pure IB or in a mixture of C4 olefins, which are non-polar organic solvents.[28] The dielectric constants for these solvents are very small (e.g., butane $\varepsilon = 1.4$). Thus, gas phase reaction free energies ($\varepsilon = 1$) were used to approximate the thermodynamics of the actual process.

2.2.2 Reaction Pathway Search and Activation Energies Estimation

The growing string method (GSM), a transition state locating technique developed by Zimmerman,[1-3] was used to identify reaction pathways. GSM calculations were performed with ORCA using the BP86 functional with D3 dispersion correction, and with the 6-31G** basis set[29-30] to provide the quantum mechanical gradients. We found that the single-ended GSM is a useful tool for identifying potential reaction pathways because it does not require the user to know the configuration of the product of the reaction and only takes the reactant configuration and a set of bonds to break and/or form as the input. The product configurations typically identified with single-ended GSM were not at local minima. Consequently, the product configurations were optimized in ORCA with the same functional and basis set and used as inputs in the double-ended GSM method to generate the potential energy surfaces reported here. Single-point energy calculations on GSM reaction coordinates were performed using the BP86/def2-TZVP model chemistry. We have also computed single point energies on some reaction pathways using the B3LYP functional and MP2. These results are compared with the BP86 results in Figures 25-27, and Appendix Table 1 of Appendix A. Overall, the trends predicted from PB86 are in reasonable agreement with those computed from higher levels of theory.

2.2.3 Ab Initio Molecular Dynamic (AIMD) Simulations

Born-Oppenheimer AIMD simulations were performed with the CP2K software package,[31] using the QUICKSTEP method[32] and a timestep of 0.5 fs. We used the Perdue-Burke-Ernzerhof (PBE) generalized gradient functional.[33] Goedecker-Teter-Hutter (GTH) pseudopotentials[34-35] and short range double-ζ basis sets with polarization[36] were employed. Grimme's D3 dispersion correction[26] was included. Periodic unit cells containing up to 10 IBs and various initiator complexes were created. The systems were equilibrated for 10-15 ps in the isothermal-isobaric ensemble to achieve liquid densities consistent near experimental conditions. The barostat was set at 10 bar and the Nosé thermostat[37] was set at 300 K. The equilibrated configuration was then used to perform isothermal-isochoric ensemble simulations of about 15 ps at 300 K, with some simulations at elevated temperatures (up to 1500 K).

2.3 Reaction Pathway with $AlCl_3OH_2$

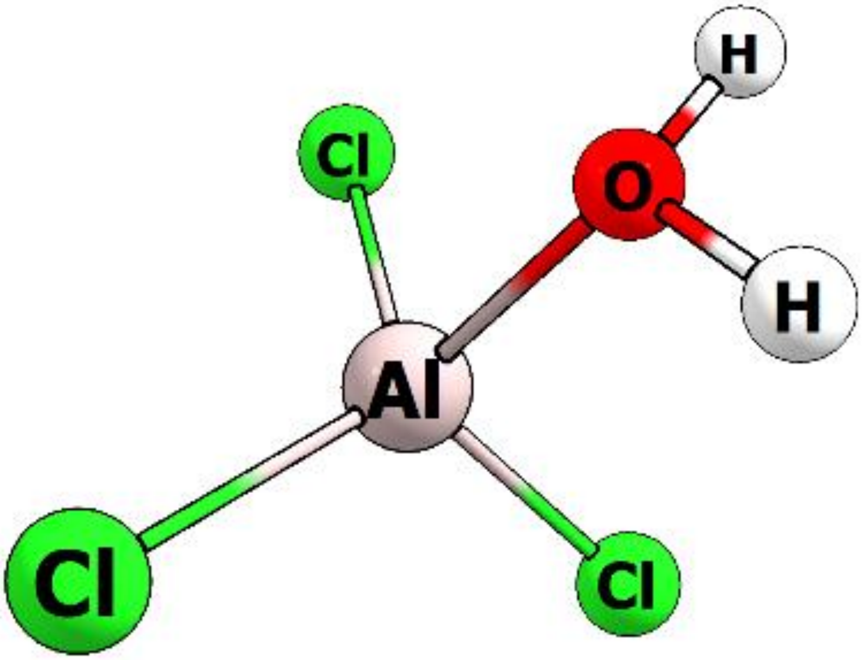

Figure 2. The putative initiator complex, $AlCl_3OH_2$.

The putative initiator complex most commonly identified in the literature is $AlCl_3OH_2$, which consists of one molecule of $AlCl_3$ and one molecule of H_2O.[4, 9, 38] The most energetically favorable complex of $AlCl_3OH_2$ is shown in Figure 2. The Al-O bond is a dative bond (1.96 Å), as the oxygen atom shares its lone pair of electrons with the empty orbital on the Al atom. The gas-phase Gibbs free energy of binding of the $AlCl_3OH_2$ complex relative to separated $AlCl_3$ and H_2O at 298 K [$\Delta G_{gas}(AlCl_3OH_2)$] is -97.6 kJ/mol. We have identified reaction pathways for the initiation reaction of IB with $AlCl_3OH_2$ using the single-ended GSM method, refining the best pathway using double-ended GSM. The potential energy surface for the initiation reaction generated with the double-ended GSM is shown in Figure 3. The initiation reaction proceeds by proton transfer from the H_2O group to the IB to form the IBH^+ cation. After the proton transfer, the newly formed t-butyl carbocation and the OH^- group form a C-O bond, as shown in the inset to Figure 3, to mitigate charge separation. As the polymerization reaction occurs very rapidly at low temperature, one would expect the initiation reaction to have a relatively low activation barrier ($E_a = E_{TS} - E_{IS}$, where TS and IS stand for transition and initial states, respectively). However, our calculated value at zero Kelvin is $E_a = 90.3$ kJ/mol, which is substantially higher than would be expected for a reaction that is rapid at low temperatures. The high E_a calculated for this initiator complex implies that the reaction rate would be extremely small at operating conditions. We stress that the pathway we have identified is the best pathway we found after extensive testing, including many GSM calculations and AIMD simulations at various temperatures for one $AlCl_3$ and one H_2O molecule. The overall reaction is exothermic with the reaction energy (ΔE_{rxn}) value of -39.8 kJ/mol at 0 K. This large exothermic value is a result of the formation of a strong C-O bond between the IBH^+ and the resulting anion. This C-O bond distance (1.51 Å) is similar to the C-O bond in tert-butanol (1.44 Å). Meanwhile, the Al-O bond remain a dative bond and is slightly shortened to 1.93 Å, relative to the Al-O bond in $AlCl_3OH_2$ of 1.96 Å. This indicates that tert-butanol is an intermediate product for this reaction pathway. As we shall see, the formation of tert-butanol impedes the polymerization reaction. For the propagation reaction to occur, the C-O bond must first be broken, resulting in an even larger reaction barrier of 217 kJ/mol, shown in Appendix Figure 5 in Appendix A. This very high barrier is inconsistent with the observed reaction rate at process conditions. Given that we investigated all combinations of $AlCl_3$ interacting with a single water molecule, we conclude that a complex consisting of only one $AlCl_3$ molecule and one H_2O molecule cannot be the correct initiator complex. We have also studied the reaction pathway with additional explicit water molecules but did not find any feasible pathways (See Appendix Figure 6 & 7 in Appendix A).

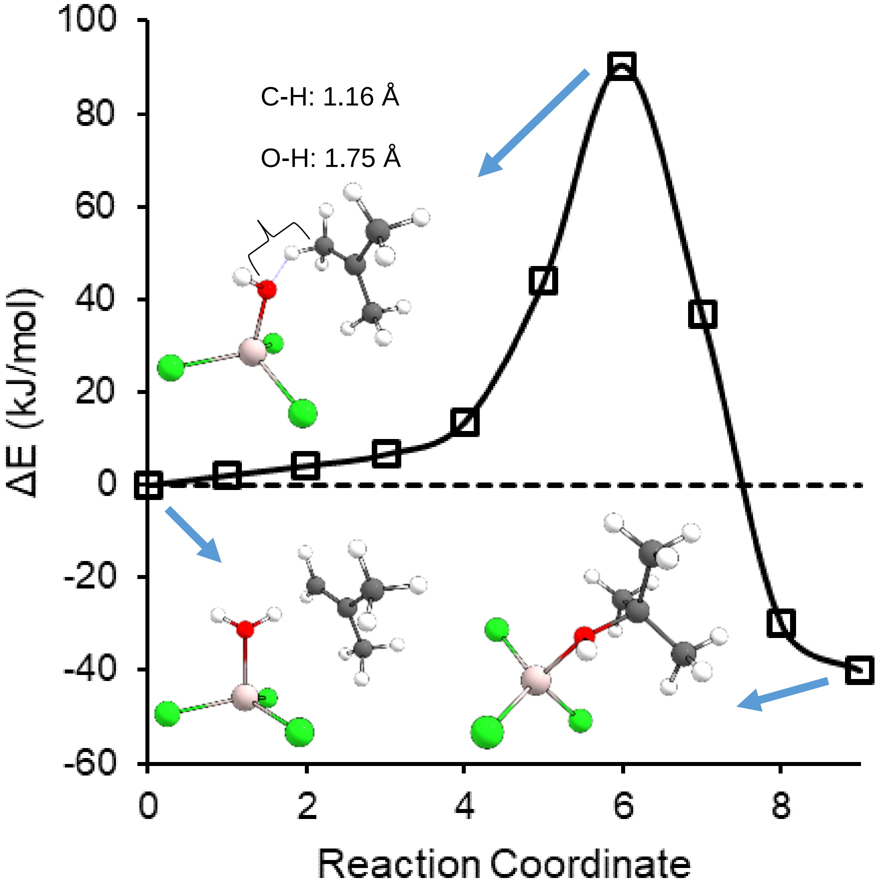

Figure 3. Potential energy surface for the initation reaction with $AlCl_3OH_2$

2.4 Reaction Pathway with $AlCl_3HOHAlCl_3$

2.4.1 Initiation Reaction

Having established that the putative initiator complex is not correct, we examined multiple $(AlCl_3)_n/(H_2O)_m$ complexes, where n is the number of $AlCl_3$ units and m is the number of water molecules in a complex (see Figures 30 - 34 in Appendix A). We considered n=1 to 3 and up to m=6. Among all the complexes we studied, we found that $AlCl_3HOHAlCl_3$, complex **1**, as identified in Figure 4, gave the lowest barrier pathways for both initiation and propagation steps for IB polymerization. The calculated $\Delta G_{gas}(AlCl_3HOHAlCl_3)$ value at 298 K is -165 kJ/mol, which indicates that $AlCl_3HOHAlCl_3$ is thermodynamically more stable than $AlCl_3OH_2$ (ΔG_{gas} = -97.6 kJ/mol). The reaction barrier of formation of **1** from $AlCl_3OH_2 + AlCl_3$ is 28.6 kJ/mol (see Appendix Figure 2 of Appendix A). This initiator complex has an OH^- group held between two $AlCl_3$ molecules and a proton weakly bound to chlorine atoms on each $AlCl_3$ group (Figure 4). Al-O bond distances in **1** are 1.87 and 1.86 Å. Refer to Appendix Figure 4 in Appendix A for bond distances for complex **1**.

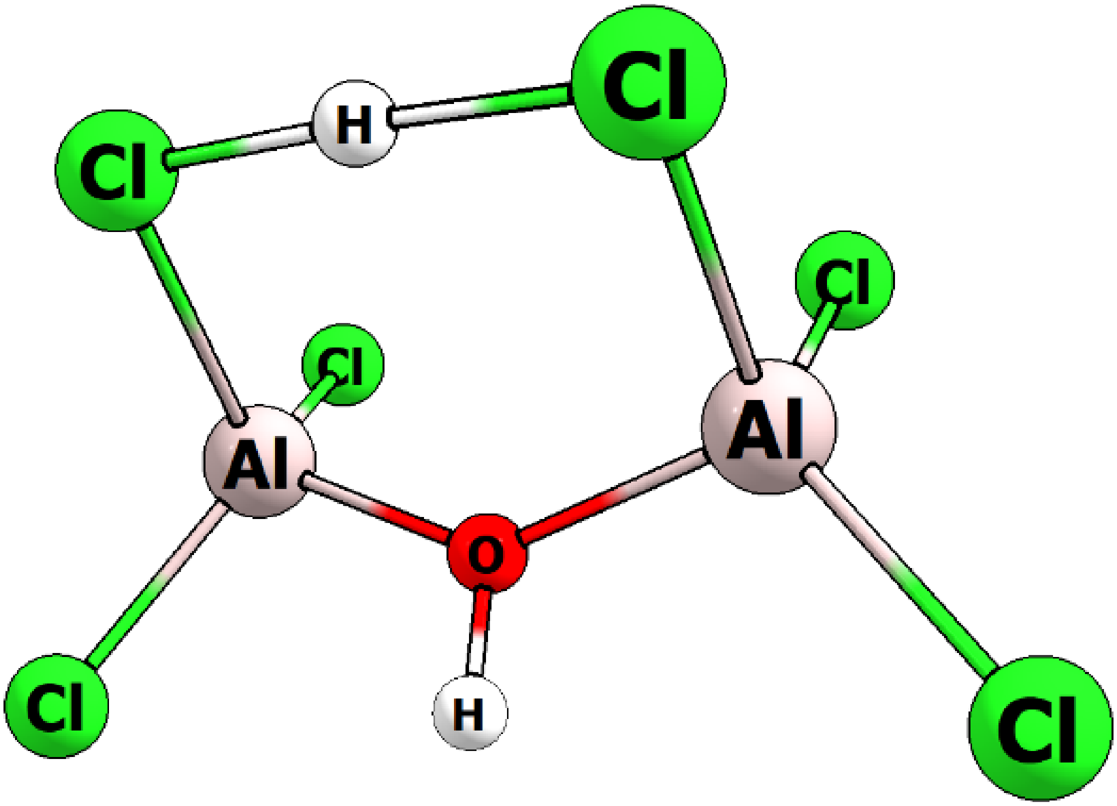

Figure 4. Identified initiator complex, $AlCl_3HOHAlCl_3$, denoted as 1.

The initiation reaction pathway with **1** is shown in Figure 5. The reaction proceeds as the proton rotates toward the alkene group on the incoming IB. After proton transfer, IBH^+ coordinates with the anion $[AlCl_3OHAlCl_3]^-$ to reduce charge separation, but in contrast to $AlCl_3OH_2$, does not form a bond. This lack of bond formation allows the IBH^+ to react facilely with another IB in the propagation step. There is negligible change to Al-O bond distances after the proton transfer. The E_a value for the initiation reaction with **1** is 21.6 kJ/mol and the overall reaction is exothermic, with ΔE_{rxn} = -47.7 kJ/mol. We have computed the Gibbs free energy of activation, $\Delta G^‡$ at the BP86/def2-TZVP and MP2/def2-TZVP levels of theory, obtaining activation energies of 13.0 and 10.9 kJ/mol, respectively. The low values of E_a and $\Delta G^‡$ indicate that the initiation rate will be significant at the low temperatures of the operating conditions, consistent with the high reaction rate observed for the polymerization reaction.

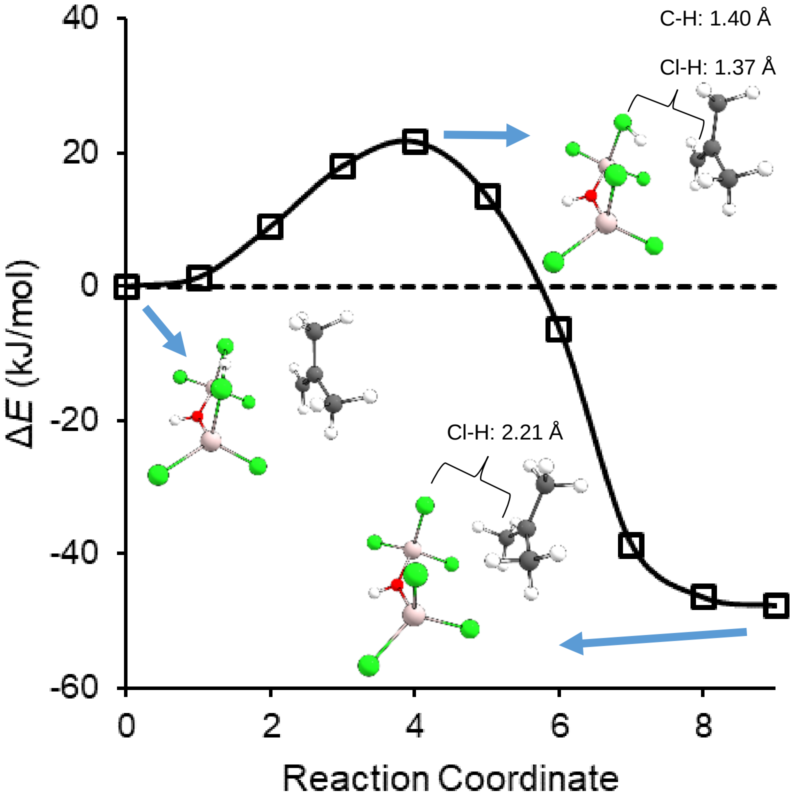

Figure 5. Potential energy surface for the IB initiation reaction with 1.

The key to understanding why **1** is a viable initiation catalyst while other complexes, even those with the same chemical formula, are ineffective (see Figures 32 - 34 in Appendix A) is the acidity of the complex. We have computed pK_a values in both aqueous and gas phases for five complexes (see Appendix Table 2 in Appendix A). The calculations indicate that **1** is a super acid, having an aqueous pK_a of -30.1. This extremely negative value suggests that **1** is not stable in water. However, the complex is stable in the very non-polar environment of the PIB reaction mixture (see the discussion in Appendix A). It is the non-polar character of the system that both stabilizes complexes like **1** and requires that a catalyst have extreme acidity to initiate the reaction.

2.4.2 Propagation Reaction

The propagation step was identified by starting from the product structure of the initiation reaction shown in Figure 5 and adding an IB molecule initially located at various starting positions and orientations, followed by GSM calculations. The lowest energy pathway we have identified is shown in Figure 6. This reaction proceeds via the anti-addition mechanism, where the IB molecule approaches the IBH^+ on the opposite side of the negatively charged initiator complex. We have also identified a syn-addition pathway for this complex, but the barrier is somewhat higher (see Appendix Figure 11 in Appendix A). The E_a value for the propagation reaction is 2.3 kJ/mol, which we believe is associated with the structural reorganization, since the gas phase addition of IB to IBH^+ is barrierless (See Appendix Figure 12). After forming the C-C bond, the new carbocation migrates closer to the anion complex to mitigate the charge separation. The overall reaction is exothermic with ΔE_{rxn} = -12.6 kJ/mol. No experimental data for IB polymerization reaction kinetics have been reported, but it has been noted that the energy barrier for the addition of an ion pair to a monomer in a low polarity medium should be less than 25 kJ/mol.[4] Hence, our calculated propagation reaction barrier is consistent with the general rule from the literature.

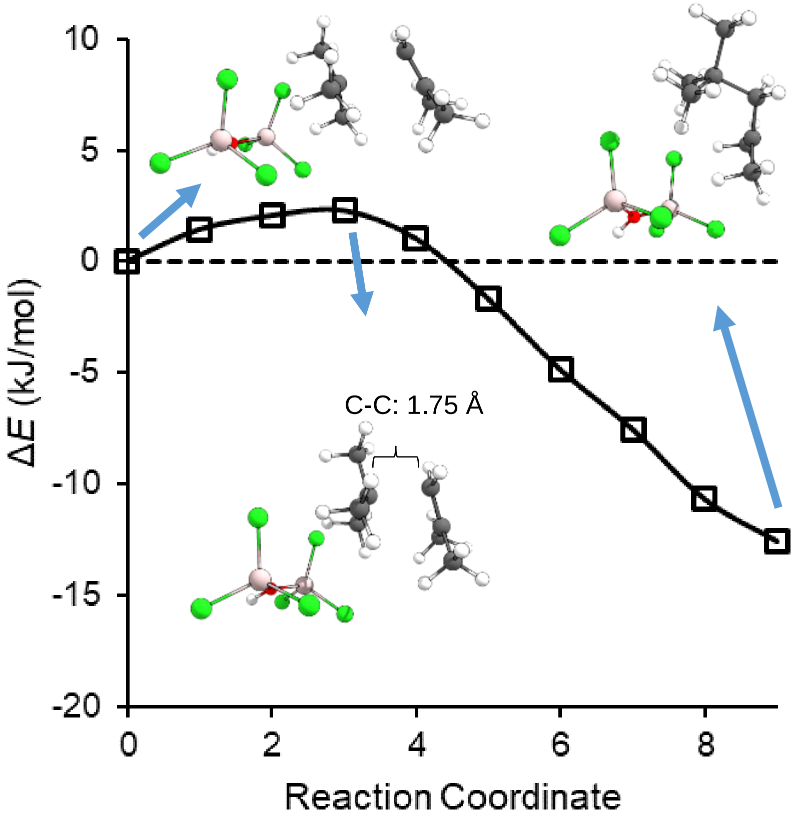

Figure 6. Potential energy surface for the first propagation reaction starting from 1 as the initiator complex.

The second propagation pathway is shown in Figure 7. The E_a value for the second propagation step is 5.0 kJ/mol, which is slightly higher than the first propagation step, but is still well below the 25 kJ/mol threshold.[4] Like the first propagation step, the reaction barrier appears to be associated with the structural reorganization of the cation in relation to the anion. The second propagation reaction is also exothermic (ΔE_{rxn} = -21.9 kJ/mol). Figure 8 summarizes our proposed reaction mechanism with **1**.

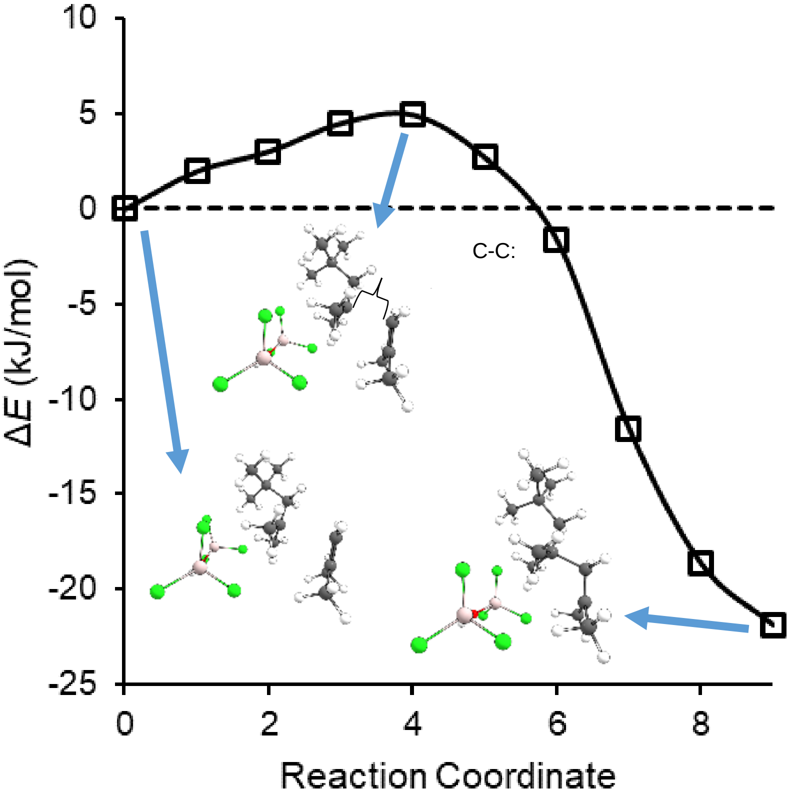

Figure 7. Potential energy surface for the second propagation reaction with 1.

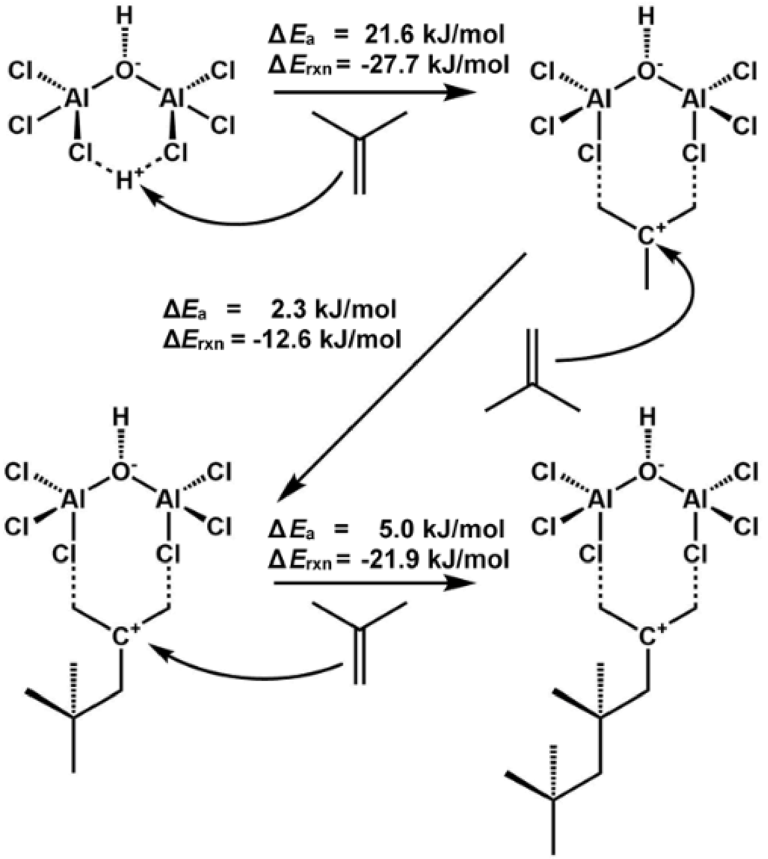

Figure 8. Summary of the propsed initiation and propagation mechanism with 1

2.4.3 AIMD Simulations

We performed AIMD simulations to observe the initiation reaction with various initiator complexes. We could readily observe the reaction starting from **1** in a simulation at 300 K. The proton transfer took place after 5 ps of simulation time. Snapshots from the AIMD simulation are shown in Figure 9, where the actual proton transfer took place in a window of about 125 fs. The reaction in the AIMD simulation proceeds in a similar fashion as the reaction pathway generated with the GSM method, which confirms the reliability of the GSM-generated reaction pathway. The AIMD simulation demonstrated that **1** is an active initiator for the IB polymerization reaction. In contrast, simulations involving other initiator complexes, including $AlCl_3OH_2$, failed to produce a proton transfer event, either at 300 K or 1500 K. This corroborates the high-energy barriers associated with breaking the O-H bond in the $AlCl_3OH_2$ complex.

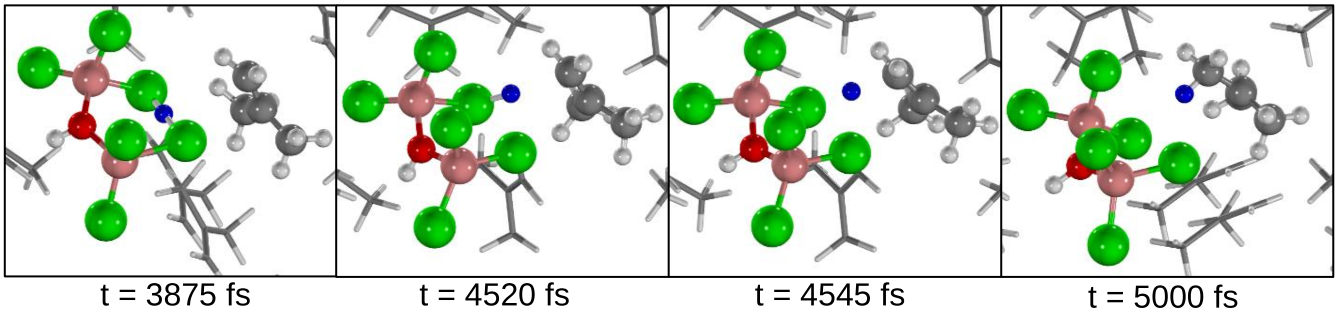

Figure 9. AIMD simulation snapshots showing the progression of the initiation reaction of IB with 1 from Figure 4. The proton of interest is colored blue for clarity and non-reacting IB molecules shown as stick models.

2.5 Conclusion

We have presented the first successful molecular-level study of catalyzed IB polymerization. Our calculations overturn the wide-spread view that the $AlCl_3OH_2$ complex is an effective proton donor and is the active catalyst because both the initiation and propagation steps have excessively high barriers. We used the GSM method to identify an $AlCl_3$-based initiator complex, **1** (Figure 4), having a low-energy barrier pathway for initiation and which is an active catalyst for the propagation reaction. The most important feature of **1** is that it is a super acid. The anion complex of **1**, $[AlCl_3OHAlCl_3]^-$, acts to stabilize the carbocation charge center of the growing polymer chain, while binding the cation only weakly. This relatively weak binding facilitates low reaction barriers for the propagation steps. The low reaction barriers for the initiation and propagation reactions with **1** are consistent with experimental conditions (low temperatures) under which the polymerization reaction is carried out. We conclude that a complex containing at least two $AlCl_3$ groups and one H_2O molecule is necessary to initiate the reaction.

We have investigated the initiation and propagation reaction for polymerization of IB assuming a homogeneous reaction. However, in practice, micron size particles of $AlCl_3$ are suspended in the IB mixture in the production of PIB,[28] which means that the actual reaction mechanism may be heterogeneous. Given that the low energy surface of $AlCl_3$ is chemically inert,[39] we postulate that defective surfaces of $AlCl_3$ particles facilitate the formation of complexes similar to **1**, which can provide low barrier initiation pathways. Investigation of surface-mediated reactions is beyond the scope of this work. We note that our observations about the need for a superacid to initiate the reaction are consistent with recent work on cationic polymerization using heteropolyacids as catalysts.[8]

3.0 Impact of Defects on the Decomposition of Chemical Warfare Agent Simulants in Zr-based Metal Organic Frameworks

3.1 Introduction

New threat patterns of chemical warfare agent (CWA) attacks motivate the search for improved protection against such attacks. Current protection is largely reliant on activated carbon impregnated with metal oxides.[40] Such materials suffer from a variety of drawbacks including poor selectivity[41] and re-emission of the agent.[42] Metal-organic frameworks (MOF) have shown promise in this application because they are capable of achieving high selectivity,[12-13] and they have been shown to react with CWAs,[43] reducing the chance of re-emission.

Recent literature accounts have reported on the interaction of the metal-organic framework (MOF) UiO-67 with the chemical warfare agent (CWA) simulant dimethyl methylphosphonate (DMMP).[14-15] Wang et al.[14] observed chemisorption as well as physisorption of DMMP at missing linker sites on the nodes of UiO-67 through use of infrared spectroscopy (IR) coupled to an ultrahigh vacuum (UHV) chamber; missing linker defects were necessary for chemisorption. However, Ruffley et al.[15] studied adsorption and desorption of DMMP on UiO-67 and functionalized variants under similar conditions but chemisorption was not observed.

The lack of reactivity in the Ruffley et al. study may be due to differences in the MOF synthesis procedures. Wang et al. used the synthesis method of Katz et al.,[44] which features HCl as the acid modulator to form UiO-67 in two hours at 80°C, while Ruffley et al. used an acetic acid modulated synthesis that formed UiO-67 in five hours at 120°C.[45] These two approaches may result in MOF structures that do not have the same defect characteristics. Ruffley et al.

hypothesized that their MOFs had lower levels of defects, which resulted in a lack of reactivity with DMMP. The goal of this work is to understanding why no reactivity was observed by Ruffley et al., while Wang et al. did observe reactions. We are not interested in developing ways to improve the reactivity through defect engineering because the purpose of the MOF is to capture and hold the CWA close to a plasmonic nanoparticle catalytic site.[15] In this work we test that hypothesis by exploring the role of the number and types of defects on the intrinsic reaction barrier for DMMP hydrolysis. We therefore do not consider the initial water displacement step in our calculations, since water adsorption is likely not present under the UHV conditions of the experiments we seek to mimic. We recognize that water displacement might be rate limiting in some cases,[46-48] but since we are interested in the intrinsic hydrolysis mechanism and barrier, we do not consider it. Momeni and Cramer[46] reported pathways where a water molecule is directly involved in the hydrolysis of sarin. However, in this work, our initial state involves DMMP adsorbed onto an open Zr site in the absence of environmental water, as can be seen in Scheme 1. Additionally, we studied the reaction pathway for two inherently undercoordinated Zr-based MOF, PCN-700 and MOF-808, which each have different topologies of open sites.

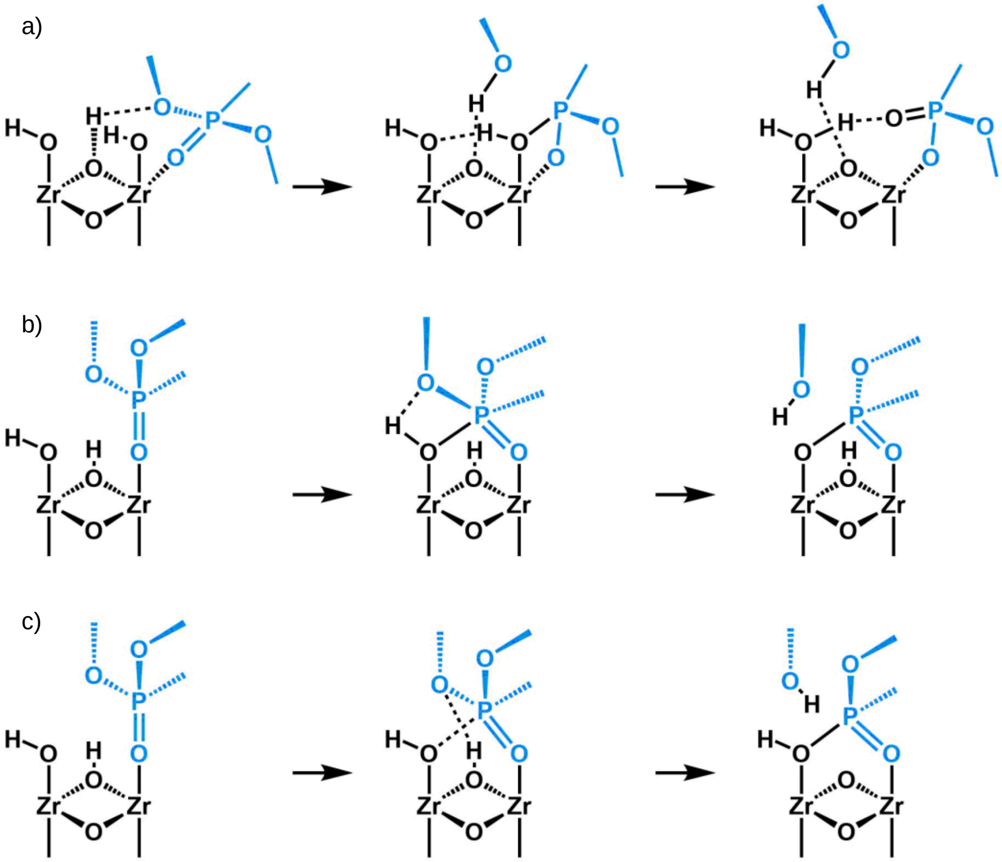

Scheme 1. (a) Hydrolysis of DMMP via 2-defect μ_3-OH elimination (b) adjacent-OH elimination, and (c) μ_3-OH elimination

3.2 Method

We performed both cluster and periodic density functional theory (DFT) calculations in this work. Cluster calculations were performed with the ORCA program.[49] Optimizations were performed at the BP86[23]/def2-SVP[24] level of theory with the RI-J approximation[25] and Grimme's D3 dispersion corrections.[26] Effective core potentials ECP-28[50] were used for Zirconium. Frequency calculations were performed at the same level of theory and basis set to verify that initial and final state geometries were at local minima, that the transition state (TS) had only one imaginary frequency, and to compute zero-point energies and thermal corrections. Single-point energy calculations were performed using the BP86/def2-TZVP[24] level of theory.

The growing string method (GSM), a TS locating technique developed by Zimmerman,[1-3] was used to identify reaction pathways. GSM calculations were performed with ORCA using the BP86 functional with D3 dispersion correction, and with the def2-SVP[24] basis set. We found that the single-ended GSM is a useful tool for identifying potential reaction pathways because it does not require the user to know the configuration of the product of the reaction, only requiring the reactant configuration and a set of bonds to break and form as the input. The product configurations typically identified with single-ended GSM were not at local minima. Consequently, the product configurations were optimized in ORCA with the same functional and basis set and used as inputs in the double-ended GSM method to generate the potential energy surfaces reported here. Single-point energy calculations on GSM reaction coordinates were performed using the BP86/def2-TZVP model chemistry. The BP86 functional was chosen for the sake of computational efficiency; the accuracy of the functional was not considered to be an overriding factor because we are interested in overall reaction barrier trends rather than accurate barriers. Additional single point energy calculations were performed with M06L functional to compare with literature values for similar reactions.

Periodic DFT calculations were performed with the CP2K software package,[51] using the QUICKSTEP method.[32] We used the Perdue-Burke-Ernzerhof (PBE) generalized gradient functional,[33] Goedecker-Teter-Hutter (GTH) pseudopotentials,[34, 52] and short range double-ζ basis sets with polarization.[36] Grimme's D3 dispersion correction[26] was included. The climbing image nudged elastic band method[53-54] was employed to compute reaction barriers, using 10 replicas.

3.3 Hydrolysis of DMMP with Defective UiO-67

3.3.1 1-missing linker defect

The reaction barriers for DMMP hydrolysis via adjacent OH elimination (Scheme 1b) with one missing linker defect UiO-67 computed from different methods are shown in Figure 10. The reaction begins with the adjacent OH group coordinated to the phosphorus atom of DMMP. The TS consists of the pentacoordinated phosphorous intermediate and a hydrogen bond between the adjacently adsorbed hydroxyl group and an ether oxygen on the DMMP (Figure 11a). The ether oxygen then forms a bond to the proton and dissociates as methanol. The BP86/def2-SVP//BP86/def2-TZVP reaction barrier is 84 kJ/mol and the reaction is exothermic by -69 kJ/mol. This reaction barrier, when calculated with a single-point energy at the M06L/6-311++G** level of theory is consistent (100 kJ/mol) with that reported by Wang et al. (97 kJ/mol).[14] This shows that the BP86 level of theory is sufficiently reliable to perform pathway search with GSM, in agreement with our previous work.[55] In addition, it is worth noting that the adjacent-OH elimination pathway identified by Wang et al. is a two-step reaction, whereas our calculations identified a single-step pathway.

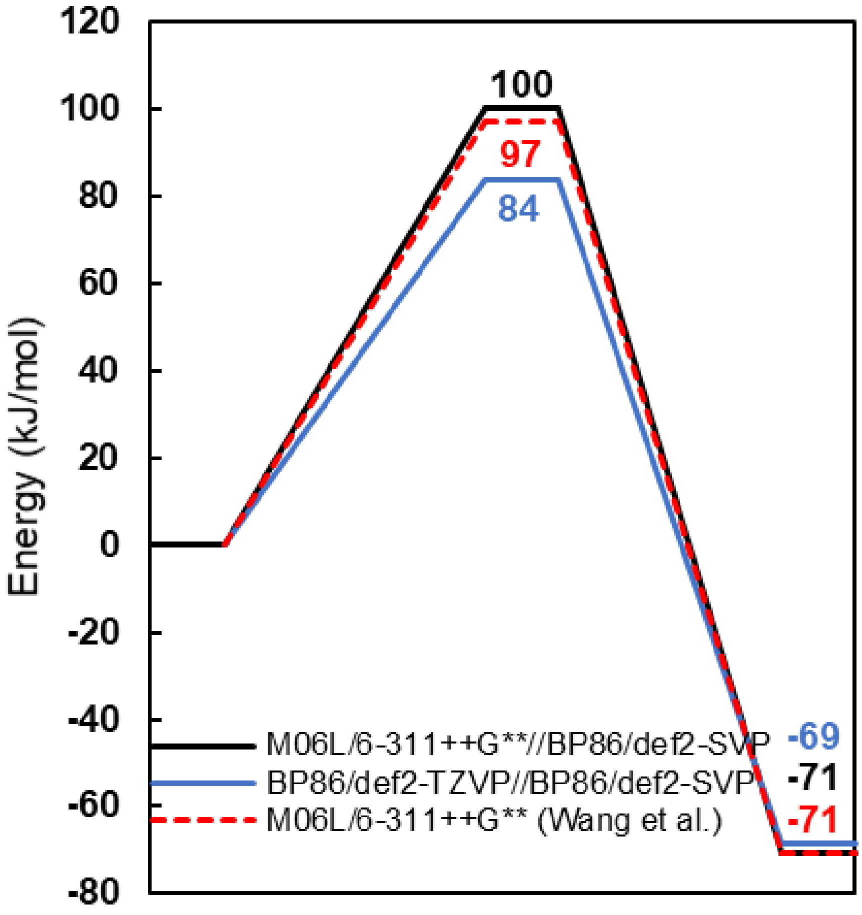

Figure 10. Cluster energy reaction paths for DMMP hydrolysis via adjacent OH elimination with one missing linker defect UiO-67 computed from different levels of theory and energies reported by Wang et al.[14]

With one missing linker defect in UiO-67, DMMP can also be hydrolyzed through the μ_3-OH elimination pathway (scheme 1c). In this pathway, the ether oxygen takes the proton from the μ_3-hydroxyl group instead of from the adjacently adsorbed hydroxyl group. The reaction barrier is 82 kJ/mol and endothermic by 62 kJ/mol as shown in Figure 12. The endothermic nature of this pathway is consistent with that reported by Morris and colleagues.[14] The TS of this pathway also forms the pentacoordinated phosphorous intermediate like the adjacent OH elimination pathway (Figure 11c). Consequently, both pathways have very similar reaction barrier and TS as can been seen from seen in Figure 11 and 12. Variation in their reaction energies is the result of different products being formed. The bound product of the adjacent-OH elimination pathway is an aprotic methyl methylphosphonic acid (MMPA), which binds more strongly to the SBU as compared to the neutral MMPA produced via the μ_3-OH elimination pathway.

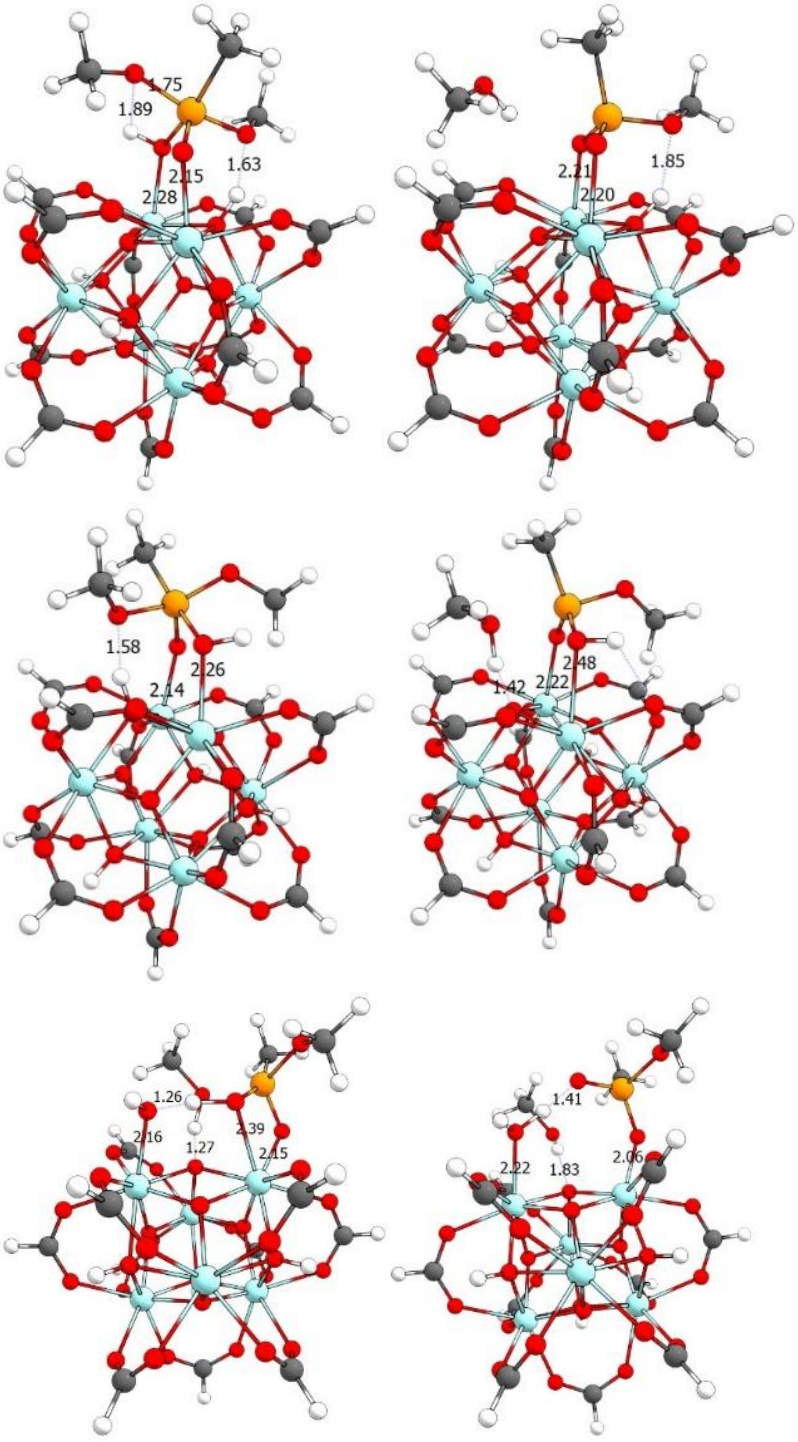

Figure 11. Transition state (TS) and product state (PS) of defective UiO-67 pathways. (a) TS and (b) PS of 1-defect adjacent OH elimination. (c) TS and (d) PS of 1-defect μ$_3$-OH elimination. (e) TS and (f) PS of 2-defect μ$_3$-OH elimination.

3.3.2 2-missing linker defect

An additional missing linker introduces new possible pathways. On the same SBU, there are four distinct configurations for the second linker to be removed,[56] and the lowest reaction pathway that we found is through the 2-defect μ_3-OH elimination as shown in scheme 1a. This pathway requires the two missing linkers to be adjacent to each other, which yields a Zr with two uncoordinated sites. Consequently, an OH group and an DMMP can adsorb onto the same Zr atom. The TS involves the DMMP forming a pentacoodinated phosphorous with the OH group adsorbed on the same Zr atom and the OH group forming a hydrogen bond with the vicinal OH group adsorbed on the adjacent Zr (Figure 11e). As the ether oxygen removes a proton from the μ_3-OH and dissociates as methanol, the vicinal OH group removes a proton from an OH group bonded to phosphorus to form adsorbed water (Figure 11f). The reaction barrier is 52 kJ/mol, which is 44 kJ/mol lower than the single defect μ_3-OH elimination barrier and 32 kJ/mol lower than the adjacent-OH elimination barrier. The residual product for this pathway is aprotic MMPA, which is similar to that produced via the one defect adjacent-OH elimination. It is surprising that the reaction energies of 1-defect adjacent OH elimination and 2-defect μ_3-OH elimination are almost identical. The products for these two reactions are significantly different; the 1-defect product has two P-O-Zr bonds and the 2-defect has the P=O hydrogen bonded to the chemisorbed water. One would expect the hydrogen bond to be weaker than the Zr-OP bond. It appears that the 2-defect product state is equally favorable due in part to the formation of strongly chemisorbed water (as can be seen from Figure 11, the Zr-OH_2 bond distance of 2.22 Å versus Zr-OP bond).

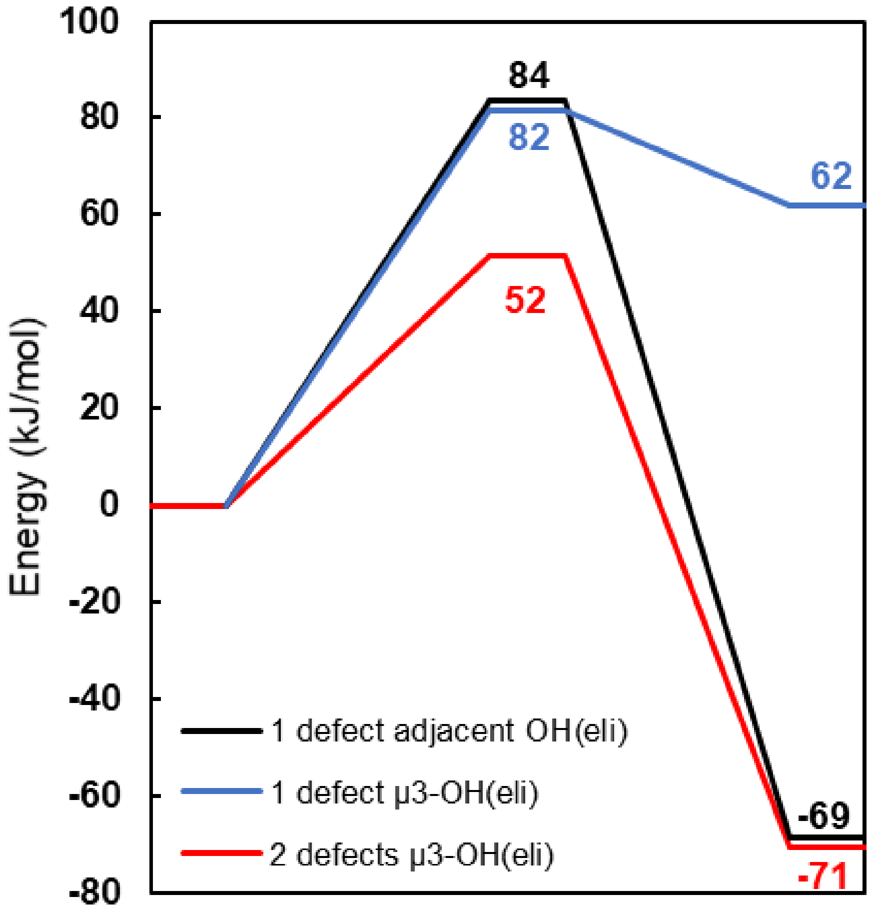

Figure 12. Lowest cluster energy pathways for DMMP hydrolysis on defective UiO-67 computed at BP86/def2-TZVP//BP86/def2-TZVP.

One reason that the TS of 2-defect μ_3-OH elimination is lower than the 1-defect OH elimination state because it is a late TS, i.e., is more product-like, and the product is lower energy than the reactant. In addition, the 2-defect TS (Figure 11e) has two shorter and stronger hydrogen bonds: OH-OH of 1.26 Å and MeOH-OH of 1.27 Å, which lower the TS energy relative to the 1-defect TS (Figure 11a), which has only one weaker hydrogen bond: MeOH-OH of 1.85 Å.

Our calculations to this point have used a cluster model with formate cap meant to mimic the linkers. This is a highly abstracted model of the periodic MOFs, which may not give accurate energies.[57-58] We therefore computed DMMP reaction pathways for 2-defect μ_3-OH elimination and 1-defect adjacent OH elimination using full periodic models with the NEB method within CP2K. The periodic pathways and energies (shown in Figures 37 and 38 in Appendix B) are consistent with those of the cluster system. This indicates that the cluster model with the formate cap is adequate for studying the hydrolysis of DMMP with UiO-67.

3.4 Hydrolysis of DMMP with Inherently Undercoordinated Zr-based MOF

Next, we report the reaction barrier for hydrolysis of DMMP with inherently undercoordinated Zr-based MOFs, PCN-700 and MOF-808. Our aim is to compare the reaction pathways for hydrolysis on pristine PCN-700 and MOF-808 with that of the 2-defect UiO-67. PCN-700 is a Zr-based MOF with an octa-coordinated $Zr_6O_4(OH)_8(H_2O)_4$ SBU. A DMMP hydrolysis pathway similar to the 2-adjacent missing linker UiO-67 pathway is not feasible on PCN-700 because of steric hindrance, as shown in Appendix Figure 15 in Appendix B. The lowest-energy barrier pathway that we found for pristine PCN-700 is similar to the 1-defect UiO-67 μ_3-OH elimination, which yielded a methanol and a neutral MMPA as products. Consequently, the reaction barrier of 88 kJ/mol and reaction energy of 56 kJ/mol (see Figure 13) for this pathway are comparable to those of the 1-defect UiO-67 μ_3-OH elimination pathway. The lowest barrier pathway for PCN-700 is shown in Figure 14a and b. This is also reinforced by the very close resemblance between the TS and FS of the 1-defect UiO-67 μ_3-OH elimination (Figure 2c & d) and PCN-700 (Figure 14a & b) pathways.

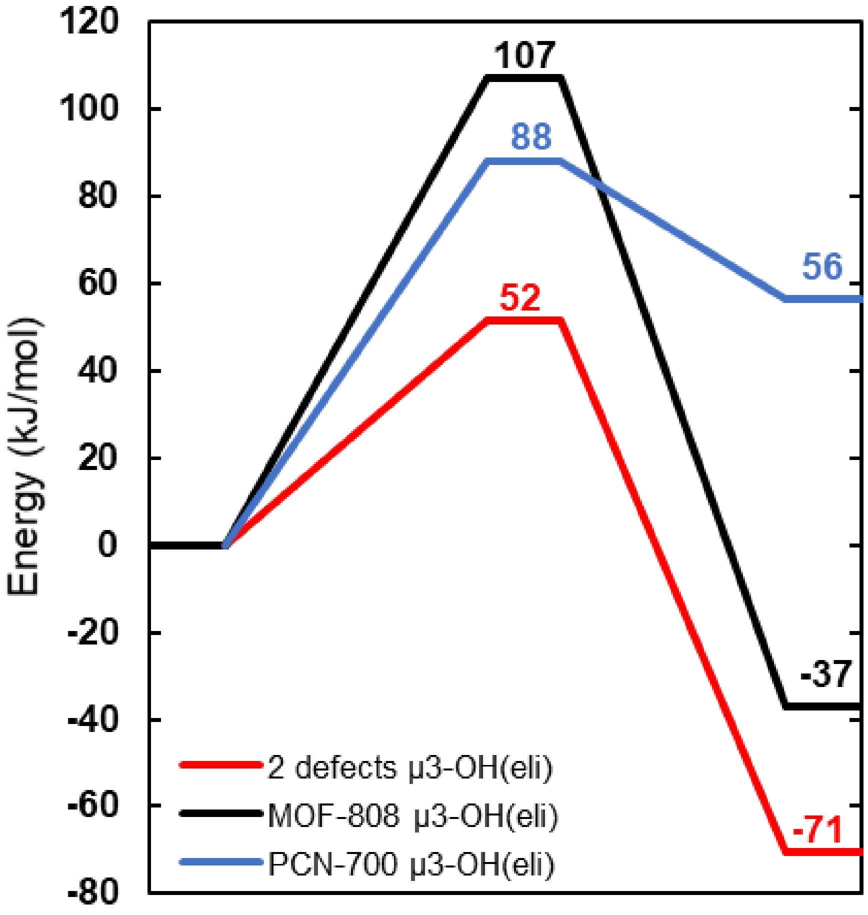

Figure 13. Lowest energy pathways of DMMP hydrolysis on cluster models of pristine PCN-700 and MOF-808 computed at BP86/def2-TZVP. The pathway for the 2-defect UiO-67 is also shown for comparison.

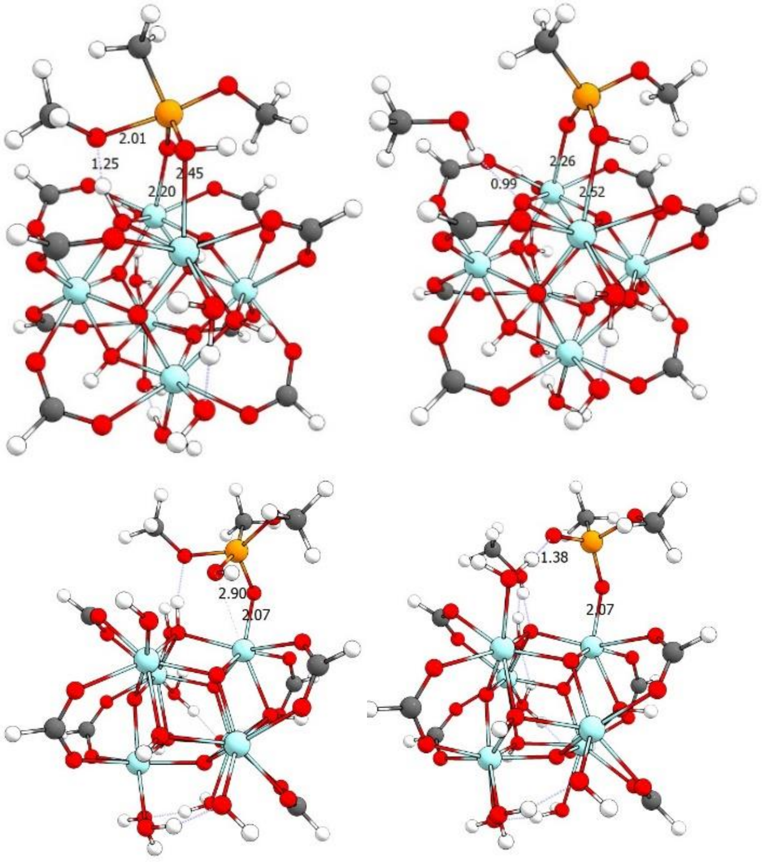

Figure 14. Transition state (TS) and product state (PS) of pristine PCN-700 and MOF-808 shown in Figure 13. (a) TS and (b) PS of PCN-700 μ_3-OH elimination. (c) TS and (d) PS of MOF-808 μ_3-OH elimination.

MOF-808 has an even lower coordination than PCN-700, with a six-connected $Zr_6O_4(OH)_{10}(H_2O)_6$ SBU. The lowest energy pathway that we found is similar to the 2-defect μ_3-OH UiO-67 elimination pathway. The reaction barrier of 107 kJ/mol is more than twice that of the 2-defect UiO-67 case (see Figure 13). At the TS, the OH group that is bound to the DMMP dissociates from the Zr site, as seen in Figure 14c. Furthermore, this OH group does not form a hydrogen bond with the vicinal OH group, like the TS of the 2-defect UiO-67. These two factors resulted in a high reaction barrier. Even though MOF-808 produces the same products and its product state (Figure 14d) is almost identical to the product state of the 2-defect UiO-67 (Figure 2f), the reaction energy of MOF-808 is -37 kJ/mol, which is 34 kJ/mol less exothermic than that of the 2-defect UiO-67. This indicates that topology of the SBU affects the reaction barrier and reaction energy.

3.5 Conclusion

We have examined the hydrolysis reaction pathway of DMMP on UiO-67 with one and two missing linkers, pristine PCN-700, and pristine MOF-808. We used both fully periodic models and cluster models to study reaction pathways on UiO-67 with multiple defects per SBU. The lowest energy pathway for the 1-defect UiO-67 is via the adjacent OH elimination pathway. In contrast, the lowest energy pathway for the 2-defect UiO-67, PCN-700 and MOF-808 is via the μ_3-OH elimination pathway. The 2-defect UiO-67 has the lowest reaction barrier among all the MOFs we studied. 2-adjacent missing linkers defects yields a Zr atom with two uncoordinated sites and allows DMMP and an OH group to adsorb onto to the same Zr atom. The close proximity between DMMP and the OH group enables the low-energy hydrolysis pathway.

PCN-700 and MOF-808 contain inherently undercoordinated Zr sites, but they yield higher reaction barriers than the 2-defect UiO-67. Due to the topology of PCN-700, a hydrolysis pathway similar to that of 2-adjacent missing linkers UiO-67 is not feasible. Instead, the lowest-energy pathway is similar to the 1-defect UiO-67 μ_3-OH elimination. The lowest-energy pathway for MOF-808 is similar to the 2-defect UiO-67 μ_3-OH elimination pathway, but the reaction barrier is substantially higher. This suggests that MOF topology of the open metal sites and the number of sites are important parameters in controlling the reaction barrier.

4.0 Method for Predicting Dipole Moments of Complex Molecules for Use in Thermophysical Property Estimation

This work was published as: Vo, M. N.; Call, M.; Kowall, C.; Johnson, J. K. (2019). Method for Predicting Dipole Moments of Complex Molecules for Use in Thermophysical Property Estimation. Ind. Eng. Chem. Res. 58, 19263-19270

4.1 Introduction

Molecular dipole moments are essential for developing potential models and predicting thermophysical properties of fluids. Thermophysical properties such as vapor viscosity and thermal conductivity are required for industrial process design calculations,[59-61] but they are often not available for many species, especially for proprietary compounds. Furthermore, vapor phase dipole moments are difficult to measure experimentally and data for complex molecules are scarce.[62-64]

Alternatively, it has been shown that quantum chemical methods such as density functional theory (DFT) can be used to accurately estimate the dipole moment vector for simple molecules.[18-19, 65-66] However, dipole moments for molecules with many conformational degrees of freedom have been very challenging to calculate. This is because the conformation of the molecule can greatly affect its dipole moment.[67] For example, the vapor phase dipole moment of the octanoic acid changes by more than two Debye, from 1.55 D to 4.27 D, as a result of the orientation of the hydrogen atom in the carboxylic acid group, as shown in Figure 15. Hence, it is critical to account for the conformation dependence of the dipole moment to accurately estimate the experimental dipole moment for molecules with multiple conformations having widely differing dipole moments. Molecular conformations can be explored through a variety of methods (e.g., ab initio molecular dynamics (AIMD), systematic configuration generation, classical molecular dynamics using model potentials).

The motivation of this work is to assess the accuracy of different computational methods to calculate the gas or vapor phase dipole moment for molecules for use in thermophysical property estimation and provide recommendations for efficient and reliable dipole estimation methods. We evaluate the use of CONFAB,[68] an open source algorithm that systematically generates diverse low-energy conformers for molecules, for conformation generation. We evaluate the use of Boltzmann weighting to correctly account for the relative population of different conformations in the gas phase at specific temperatures. Additionally, we compare the performance of this method to obtaining conformations from AIMD simulations. We also examine the impact of using calculated dipole moments to estimate vapor viscosity and thermal conductivity.

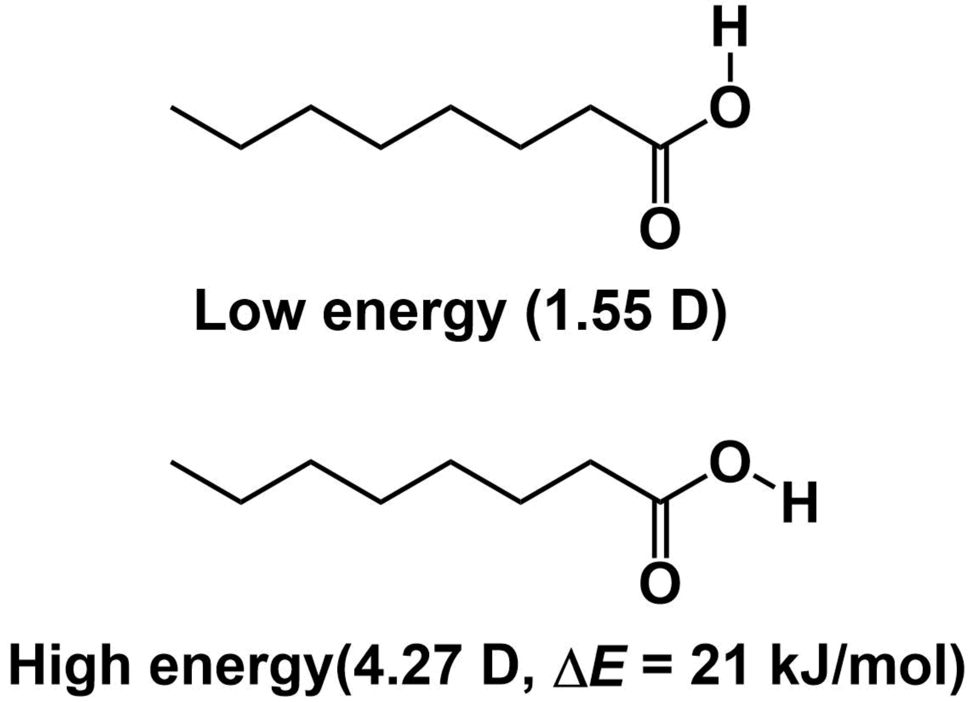

Figure 15. Two conformations of octanoic acid having very different dipole moments.

4.2 Method

4.2.1 Electronic Structure Calculations

All dipole moment calculations were performed with the ORCA version 3.03 program.[22] Optimizations were performed at the B3LYP[69]/def2-SVP[24] level of theory with the RI-J approximation[25] and Grimme's D3 dispersion correction.[26] Single-point energy and dipole moment calculations were performed using the B3LYP/def2-TZVP[24] level of theory. Performing optimizations with a small basis set speeds up the optimization process with minimal effect on the accuracy. Solution polarizability effects were ignored for molecules that are liquid at normal conditions (20°C and 1 atm) because we are solely interested in the vapor phase dipole moments.

4.2.2 Conformer Generations

A modified version of the CONFAB algorithm in OpenBabel[70] version 2.4 was employed for conformer generations (see Appendix C). For most molecules, the energy and root mean square deviation (RMSD) cutoff were set to 25 kJ/mol and 0.5 Å, respectively. CONFAB optimized each structure with the MMFF94 forcefield[71] before computing the energy for ranking and cutoff. All generated conformers were re-optimized with DFT in the ORCA, as described above, to ensure that they are at local minima within DFT. Dipole moments were averaged using Boltzmann weighting:

$$\langle D \rangle = \frac{\sum_{i=1}^{N} D_i e^{(E_o - E_i)/RT}}{\sum_{i=1}^{N} e^{(E_o - E_i)/RT}} \tag{4-1}$$

where $\langle D \rangle$ is the weighted dipole moment, N is the number of conformers generated, D_i and E_i are the dipole moment and total DFT energy (i.e., zero Kelvin energy without zero-point energy corrections) of conformer i, respectively. E_o is the energy of the lowest energy conformer, R is the gas constant, and T is the absolute temperature. The temperature used in eq (1) corresponded to the temperature at which the experimental dipole moment was reported.

4.2.3 AIMD Simulations

Born-Oppenheimer AIMD simulation were performed with the CP2K software package,[31] using the QUICKSTEP method[32] and a timestep of 0.5 fs. We used the Perdue-Burke-Ernzerhof (PBE) generalized gradient functional.[33] Goedecker-Teter-Hutter (GTH) pseudopotentials and short-range double-ζ basis sets with polarization were employed.[34-35] Gas phase simulations were performed with a single molecule in the isothermal-isochoric (*NVT*) ensemble for 10 ps. Configurations were sampled in the last 5 ps.

4.2.4 Gas-phase Viscosity and Thermal Conductivity Estimation

The vapor viscosity of molecules was calculated using methods of Chapman et al.,[72] Chung et al.,[17, 73-74] Lucas,[75] and Reichenberg.[76-77] Thermal conductivities were calculated using the Chung et al. method.[17, 74, 78] Properties and parameters for these calculations were taken from the Aspen Plus™ PURE36 database, except for the dipole moments. Predictions of vapor viscosities and thermal conductivities using experimental dipole moments, calculated dipole moments, and dipole moments set to zero were compared.

4.3 Basis Set and Level of Theory

First, we examined molecules in the NIST computational chemistry comparison and benchmark database [64, 79] to determine a reliable level of theory and basis set for computing dipole moments. The NIST database has a large set of calculated dipole moments (~1800) but only about 400 molecules in the database have experimental dipole moments. We identified the B3LYP/TZVP level of theory as giving reasonably accurate dipole moments at an acceptable computational cost. We found this level of theory gives dipole moments in good agreement with both higher level of theory and experimental data.[19] We selected nine molecules from the NIST database with available experimental dipole moments as our test set, shown in Figure 16, and performed DFT calculations on these molecules using the conformations reported in the NIST database.

From Table 1, our calculations are within 20% of the MP2/cc-pVTZ method and fall within 10% of the experimental data for all molecules except for di-n-propyl ether and sulfurous acid dimethyl ester, which gave absolute errors of 24% and 32%, respectively. Both molecules have many conformational degrees of freedom, but only one geometry was examined and reported, hence part of the error with respect to experiments for these two molecules is due to ignoring important conformational effects. It is worth noting that even the higher level of theory, MP2/cc-pVTZ, underestimated the dipole moments by more than 20% for these two molecules. As will be discussed below, calculated dipole moments for these two molecules improved when we account for conformational effects.

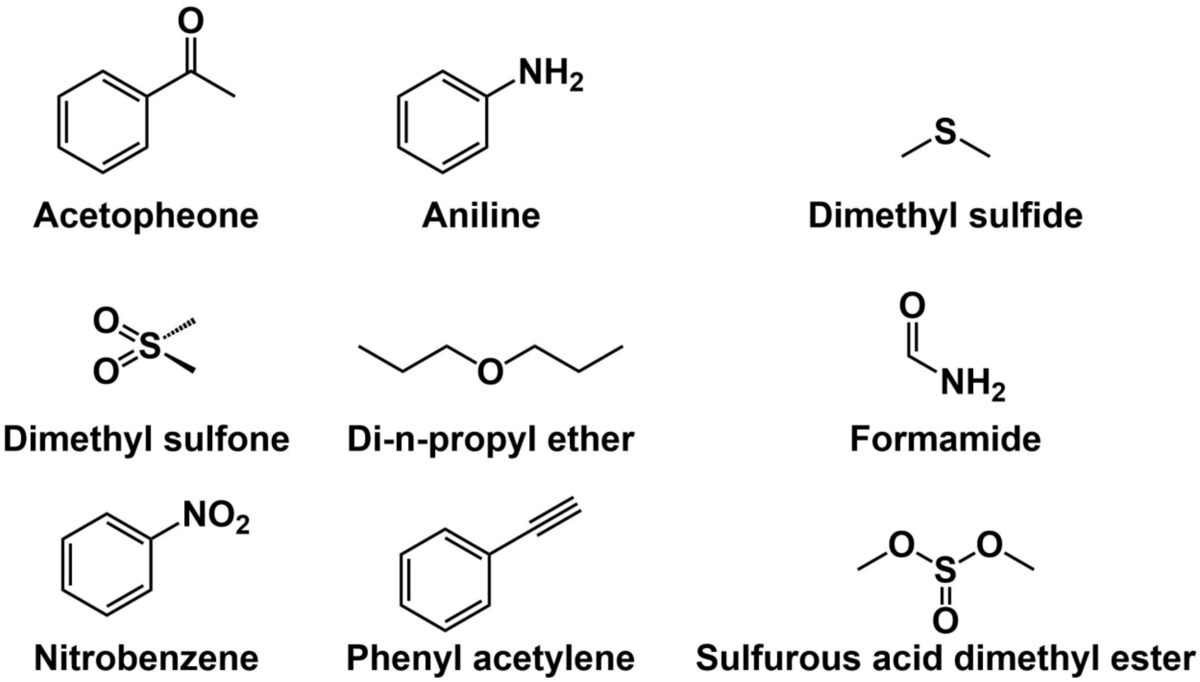

Acetopheone

Aniline

Dimethyl sulfide

Dimethyl sulfone

Di-n-propyl ether

Formamide

Nitrobenzene

Phenyl acetylene

Sulfurous acid dimethyl ester

Figure 16. Benchmark molecules with available experimental dipole moments examined in this work.

Table 1. Comparison of calculated vapor phase dipole moment (units in Debye) with data from the NIST database

	NIST Database			This work
Molecules	EXP	B3LYP/TZVP	MP2/cc-pVTZ	B3LYP/def2-TZVP
Acetophenone	3.02	3.19	3.00*	3.12
Aniline	1.53	1.65	1.51	1.72
Dimethyl sulfide	1.50	1.64	1.56	1.53
Dimethyl sulfone	4.49	4.88	4.43	4.59
Di-n-propyl ether	1.21	1.07	1.02	0.92
Formamide	3.73	4.02	3.81	3.96
Nitrobenzene	4.22	4.81	4.10	4.64
Phenylacetylene	0.66	0.74	0.63	0.74
Sulfurous acid dimethyl ester	3.09	2.32	1.74	2.09

* Performed at MP2/aug-cc-pVTZ

4.4 Conformational Effects

We have identified 18 molecules that have significant conformational degrees of freedom and for which the dipole moment has been experimentally measured to evaluate the impact of conformations on the computed dipole moment. These molecules are shown in Figure 17 and include two molecules from Figure 16, namely di-n-propyl ether and sulfurous acid dimethyl ester. We used the CONFAB program to generate low-energy and structurally diverse conformers for these 18 molecules. The dipole moments of the generated conformers were Boltzmann weighted and this Boltzmann weighted average (BWA) value was compared with the dipole moment of the lowest energy structure (LES) for molecules in Figure 17, as reported in Figure 18 and Table 2.

Note that the LES computed dipole moment for sulfurous acid dimethyl ester in Table 2 is not the same as the value reported in Table 1 because the conformations are different; specifically, the conformation reported in the NIST database is not the lowest energy structure. We divided the list of molecules into two groups: vapor phase and condensed phase. The group names refer to the phase corresponding to the experimental dipole moment measurements.

Overall, the BWA and LES methods give similar dipole moment estimations and both methods give similar accuracy compared with experimental values. The mean absolute errors (MAE) for the LES method are 0.21 and 0.37 D, for vapor and condensed phase molecules, respectively. The BWA method yields a slightly higher MAE of 0.23 D for vapor phase molecules and the same MEA of 0.37 D for condensed phase molecules. Higher MAE values are expected for condensed phase molecules because we are generating conformations in the vapor phase rather than condensed phase, and it is known that solvent effects can impact dipole moments.[63]

It is surprising that the predicted dipole moments for the molecules in Figure 17 are no better when using the BWA method as compared with the LES method. In principle, the BWA method should give the correct ensemble average, under the assumptions that (1) the conformations generated are drawn randomly from the set of all possible conformations, (2) a sufficient number of conformations has been generated, and (3) the dipole moments computed from DFT are sufficiently accurate.

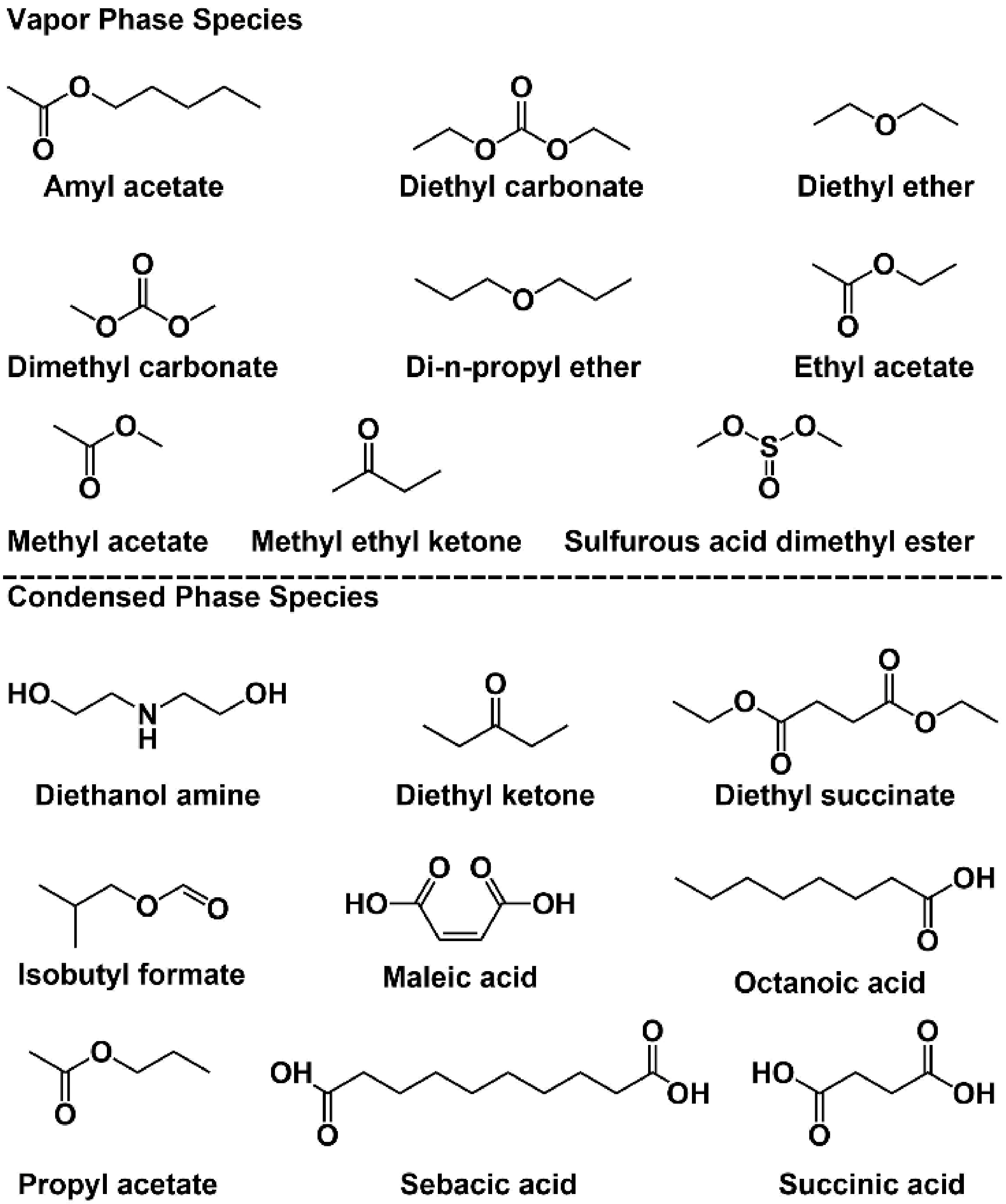

Figure 17. Molecules studied in this work. Condensed phase species refer to molecules with only experimental condensed phase dipole moment reported in the literature.

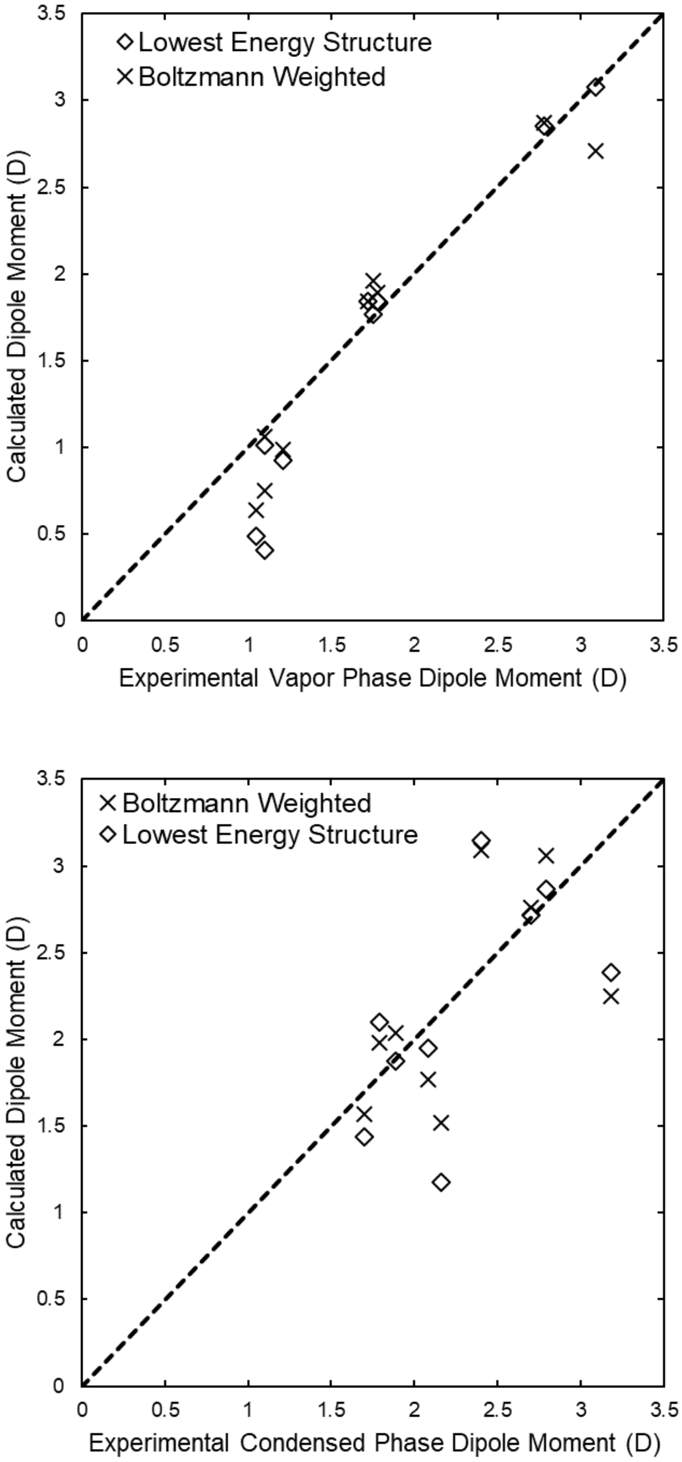

Figure 18. Comparison of Boltzmann averaged dipole moments and dipole moments of the CONFAB generated lowest-energy structure to experimentally measured dipole moments for a) vapor phase and b) condensed phase molecules.

Dimethyl carbonate and diethyl carbonate have the largest absolute errors compare to experimental results. These two molecules have two major conformers: cis-cis and cis-trans, as shown in Figure 19.[80-83] The problem with these molecules appears to be that the high dipole moment configuration (cis-trans) is much higher in energy, and hence contributes little to the Boltzmann average, giving a BWA that is too small. This is probably because CONFAB does not correctly account for the degeneracy of conformers, which would change the BWA. This is because CONFAB is a systematic conformer generator and uses the RMSD to differentiate between distinct conformers, excluding conformers that structurally similar, even though they could be distinct. This is the case for dimethyl and diethyl carbonates, because the cis-trans conformation is doubly degenerate. Thus, CONFAB has no way of accounting for the actual number of degenerate or nearly degenerate conformers in a finite-temperature system. In the next section we test this hypothesis by generating conformations for a select set of molecules from AIMD simulations.

4.5 AIMD Simulation

The correct weighting of configurations can, in principle, be generated from AIMD simulations, under the assumptions that (1) the simulation time is sufficiently long to be ergodic and (2) the functional used in the DFT calculations is sufficiently accurate. We performed *NVT* ensemble simulations for di-n-propyl ether, dimethyl carbonate, diethyl carbonate, and sulfurous acid dimethyl ester in the gas phase, to generate physically realistic distributions of conformations; the results from these simulations are shown in Table 3. These molecules were chosen because their BWA dipole moments are substantially different from the vapor phase experimental values.

Table 2. Boltzmann averaged dipole moments and dipole moments of the lowest-energy structure and their errors (units in Debye)

Molecule	Experiment	Boltzmann Weighted	Absolute Error	Lowest-energy structure	Absolute Error
Vapor Phase Molecules					
Amyl acetate	1.75±0.10*	1.96	0.21	1.77	0.02
Diethyl carbonate	1.10±0.06‡	0.75	0.35	0.41	0.69
Diethyl ether	1.10*	1.06	0.04	1.01	0.09
Dimethyl carbonate	1.05‡	0.64	0.41	0.49	0.56
Di-n-propyl ether	1.21±0.06‡	0.99	0.22	0.92	0.29
Ethyl acetate	1.78±0.09*	1.89	0.11	1.84	0.06
Methyl acetate	1.72±0.09‡	1.84	0.12	1.84	0.12
Methyl ethyl ketone	2.78±0.02*	2.87	0.09	2.85	0.07
Sulfurous acid dimethyl ester	3.09‡	2.71	0.38	3.08	0.01
Condensed Phase Molecules					
Diethanol amine	2.79§	3.06	0.27	2.86	0.07
Diethyl ketone	2.82*	2.76	0.06	2.72	0.02
Diethyl succinate	2.16§	1.52	0.64	1.18	0.98
Isobutyl formate	1.88*	2.04	0.15	1.88	0.01
Maleic acid	3.18±0.02§	2.25	0.93	2.39	0.79
Octanoic acid	1.70§	1.57	0.13	1.44	0.26
Propyl acetate	1.78*	1.98	0.19	2.10	0.31
Sebacic acid	2.40±0.02§	3.09	0.69	3.14	0.74
Succinic acid	2.08±0.02§	1.77	0.31	1.95	0.13

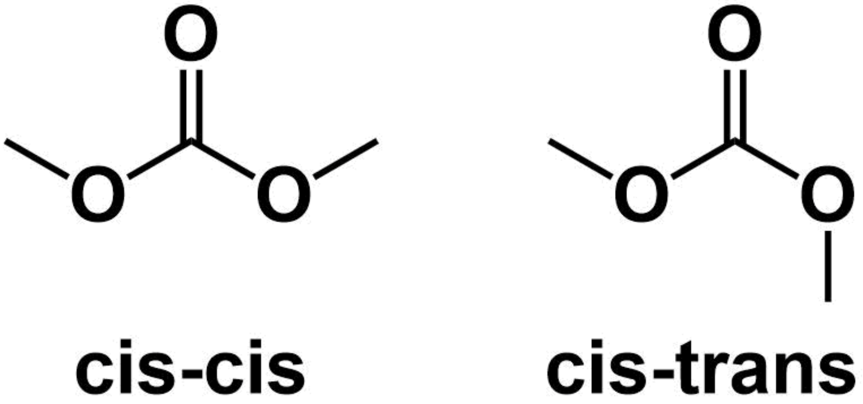

Figure 19. Two major conformations of dimethyl carbonate.

Two dipole moment values are shown in Table 3 for diethyl carbonate and dimethyl carbonate; these correspond to independent simulations started in either cis-cis or cis-trans conformations. The AIMD simulations for these two molecules are non-ergodic over the short time-scale of the simulation because there is a large barrier for rotation (40 kJ/mol for dimethyl carbonate, see Appendix Figure 16 in Appendix C). Hence, simulations started in the cis-cis conformation were not observed to convert to the cis-trans conformation, and vice versa. The average dipole moments from AIMD simulations for the cis-cis configuration are 0.74 and 0.96 D for dimethyl carbonate and diethyl carbonate, respectively. The average dipole moments for cis-trans are 3.66 and 3.78 D for dimethyl carbonate and diethyl carbonate, respectively. Okada performed MD simulations of liquid dimethyl carbonate using a classical model potential and reported that it took about 50 ns to reach conformational equilibrium at 80°C.[81] This supports our observations that the AIMD simulations are non-ergodic, since our simulations were run for only 0.02 ns. However, for dimethyl and diethyl carbonates it appears that the experimental dipole moment may be influenced by dimerization in the vapor phase. Reddy and Balasubramanian reported that dimerization of dimethyl carbonate is energetically favorable in the vapor phase, based on first principles calculations.[82] Moreover, they showed that polarization effects in the liquid phase of dimethyl carbonate give rise to much larger dipole moments than for isolated molecules. Therefore, it is likely that the dipole moments of dimerized dimethyl carbonate will be larger than for isolated molecules. It is reasonable to assume that this is also true for diethyl carbonate. Since our AIMD simulations were only performed using a single molecule, dimerization effects could not be accounted for. Consequently, we propose that long-time classical molecular dynamic simulations containing many molecules of dimethyl carbonate or diethyl carbonate will be necessary to access the configurations required for accurate calculation of the dipole moments of these molecules.

Table 3. Summary of dipole moments computed from con-formers generated from AIMD simulations, compared with experiments and computed values from the BWA and LES methods (units in Debye)

Molecule	Experiment	AIMD	BWA	LES
Diethyl carbonate	1.10±0.06	0.96/ 3.78*	0.52	0.41
Dimethyl carbonate	1.05	0.74/ 3.66*	0.54	0.49
Di-n-propyl ether	1.21±0.06	1.16	0.95	0.92
Sulfurous acid dimethyl ester	3.09	3.13	2.71	3.08

* The values correspond to simulations started in the cis-cis or cis-trans conformations, respectively.

The AIMD method yields good agreement with the dipole moments of di-n-propyl ether and sulfurous acid dimethyl ester. Note that both BWA and LES methods underestimate the dipole moment of di-n-propyl ether. To understand the reason for this, we compared the RMSD of molecules sampled from AIMD simulations with the lowest energy structure generated from CONFAB. The lowest energy structure generated by CONFAB was used as the starting configuration for the AIMD simulation run. Figure 20a shows the RMSD of sample AIMD structures relative to the lowest energy structure generated by CONFAB for di-n-propyl ether. The majority of sampled AIMD structures are very different from the lowest energy structure, with a most probable RMSD of 0.8 Å, and no structures within an RMSD of 0.6 Å. In contrast, when we compared our AIMD configurations to an arbitrary higher energy structure generated from CONFAB (1.05 D, ΔE = 4.5 kJ/mol), approximately half of the AIMD structures have RMSD values within 0.5 Å (Figure 20b). This indicates that the lowest energy structure is not representative of the structures typically sampled for di-n-propyl ether in the vapor phase. As the result, the BWA and LES methods underestimate the dipole moment of di-n-propyl ether. It seems counter-intuitive that the lowest energy structure is not sampled in an AIMD simulation; this can be explained by noting that the higher energy structures are much more entropically favored, hence, the free energy of the lowest energy structure must be higher than the free energies of structures sampled with high frequency in the AIMD simulation. Note that the entropy arises from conformational degrees of freedom, not vibrational degrees of freedom.

We can conclude from these results that the CONFAB approach fails to generate structures that can be used in a Boltzmann weighting approach to arrive at the correct ensemble average dipole moment. The failure of CONFAB is probably due to (1) exclusion of degenerate structures through the exclusion of conformations with RMSD values within 0.5 Å and (2) optimization of the structures with a classical forcefield, which would cause some conformations to be missed because they relax to a local minimum that might have a dipole moment different from the non-optimized structure.

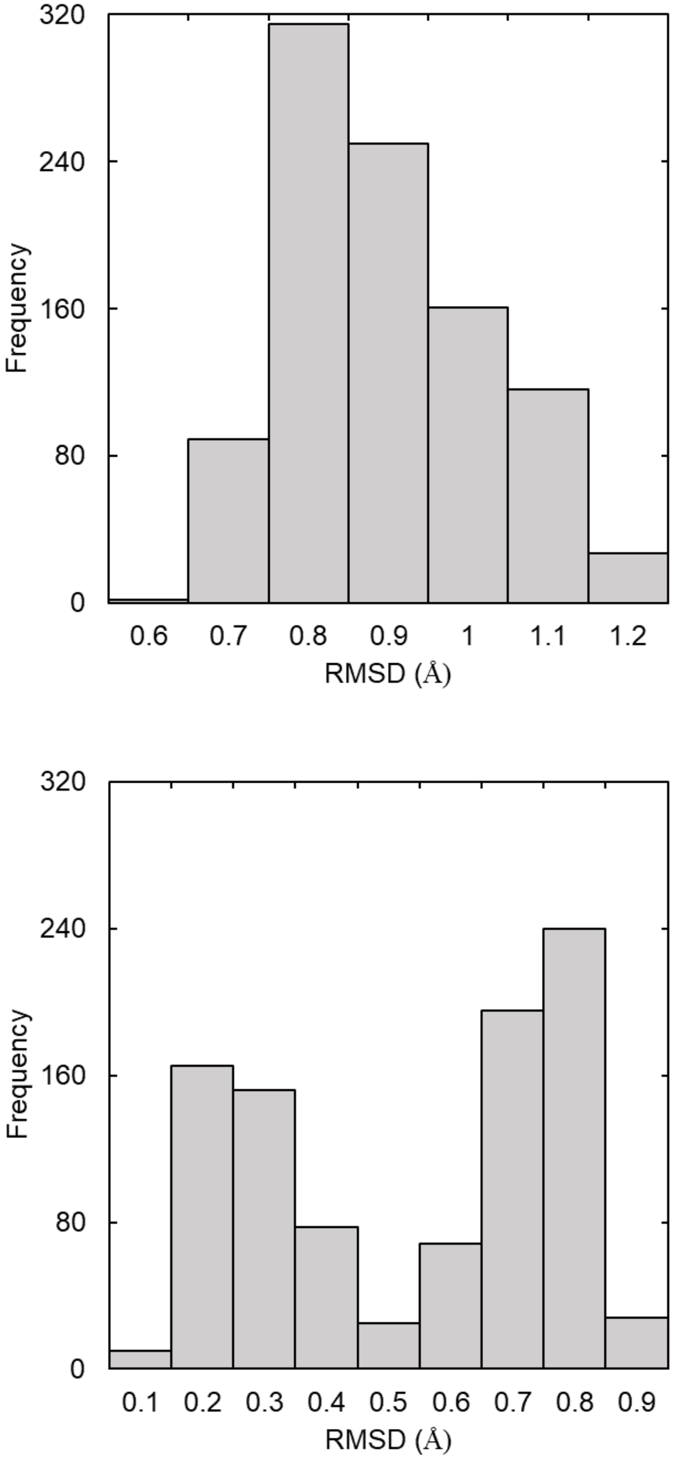

Figure 20. (a) RMSD of structures of di-n-propyl ether with respect to lowest energy structure generated by CONFAB (b) with respect to an arbitrary structure generated by CONFAB (1.05 D, ΔE = 4.5 kJ/mol)

4.6 Thermophysical Properties Estimation

4.6.1 Vapor Viscosity

To assess the importance of dipole moment on estimating thermophysical properties, we examined four different vapor viscosity prediction models: Chapman et al.,[72] Chung et al.,[17, 73-74] Lucas,[75] and Reichenberg.[76-77] We also evaluated one model for estimating thermal conductivity developed by the Chung et al.[17, 74, 78] The vapor viscosities were computed from 0 to 300°C with 10°C increments. We compared values computed using the BWA dipole moments and $\mu = 0$ to values obtained using experimental dipole moments for estimating vapor viscosity with the Lucas method (Figure 21). The Lucas method results are shown here because this method is the most sensitive to the dipole moment, among the four methods tested. Results for other methods follow similar trends and can be found in Tables 8 - 12 in Appendix C. It can be seen from Figure 21 that vapor viscosity is insensitive to the dipole moment when $\mu < 1.3$ D. This indicates that for molecules with low dipole moments, one can neglect the dipole moment contribution when estimating the vapor viscosity. Vapor viscosity is sensitive to higher dipole moments (> 1.3 D). Errors as high as 12% were observed when using $\mu = 0$. We also observe that viscosities computed using calculated dipole moments are in good agreement with values obtained using experimental dipole moments, as seen by MAE values of zero when using calculated dipole moments.

To understand the reason for the high degree of consistency observed between using experiment and calculated dipole moments for estimating vapor viscosities we need to examine the polarity correction factor (F_p°) used in the Lucas method, which is a piecewise function of the reduced dipole moment (μ_r) given by

$$F_p^* = \begin{cases} 1 & 0 \leq \mu_r \leq 0.022 \\ 1 + 30.55(0.292 - Z_c)^{1.72} & 0.022 \leq \mu_r \leq 0.075 \\ 1 + 30.55(0.292 - Z_c)^{1.72}|0.96 + 0.1(T_r - 0.7)| & 0.075 \leq \mu_r \end{cases} \tag{4-2}$$

where Z_c is the critical compressibility factor and T_r is the reduced temperature. μ_r is defined as:

$$\mu_r = 52.46 \frac{\mu^2 P_c}{T_c} \tag{4-3}$$

Where μ is the dipole moment, P_c is the critical pressure in bar, and T_c is the critical temperature in K.

It can be seen from Figure 21b that the reduced dipole moments computed from experimental and estimated values of μ have very similar values of μ_r for the molecules tested. Moreover, the values of μ_r for each molecule lie within the same boundary limits of eq (2). Consequently, the polarity corrections are identical for the experimental and estimated values of μ, and thus yield the same vapor viscosity values for the molecules tested. On the other hand, when μ = 0 D, μ_r = 0, F_p° = 1, and no polarity correction is made to the estimated vapor viscosity values. Hence, for systems where $\mu_r > 0.022$ for the experimental dipole moment, large errors could result from assuming $\mu = 0$, as seen in Figure 21a.

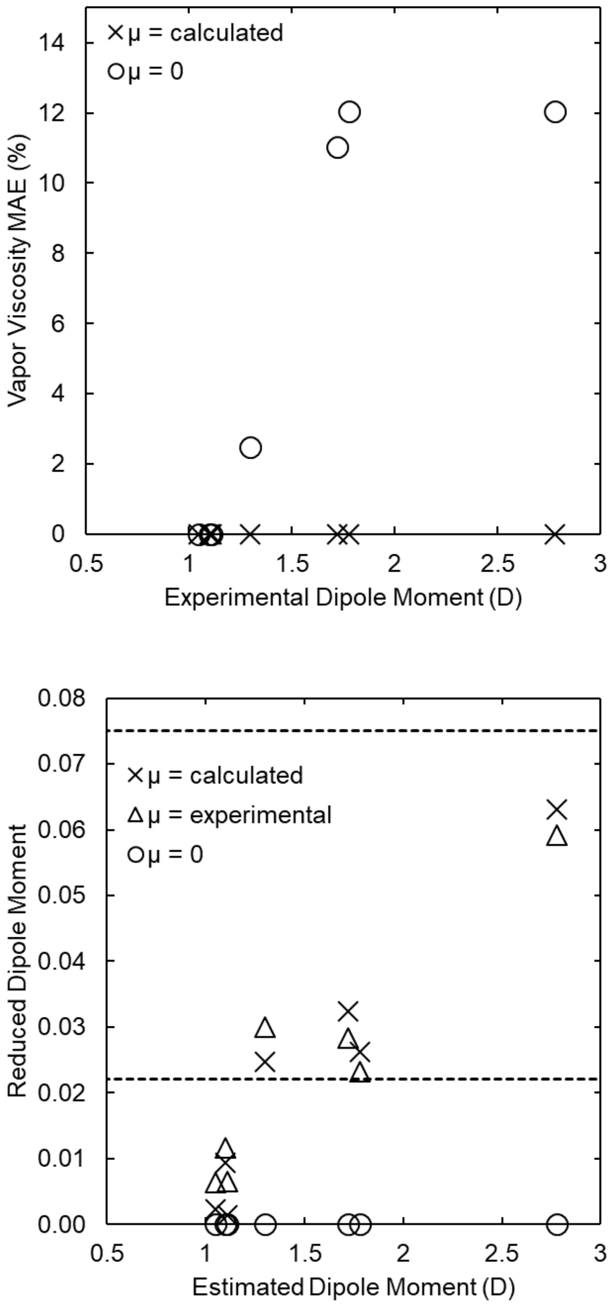

Figure 21. (a) Mean absolute error in the viscosities calculated from the Lucas method using BWA calculated dipole moments and μ = 0. The viscosities computed using the experimental dipole moments were used as reference. (b) Comparison of reduced dipole moments as defined by Lucas method. Dashed lines mark the boundary limits in the piece-wise function for F_p° in eq (2) of μ_r = 0.022 and 0.075. Molecules evaluated (ordered in increasing dipole moment) are: dimethyl carbonate, diethyl carbonate, diethyl ether, dimethyl ether, methyl acetate, ethyl acetate, and methyl ethyl ketone.

Among the other vapor viscosity methods studied, the Reichenberg method yields negligible differences between using experimental, estimated, or zero dipole moments. The largest error observed for the Chung et al. for using $\mu = 0$ is 5.2% for methyl ethyl ketone.

Figure 22 compares vapor viscosities estimated from the Lucas method with μ computed from the BWA method to experimentally measured vapor viscosity values. Calculated vapor viscosities of dimethyl ether and diethyl ether are in good agreement with experimental values. Values for methyl acetate and ethyl acetate deviate from experimental values by up to 10%. This, however, is consistent with the error reported when using experimental dipole moment.[84]

The estimated thermal conductivity follows the same trend as the estimated vapor viscosity, but it is much less sensitive to dipole moment than the vapor viscosity, as shown in Table 4. Although octanoic acid and maleic acid experimental dipole moments are measured in the condensed phase, we report their error here because we are interested in the performance of calculated dipole moment to estimate thermal conductivity. It can be seen from Table 4 that the dipole moment has a negligible effect on the thermal conductivity of dimethyl carbonate, diethyl carbonate, and octanoic acid. Only for maleic acid is the error in the thermal conductivity significant when using $\mu = 0$. We see that using the BWA estimated dipole moment yields no error. Although the BWA dipole moment of maleic acid (2.2 D) is 0.93 D lower than the experimental condensed phase dipole moment, they yield the same estimated thermal conductivity. This shows that, overall, using calculated dipole moments rather than assuming $\mu = 0$ yields more reliable thermophysical property values, even if the error in the dipole moment is fairly large.

We note that while the viscosity and thermal conductivity calculations were performed with the BWA dipole moments, the same results would be obtained using the LES method.

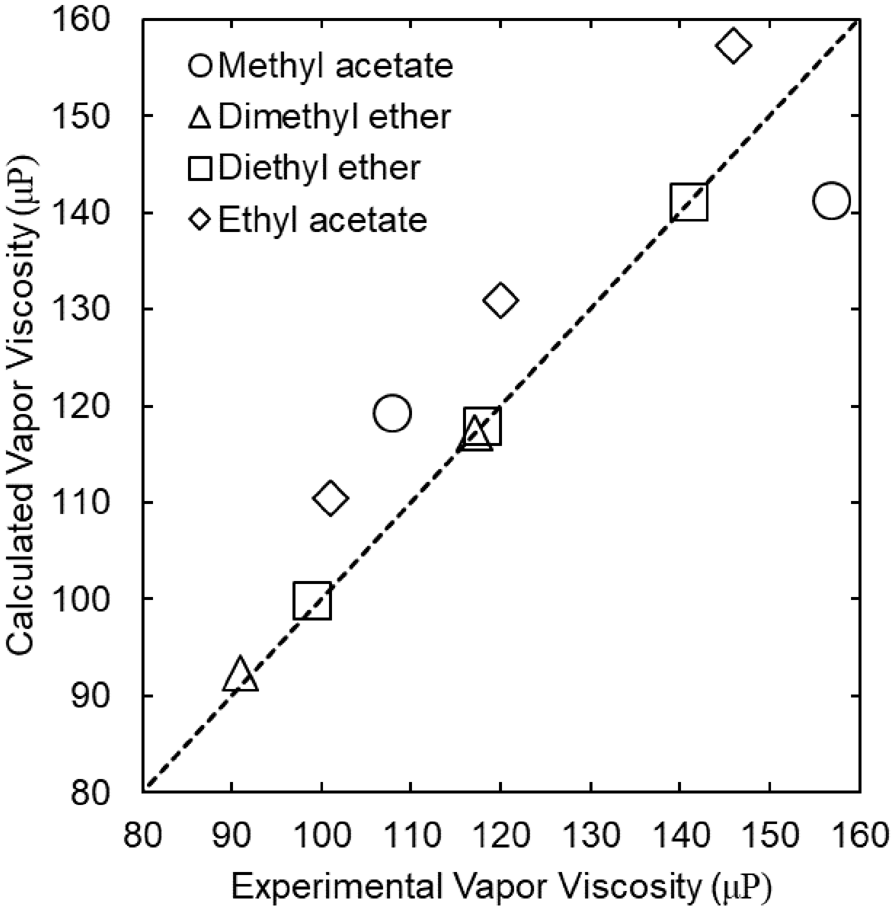

Figure 22. Comparison of experimental and calculated vapor viscosities (in micropoise, µP) for selected molecules. Vapor viscosities are reported at specific temperature based on literature values: Methyl acetate (125, 200°C), dimethyl ether (20, 100°C), diethyl ether (125, 200, 300°C), and ethyl acetate (125, 200, 300°C)

Table 4. Summary of mean average error of thermal conduc-tivity estimation when using μ = BWA and μ = 0

Molecule	Exp Dipole Moment (D)	Thermal Conductivity MAE (%)	
		μ = BWA	μ = 0
Dimethyl carbonate	1.05	0	0
Diethyl carbonate	1.10	0	0
Octanoic acid	1.70	0	0.1
Maleic acid	3.18	0	9.4

4.7 Conclusion

In this work, we have shown that the B3LYP/def-TZVP level of theory yields acceptably accurate dipole moments for small molecules compared with experiments and higher-level theories. More importantly, we compared three different approaches for estimating dipole moments for molecules with many degrees of conformational freedom. The most efficient method is the LES method, which only involves finding the lowest energy structure for a molecule. However, the LES method may give poor results if the lowest energy structure is not representative of the most common structures at the temperature (and density for condensed phases) of interest, as we showed to be the case for di-n-propyl ether. Multiple configurations can be accounted for by using a Boltzmann weighting of dipole moments for configurations generated by CONFAB and optimized to their local minimum geometries with DFT methods (BWA method). However, CONFAB does not correctly account for degeneracy and near-degeneracy of structures and hence the BWA method does not always give good results. Generating configurations from AIMD simulations at the temperature of interest will, in principle, give accurate results. However, this method is the most computationally expensive of the three and will fail in practice if the configurational equilibration time is much longer than the time that can be reasonably simulated, which is typically on the order of tens of picoseconds. Another method for generating configurations for dipole calculations is to use a classical empirical potential to carry out long-time molecular dynamics (or Monte Carlo) simulations, but this approach requires that one has a potential model of acceptable accuracy, which is not always the case, especially for new (e.g., proprietary) molecules.

Among the four common vapor viscosity estimation methods, the Lucas method is the most sensitive to the dipole moment. Only dipole moments above about 1.3 D affect the viscosity estimation using the Lucas method, and even higher values of dipole moments are necessary to impact viscosity estimation using the Chung method. Estimated thermal conductivity is even less sensitive to dipole moment, showing differences only when $\mu > \sim 3$ D. Estimating these thermophysical properties with calculated dipole moments yields results in extremely good agreement with estimations using experimental dipole moments. These findings can be useful for fast and efficient vapor viscosity and vapor thermal conductivity estimation of novel molecules. The recommended method is to first identify the lowest energy structure using CONFAB, then relax the configuration and compute its dipole moment using DFT. If the dipole moment is above the threshold value of about 1.3 D, one can use the calculated dipole moment to estimate the vapor viscosity and thermal conductivity (threshold of about 3 D). Otherwise, one can neglect the dipole moment effect.

5.0 Future Work

5.1 Investigate the effect alkyl chain length on dipole moment of aliphatic oligomers

The work for predicting dipole moment of complex molecules for use in thermophysical property estimation was discussed in Chapter 4. As the molecule gets longer, the conformational degree of freedom and the computational cost increases dramatically, making it impossible to exhaustive sample all conformational degrees of freedom for long chain molecules such as polymers. Nevertheless, it is important to investigate the effect of increasing chain length on the dipole moment of aliphatic oligomers because the dipole moment is needed for thermophysical property estimations and experimental measurement of their dipole moments is infeasible. We postulate that the dipole moment of a chain will converge to a limiting value as the chain length increases. For this work, we examine the effect of chain length on the dipole moment of polyisobutylene succinic anhydride (PIBSA). A diagram of PIBSA is shown in Figure 23.

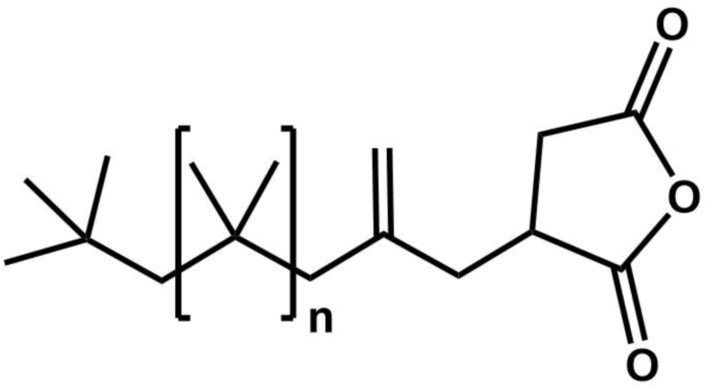

Figure 23. Structure of PIBSA

For this work, we employed the conformer sampling program CREST,[85] for conformer generation. The dipole moment was computed at the B3LYP/def2-TZVP level of theory. The Boltzmann weighted averaging method, as described in Chapter 4, was used to assess the effect of chain length on the dipole moment of PIBSA. The preliminary result for n = 0 to 9 are shown in Figure 24.

It can be seen from Figure 24 that the dipole moment gradually decreases by about 1 D as the chain length increases from n = 0 to n = 9. Figure 25 shows the distribution of dipole moment for selected chain length. The distribution of dipole moment ranges from about 3.5 D to 5.5 D. At the shorter chain lengths, n = 0 and 2, the peaks are around 5 D. At the longer chain length, the peaks are closer to 4.1 D. The distribution of dipole moment changes with chain length, and it is not obvious why this is happening. Further analysis of the results is required and summarized below:

1. Compare structures with high /low dipole moment to assess the trend
2. Assess parameters that can be used to correlate the trend. For example, radius of gyration

3. Assess whether the decrease in dipole moment affects the vapor viscosity estimation value

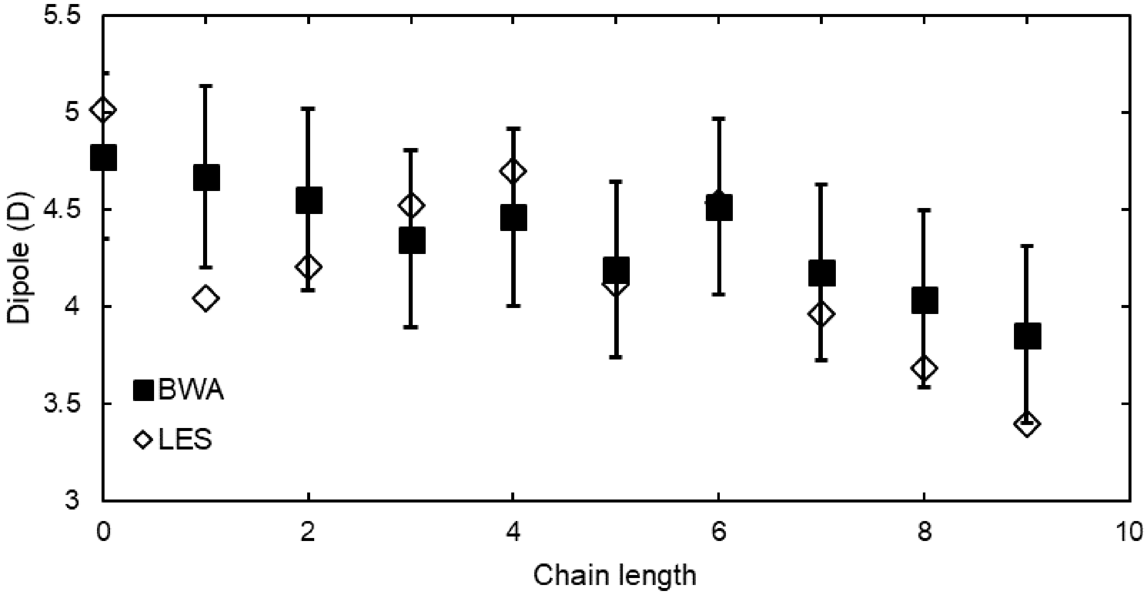

Figure 24. Dipole monent of PIBSA for n = 0 to n = 9

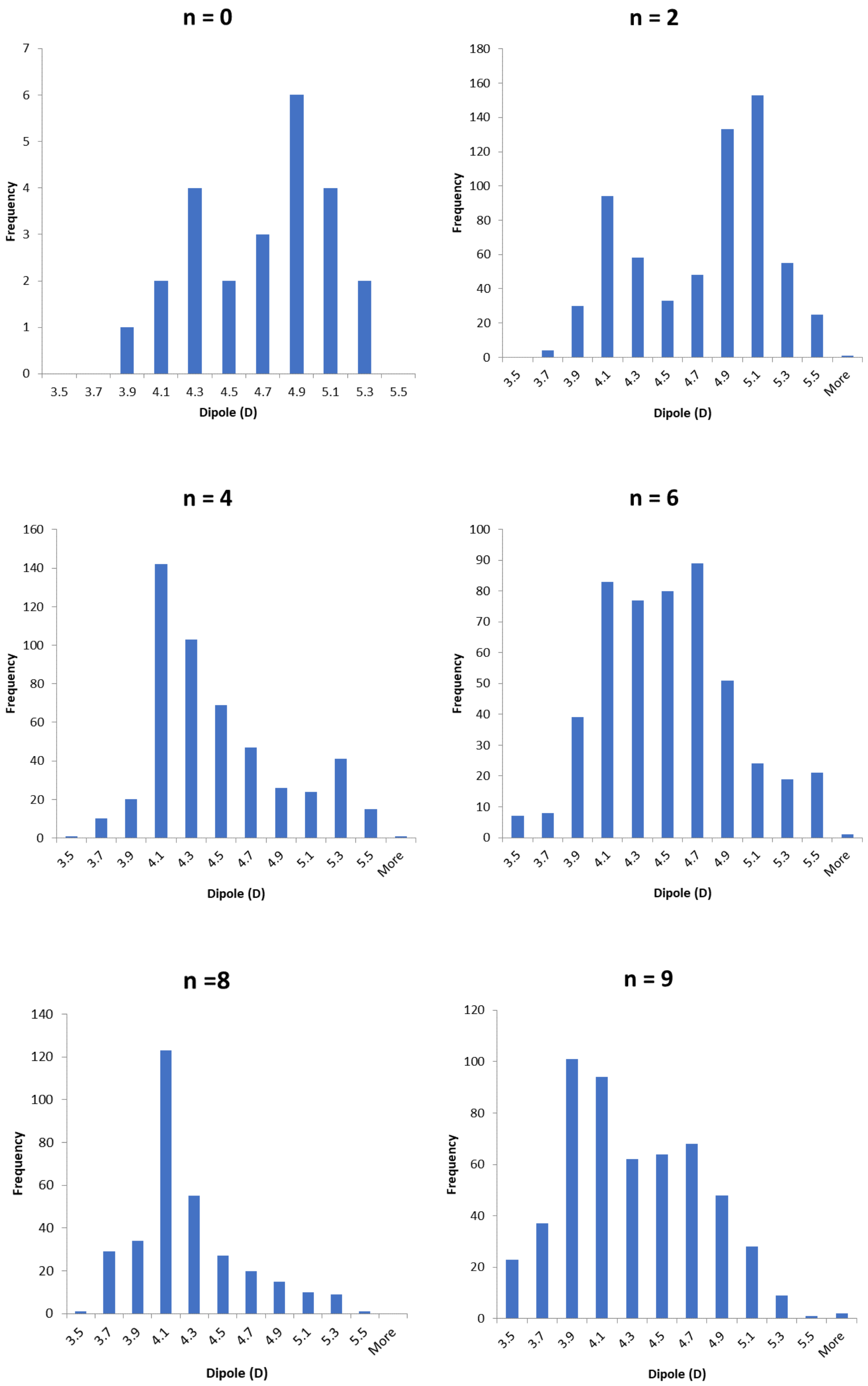

Figure 25. Dipole distribution for PIBSA with different chain length. n = 0, 2, 4, 6, 8, and 9

6.0 Summary of Publications from Ph.D.

6.1 Published Work

1. Vo, M. N.; Basdogan, Y.; Derksen, B. S.; Proust, N.; Cox, G. A.; Kowall, C.; Keith, J. A.; Johnson, J. K. (2018). Mechanism of Isobutylene Polymerization: Quantum Chemical Insight into AlCl3/H2O-Catalyzed Reactions. ACS Catal. 8, 8006-8013
2. Vo, M. N.; Call, M.; Kowall, C.; Johnson, J. K. (2019). Method for Predicting Dipole Moments of Complex Molecules for Use in Thermophysical Property Estimation. Ind. Eng. Chem. Res. 58, 19263-19270

6.2 Manuscript in preparation

1. Vo, M. N.; Ruffley, P. J.; Johnson, J. K. Impact of Defects on the Decomposition of Chemical Warfare Agent Simulants in Zr-based Metal Organic Frameworks
2. Vo, M. N.; Call, M.; Kowall, C.; Johnson, J. K. The effect of chain length on the dipole moment of polyisobutylene succinic anhydride

Appendix A Mechanism of Isobutylene Polymerization

Appendix A.1 Theory and Basis Set Comparison

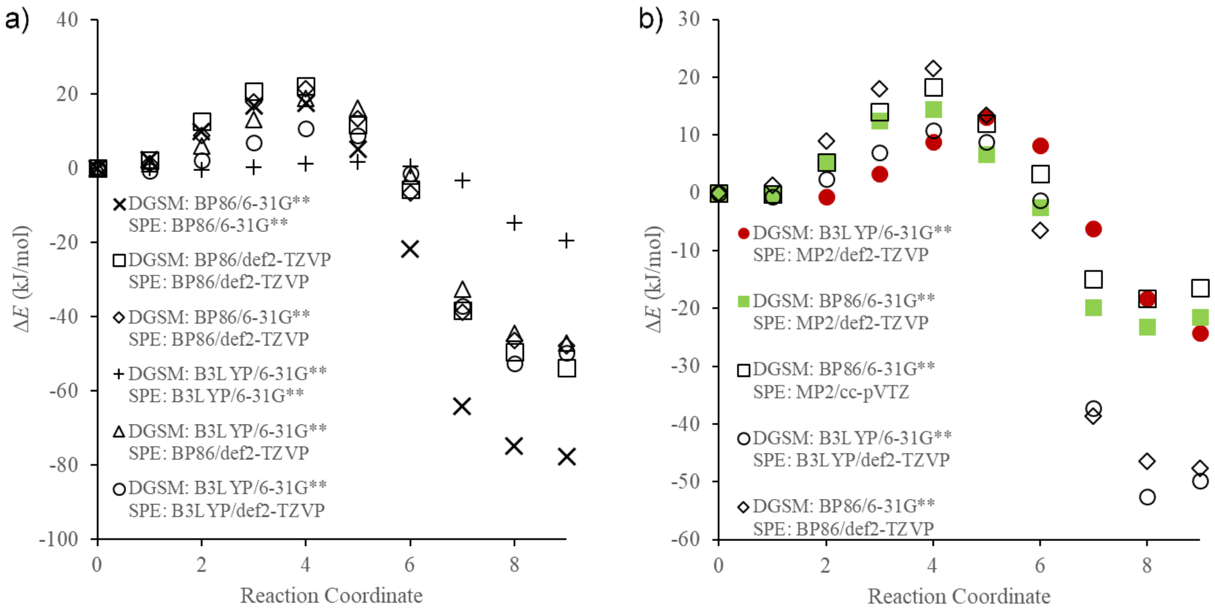

Appendix Figure 1. Potential energy surfaces (PES) for the initiation reaction with complex 1 at different level of theory and basis sets for double-ended GSM, and post-GSM single-point energy calculations.

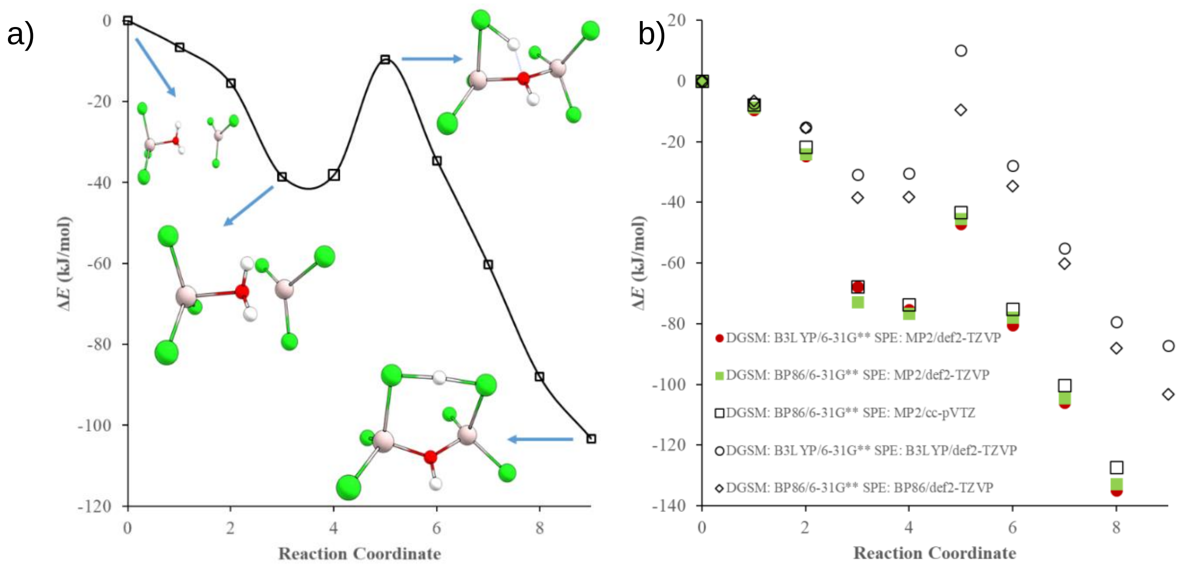

Appendix Figure 2. a) PES for the formation of complex 1 at BP86/6-31G and b) at different levels of theory**

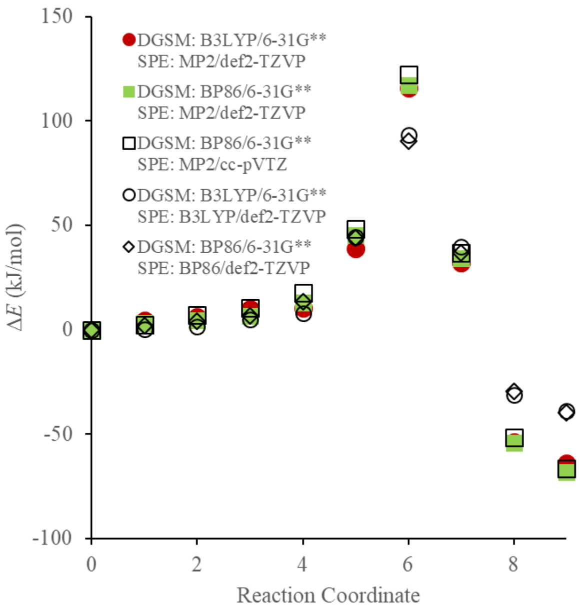

Appendix Figure 3. PES for the initiation reaction with $AlCl_3OH_2$ at different levels of theory

Appendix Table 1. Summary of ΔE_a and ΔE_{rxn} (kJ/mol) at different levels of theory

	Initiation with $AlCl_3OH_2$		Initiation with complex 1		Formation of complex 1	
	ΔE_a	ΔE_{rxn}	ΔE_a	ΔE_{rxn}	ΔE_a	ΔE_{rxn}
DGSM: BP86/6-31G** SPE: BP86/def2-TZVP	90.3	-39.8	21.6	-47.7	40.9	-56.4
DGSM: B3LYP/6-31G** SPE: B3LYP/def2-TZVP	93.2	-39.0	10.8	-49.2	28.9	-64.7
DGSM: BP86/6-31G** SPE: MP2/cc-pVTZ	122.4	-66.6	18.3	-16.2	30.5	-66.5
DGSM: BP86/6-31G** SPE: MP2/def2-TZVP	117.1	-68.3	14.5	-21.3	31.3	-69.8
DGSM: B3LYP/6-31G** SPE: MP2/def2-TZVP	116.1	-64.0	13.2	-16.5	28.3	-68.6

We have tested the effects of basis set size and level of theory on the GSM pathway by computing three pathways using different basis sets and different levels of theory. We make the following observations:

1. The GSM pathway is not greatly affected by the size of the basis set used in generating the pathway (Appendix Figure 1a), i.e., one can use a small 6-31G** basis set to generate the pathway, but use a larger def2-TZVP or cc-pVTZ to compute the single point energies.
2. The GSM pathway does not depend greatly on the level of theory used to generate the geometries. That is, GSM generated with the BP86 functional is very similar to that generated with the B3LYP functional, giving similar single point energies for the same level of theory. For example, BP86 pathway evaluated at B3LYP single point energies is almost identical with the energies generated from the B3LYP pathway. Likewise, BP86 and B3LYP generated pathways have almost identical energies when evaluated at the MP2 level of theory.
3. The level of theory does impact the transition state energies and the product energies relative to the initial states. However, there are no trends across three pathways. In one

case, the MP2 energies are in good agreement with the B3LYP energies, but are different from BP86 (Appendix Figure 2b). In another case, BP86 and B3LYP are in relatively good agreement with MP2 being different (Appendix Figure 3). In the third case, the barriers are different for each of the three levels of theory tested (Appendix Figure 1b).

4. The magnitude of the differences in the transition state energies due to the level of theory are <12 kJ for barriers of 40 kJ/mol or less and about 20 kJ/mol for barriers of about 100 kJ/mol. We consider these errors to be acceptable.

Appendix A.2 Bond Distances

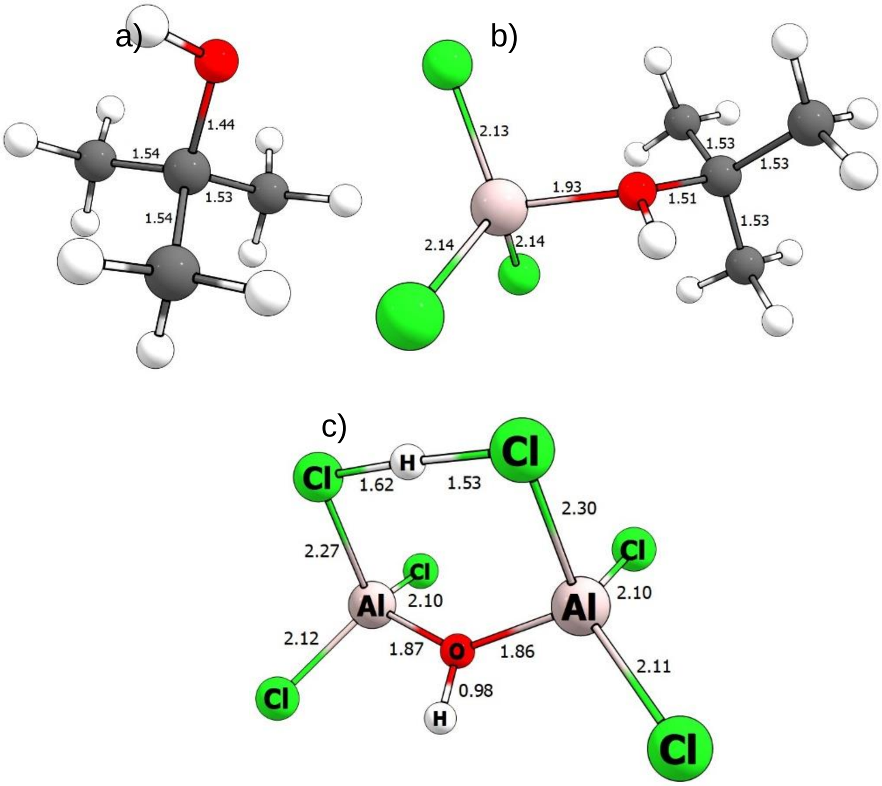

Appendix Figure 4. Labeled bond distance structure of a) tert-butanol, b) ($AlCl_3OH$)(IBH) complex , and c) complex 1. All bond distances are in Å. C-H bond distances are omitted.

Appendix A.3 Propagation Reaction with $AlCl_3OH_2$

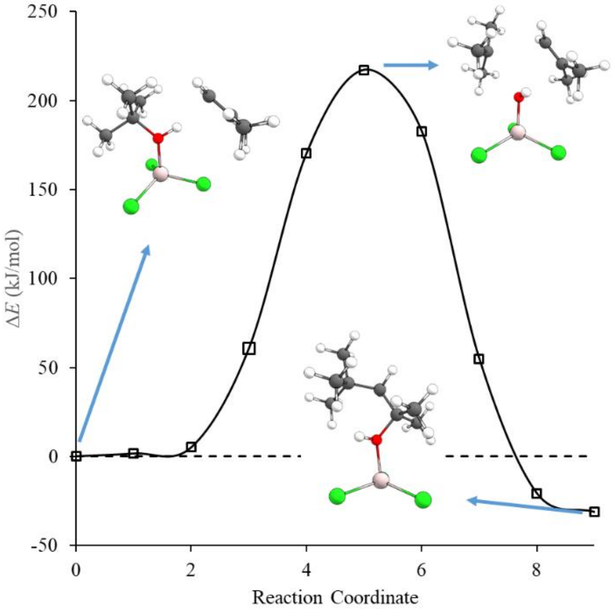

Appendix Figure 5. Potential energy surface (PES) for the propagation reaction with $AlCl_3OH_2$. E_a = 217.2 kJ/mol E_{rxn} = -31.3 kJ/mol

From the figure above, the high reaction barrier is associated with the breaking of the C-O bonds.

Appendix A.4 Reaction Pathway with $AlCl_3/H_2O$ Complexes

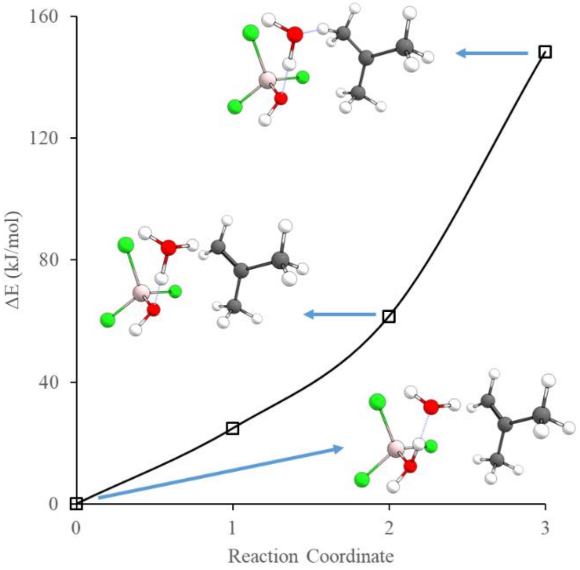

Appendix Figure 6. PES for the initiation reaction with $AlCl_3(OH_2)_2$.

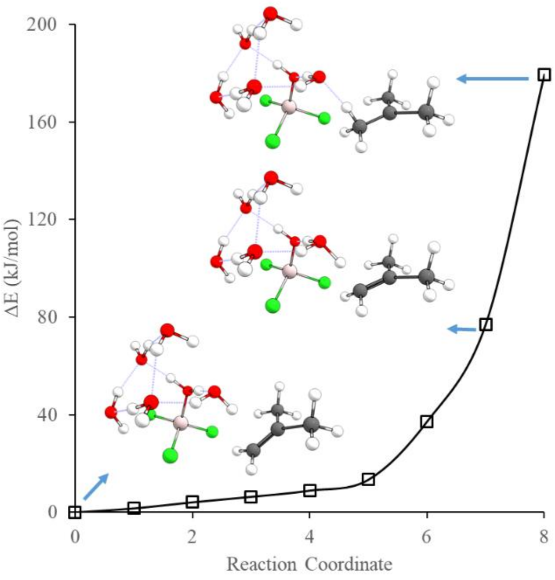

Appendix Figure 7. PES for the initiation reaction with $AlCl_3(OH_2)_6$.

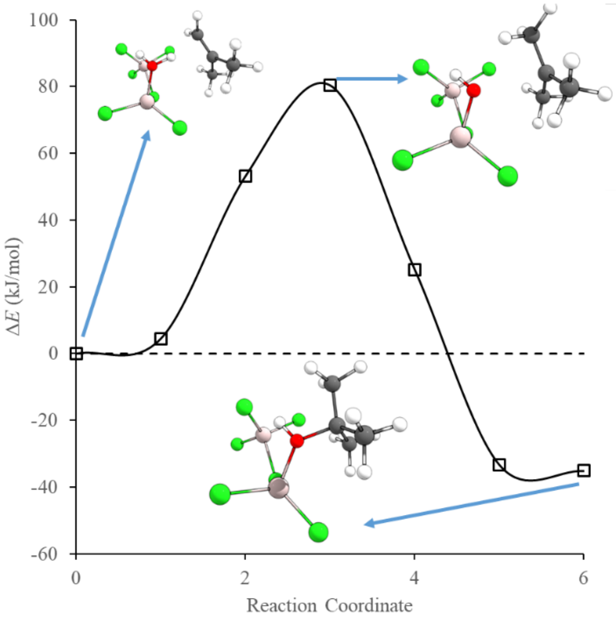

Appendix Figure 8. PES for the initiation reaction with $(AlCl_3)_2OH_2$. E_a = 80.3 kJ/mol E_{rxn} = -35.2 kJ/mol.

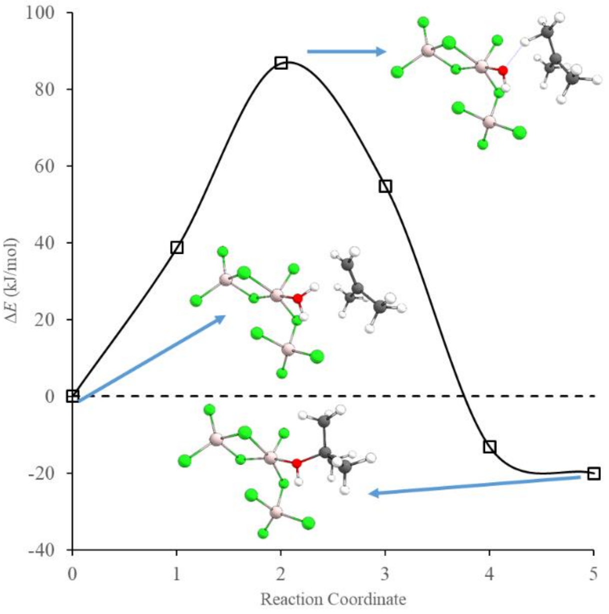

Appendix Figure 9. PES for the initiation reaction with $(AlCl_3)_3OH_2$. E_a = 86.8 kJ/mol E_{rxn} = -20.1 kJ/mol

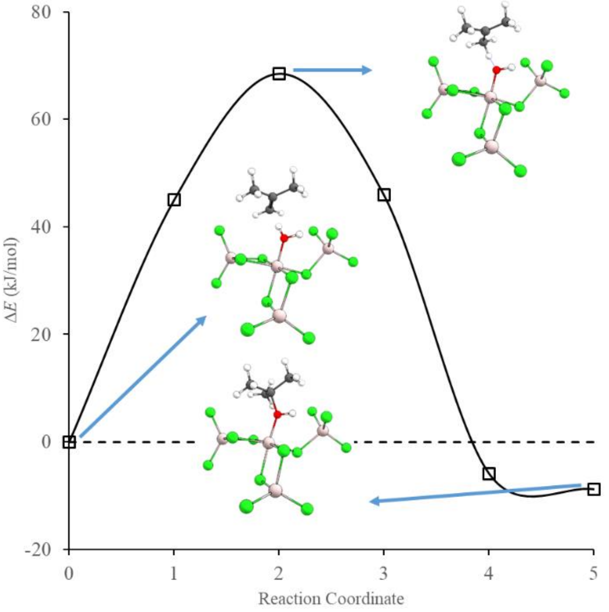

Appendix Figure 10. PES for the initiation reaction with $(AlCl_3)_4OH_2$. E_a = 68.6 kJ/mol E_{rxn} = -8.8 kJ/mol

Appendix A.5 Propagation Reaction Pathway with Complex 1 via Syn-addition

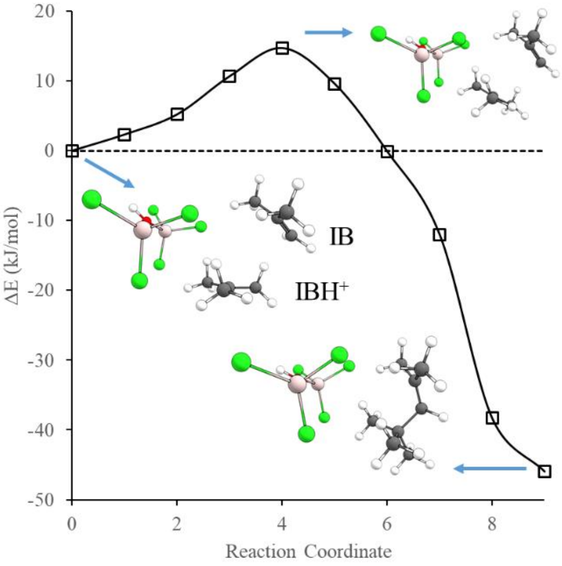

Appendix Figure 11. PES for the propagation reaction via syn-addition with complex 1. E_a = 14 kJ/mol and E_{rxn} = -46.0 kJ/mol

Appendix A.6 Reaction Pathway of IB + IBH^+

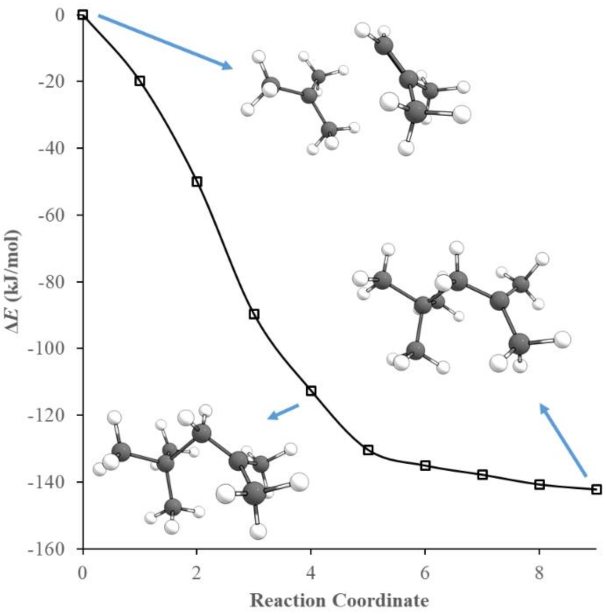

Appendix Figure 12. PES for the reaction of IB + IBH^+

Appendix A.7 pK_a Comparison

We have computed pK_a values for some of the initiator complexes identified in this work as a way to rank the relative acidity of the complexes. The relative pK_a values should be informative, even though the reaction occurs in a very non-polar solvent. The pKa was computed from:

$$\mathrm{p}K_\mathrm{a} = \frac{\Delta G^*_\mathrm{aq}}{2.303 \cdot RT}$$

where ΔG^*_aq is the aqueous-phase free energy (implicit solvent), R is the gas constant, and T is the temperature in Kelvin. Solvation effects were approximated with the COSMO continuum solvation model[86] as implemented in ORCA. Please refer to ref [87-88] for detailed discussion on ΔG^*_aq and pK_a calculations. We have also computed pK_a(vacuum), by using the gas-phase free energy in the above equations. Table 6 summarizes the pK_a for the initiator complexes we studied and, for reference, the pK_a for IBH^+.

Appendix Table 2. pK_a for initiator complexes studied

Reaction	ΔG_{aq} (kcal/mol)	ΔG_{gas} (kcal/mol)	pK_a	pK_a (vacuum)
$AlCl_3OH_2 \rightarrow [AlCl_3OH]^- + H^+$	-8.0	293.0	-5.8	215.0
$(AlCl_3)_2OH_2 \rightarrow [(AlCl_3)_2OH]^- + H^+$	-18.8	278.8	-13.8	204.5
$(AlCl_3)_3OH_2 \rightarrow [(AlCl_3)_3OH]^- + H^+$	-20.5	268.8	-15.0	197.2
$(AlCl_3)_4OH_2 \rightarrow [(AlCl_3)_4OH]^- + H^+$	-16.2	273.2	-11.9	200.4
Complex 1 $\rightarrow [AlCl_3(OH)AlCl_3]^- + H^+$	-41.1	255.5	-30.1	187.4
$IBH^+ \rightarrow IB + H^+$	-16.0	190.8	-11.7	140.0

From Table 6 we see that the proton is very weakly bound to the chlorines in complex **1** and is about 24 orders of magnitude more acidic than the proton on the $AlCl_3OH_2$ complex, and thus can give up a proton much more easily. The very negative value of pK_a for **1** indicates that this complex is not stable in water, which is certainly the case since $AlCl_3$ will convert to $Al(OH)_3$ in the aqueous phase. In contrast, the large positive value of pK_a(vacuum) for **1**, coupled with our AIMD simulations of **1** in a non-polar solvent indicate that it is stable under non-aqueous conditions. Note that ΔG_{gas} for IBH^+ is less positive than any of the initiators because the initial structure is a cation.

Appendix A.8 AIMD Simulation Summary

Appendix Table 3. Summary of isothermal-isochoric ensemble simulation performed with different initiator complexes

Temperature (K)	**Initiator Complex**	**Number of Additional H_2O**	**Number of IB**	**Observation**
300	$AlCl_3OH_2$	0	10	No reaction was observed
1000	$AlCl_3OH_2$	0	10	no reaction was observed
1500	$AlCl_3OH_2$	0	10	Proton transfer from the complex to an IB at around 2500 fs, but transfer back to the complex at around 4500 fs
1000	$(AlCl_3)_2OH_2$	4	6	The complex dissociated into two $AlCl_3$ molecules
1000	$(AlCl_3)_3OH_2$	6	7	The complex dissociated and form three $AlCl_3OH_2$
1000	Complex **1**	0	7	Proton transfer was observed and it remained on the IB
300	Complex **1**	0	7	Proton transfer was observed and it remained on the IB

Appendix A.9 Coordinates of Initiator Complex

11

Complex **1**

Al	2.06106707012648	-1.36470708737372	-0.83720778255019
Cl	4.17453629919369	-2.20479813586948	-0.82509090153621
Cl	1.88340591314082	0.00278060683818	-2.41930510447285
Cl	1.49419709903235	-0.82025392352095	1.12733259326101
O	1.11521798698605	-2.93686312593136	-1.14132394329954
H	3.79089739074371	-3.73131071483528	-0.99929556230111
H	0.43696435312836	-3.09446284398166	-0.45344617050688
Cl	3.28357914662869	-5.18869819729116	-1.21494266378787
Al	1.41260892346512	-4.38984253557593	-2.25107699452121
Cl	1.98905003751391	-3.66891910251454	-4.13663678696029
Cl	-0.16725821995917	-5.74791593994410	-1.93943768332486

19

AlCl3OH2

Al	1.952614	-0.447947	-0.357332
Cl	3.498322	-0.253353	1.089801
Cl	2.060443	0.882798	-2.019293
Cl	-0.006263	-0.929768	0.298100
O	2.522751	-2.142740	-1.164068
H	3.489122	-2.226763	-1.292701
H	2.078257	-2.381712	-2.006090

23

(AlCl3)2OH2

Al	1.979436	-5.726311	0.692126
Cl	5.453947	-4.608104	1.398260
Cl	0.378846	-6.475726	-0.472015
Cl	1.901005	-5.800445	2.789294
Cl	4.670771	-1.127618	0.915167
Cl	2.332685	-3.588166	-0.000780
Al	4.618301	-3.068722	0.103364
Cl	5.273490	-3.333082	-1.906917
O	3.540800	-6.559230	0.136524
H	4.356114	-6.144983	0.558173
H	3.759098	-6.731047	-0.860693

```
27
 (AlCl3)3OH2
  Al -0.830650 1.424719 7.516728
  Al -1.011800 4.708856 7.328613
  Cl 2.095521 -1.562213 7.553414
  Cl -1.041326 3.239958 9.049182
  Cl -0.773714 3.050812 5.797189
  Cl -2.880537 5.649726 7.111578
  Cl 0.758997 5.848879 7.396085
  Al 1.811471 0.035798 8.982688
  Cl -0.359413 0.014495 9.487730
  Cl -2.926638 0.928020 7.453217
  Cl 1.652757 1.854476 7.716541
  Cl 3.094448 0.145836 10.635018
  O -0.261577 0.067096 6.298950
  H -0.953996 -0.617039 5.990704
  H 0.584552 -0.437232 6.440258
```

```
31
 (AlCl3)4OH2
  Al 0.140463 2.225162 -0.457958
  Cl -0.751289 3.888472 0.940072
  Cl 0.999213 3.979363 -1.814865
  Cl -1.727474 2.214126 -1.846673
  Cl 2.183956 2.297717 0.833210
  Cl 1.258515 0.656892 -1.817059
  Cl -3.423409 1.207750 1.072905
  Al 0.145062 5.520370 -0.379158
  Al 3.224065 1.059363 -0.731735
  Al -3.394600 0.795681 -1.074744
  Cl 1.708562 6.469651 0.653552
  Cl -1.390292 6.602712 -1.313757
  Cl 4.482946 2.224583 -1.941735
  Cl 3.938807 -0.732369 0.130896
  Cl -5.124641 1.420089 -2.096433
  Cl -2.636414 -1.162117 -1.435199
  O -0.489641 0.912075 0.698016
  H -0.182613 -0.073417 0.706915
  H -1.454821 0.954001 0.994734
```

Appendix B Impact of Defects on the Decomposition of Chemical Warfare Agent Simulants in Zr-based Metal Organic Frameworks

Appendix B.1 Reaction in Periodic System

Appendix B.1.1 1-defect UiO-67

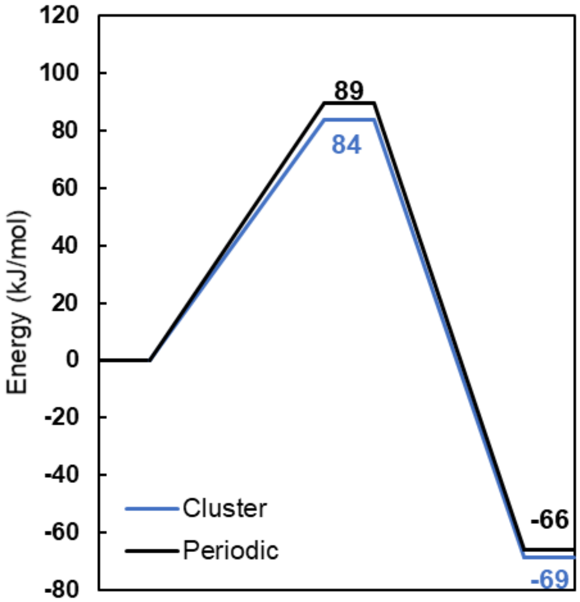

Appendix Figure 13. Cluster and periodic energy reaction paths for DMMP hydrolysis via adjacent OH elimination with one missing linker defect UiO-67

Appendix B.1.2 2-defect UiO-67

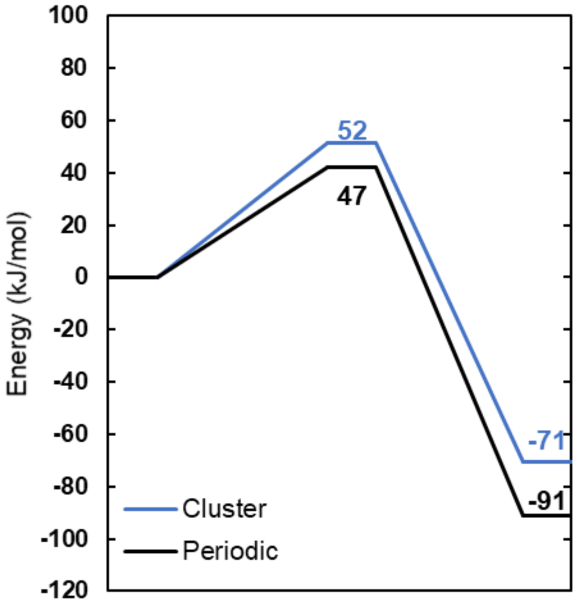

Appendix Figure 14. Cluster and periodic energy reaction paths for DMMP hydrolysis via μ3-OH elimination with 2-defect UiO-67

Appendix B.2 PCN-700 Topology

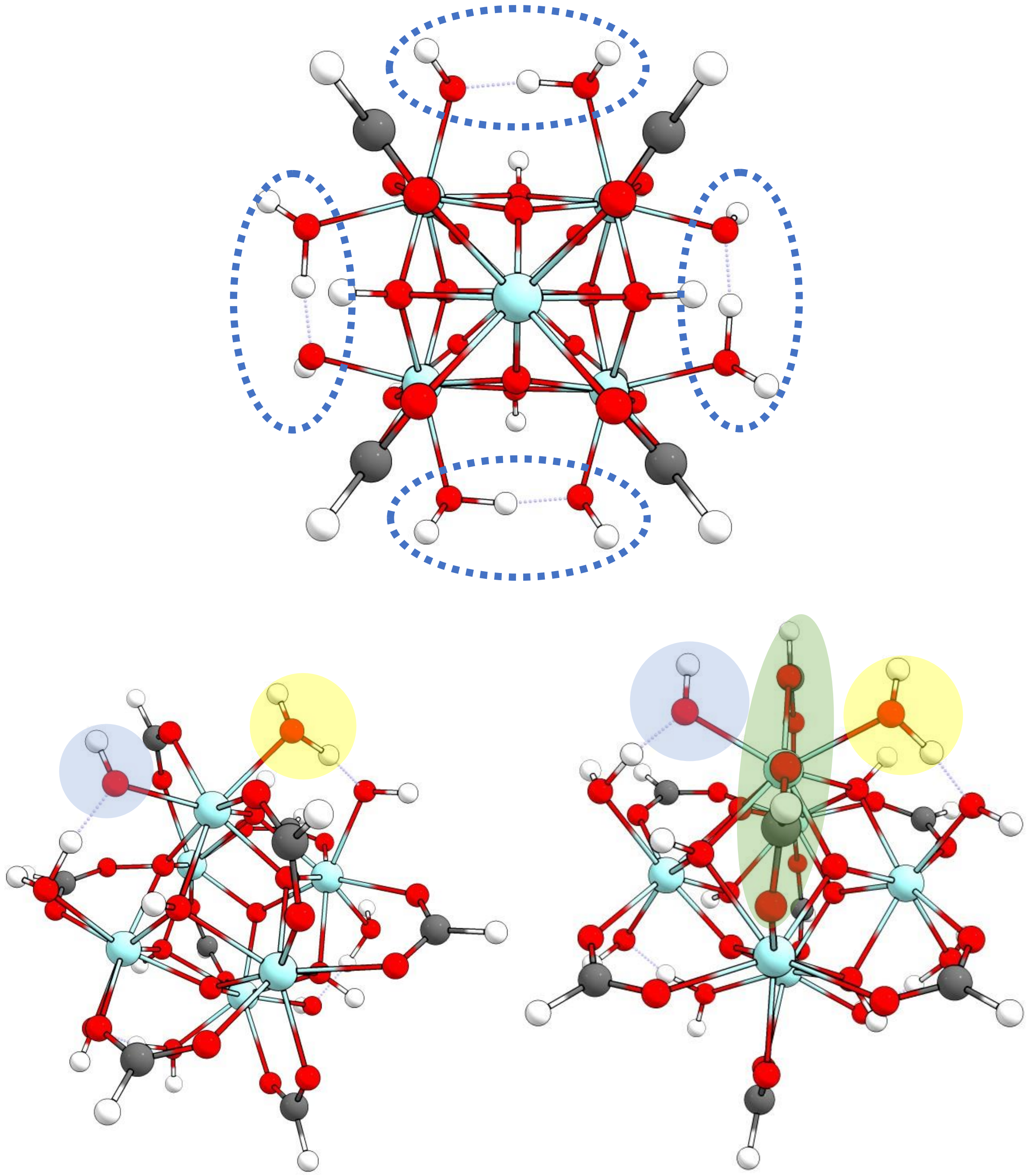

Appendix Figure 15. Topology of pristine PCN-700. Dotted blue outlines show pairs of OH and water molecules occupy the undercoordinated sites. Shaded yellow areas show the location that DMMP would adsorb to reaction with the OH groups (shaded blue) to follow the 2-adjacent missing linker UiO-67 pathway. The shaded green area shows the linkers that sterically hinder the 2-djacent missing linker pathway.

From the Figure above, visibly, the undercoordinated Zr-site are located at the equatorial position with respect to each other (dotted blue). In order to follow the 2-adjacent missing linker OH elimination pathway, the DMMP will need to adsorb on the same Zr as the reacting OH group (blue) by displacing the water (yellow). However, their interaction would be sterically hindered because of the pair of linkers (green) exist between them. Consequently, we concluded that the 2-adjacent missing linker OH elimination is not feasible on PCNC-700.

Appendix C Method for Predicting Dipole Moments of Complex Molecules for Use in Thermophysical Property Estimation

Appendix C.1 CONFAB Modification

CONFAB relies on SMARTS to assign values to particular rotatable bonds. We, however, found that CONFAB failed to generate a comprehensive set of configurations for molecules containing rotatable C-O and O-H bonds. To overcome this, we made the following modification to the data/torlib.txt file:

1. Deleted all SMARTS string
2. Replace:

```
SP3-SP3  60.0  -60.0 180.0
SP2-SP2   0.0  180.0 -30.0 30.0 150.0 -150.0
SP3-SP2   0.0   30.0 -30.0 60.0 -60.0  120.0 -120.0 -150.0 150.0 180.0 -90.0 90.0
```

with

```
SP3-SP3  0.0 60.0  -60.0 180.0
SP2-SP2   0.0  180.0 -30.0 30.0 150.0 -150.0
SP3-SP2   0.0 15.0 -15.0 45.0 -45.0 75.0 -75.0 105.0 -105.0 135.0 -135.0 165.0 -165.0 30.0 -30.0 60.0 -60.0  120.0 -120.0 -150.0 150.0 180.0 -90.0 90.0
```

Appendix C.2 Dimethyl Carbonate Bond Rotation Energy

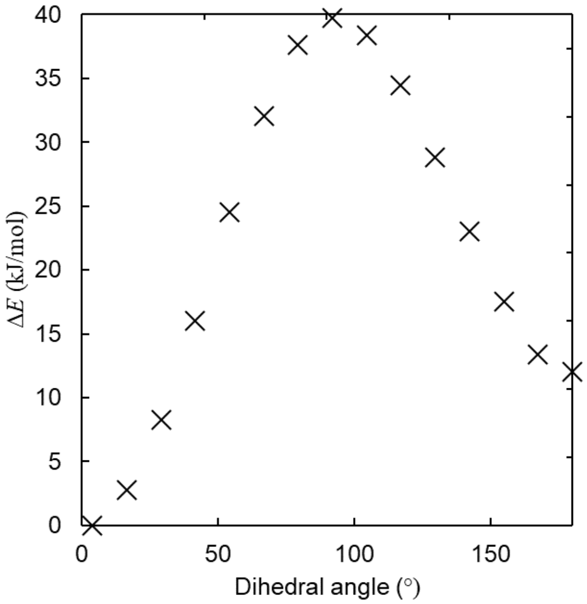

Appendix Figure 16. Potential energy surface of rotating the methyl group in dimethyl carbonate along the dihedral angle to transform cis-cis to cis-trans configuration.

Appendix C.3 AIMD Results

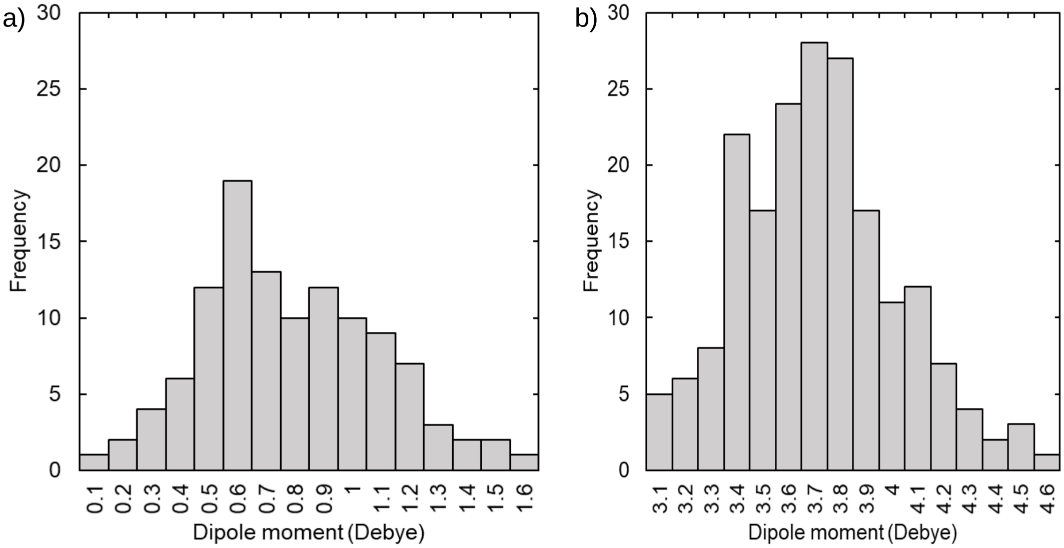

Appendix Figure 17. Distribution of dimethyl carbonate dipole moment from AIMD simulation. (a) starting with cis-cis configuration (b) cis-trans configuration

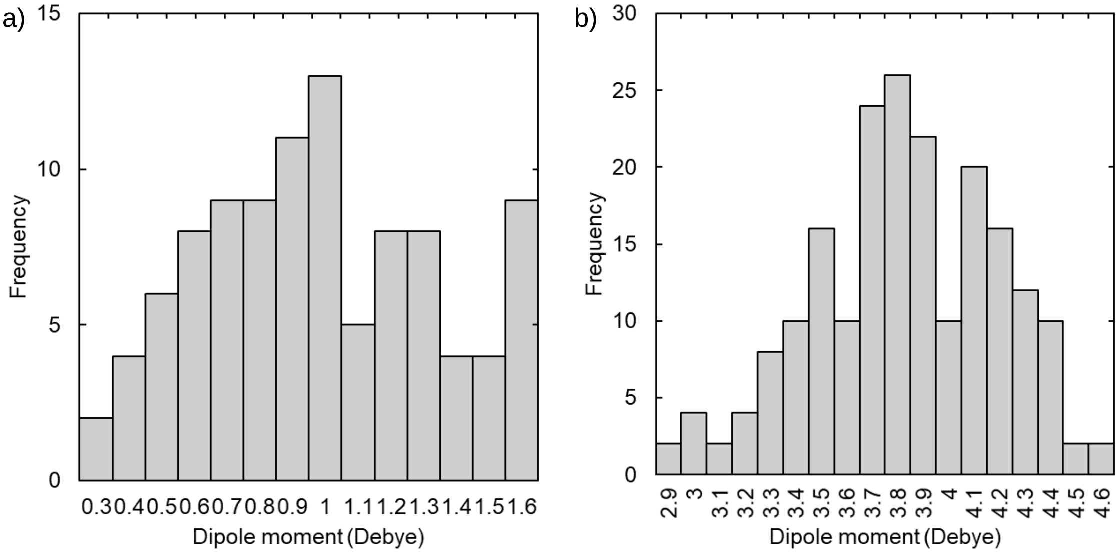

Appendix Figure 18. Distribution of diethyl carbonate dipole moment from AIMD simulation(a) starting with cis-cis configuration (b) cis-trans configuration

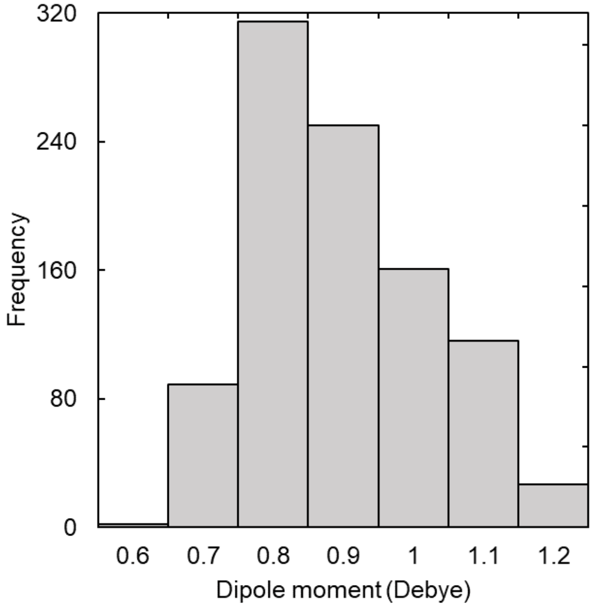

Appendix Figure 19. Distribution of di-n-propyl ether dipole moment from AIMD simulation

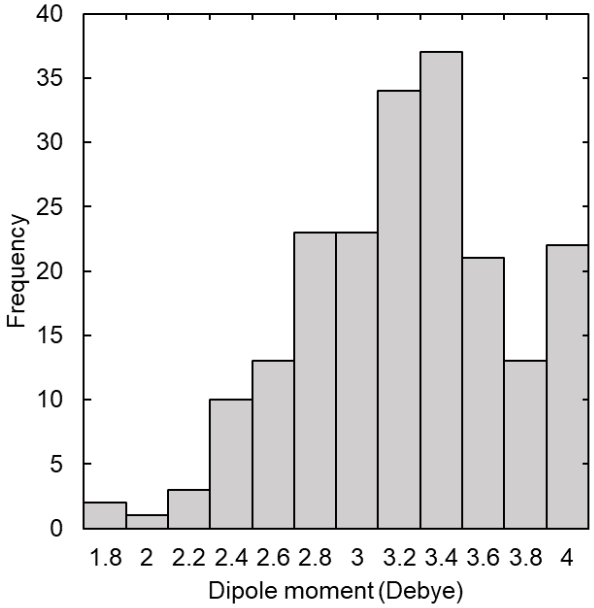

Appendix Figure 20. Distribution of sulfurous acid dimethyl ester dipole moment from AIMD simulation

Appendix C.4 Thermophysical Properties

Appendix Table 4. Estimated Vapor Viscosities (cP) from the Lucas method

Temp	**Dimethyl carbonate**			**Diethyl carbonate**			**Diethyl ether**			**Dimethyl ether**			**Methyl acetate**			**Ethyl acetate**			**Methyl ethyl ketone**		
°C	Exp	Cal	$\mu = 0$	Exp	Cal	$\mu = 0$	Exp	Cal	$\mu = 0$	Exp	Cal	$\mu = 0$	Exp	Cal	$\mu = 0$	Exp	Cal	$\mu = 0$	Exp	Cal	$\mu = 0$
0	72.1	72.1	72.1	64.6	64.6	64.6	68.4	68.4	68.4	86.1	86.1	84.0	81.7	81.7	73.6	75.7	75.7	67.6	70.8	70.8	63.2
10	74.7	74.7	74.7	66.9	66.9	66.9	70.9	70.9	70.9	89.3	89.3	87.1	84.7	84.7	76.3	78.5	78.5	70.0	73.4	73.4	65.5
20	77.3	77.3	77.3	69.2	69.2	69.2	73.4	73.4	73.4	92.4	92.4	90.2	87.7	87.7	79.0	81.2	81.2	72.5	76.0	76.0	67.8
30	80.0	80.0	80.0	71.5	71.5	71.5	76.0	76.0	76.0	95.6	95.6	93.3	90.7	90.7	81.7	84.0	84.0	75.0	78.5	78.5	70.1
40	82.6	82.6	82.6	73.9	73.9	73.9	78.5	78.5	78.5	98.7	98.7	96.3	93.7	93.7	84.4	86.8	86.8	77.4	81.1	81.1	72.4
50	85.2	85.2	85.2	76.2	76.2	76.2	81.0	81.0	81.0	101.9	101.9	99.4	96.7	96.7	87.1	89.5	89.5	79.9	83.7	83.7	74.7
60	87.9	87.9	87.9	78.6	78.6	78.6	83.5	83.5	83.5	105.0	105.0	102.4	99.7	99.7	89.8	92.3	92.3	82.4	86.3	86.3	77.0
70	90.5	90.5	90.5	81.0	81.0	81.0	86.0	86.0	86.0	108.1	108.1	105.4	102.7	102.7	92.5	95.1	95.1	84.9	88.9	88.9	79.4
80	93.2	93.2	93.2	83.3	83.3	83.3	88.5	88.5	88.5	111.2	111.2	108.5	105.7	105.7	95.2	97.9	97.9	87.4	91.5	91.5	81.7
90	95.8	95.8	95.8	85.7	85.7	85.7	91.0	91.0	91.0	114.2	114.2	111.5	108.7	108.7	97.9	100.7	100.7	89.9	94.1	94.1	84.0
100	98.5	98.5	98.5	88.1	88.1	88.1	93.5	93.5	93.5	117.3	117.3	114.4	111.7	111.7	100.6	103.4	103.4	92.3	96.7	96.7	86.3
110	101.1	101.1	101.1	90.4	90.4	90.4	96.0	96.0	96.0	120.3	120.3	117.4	114.6	114.6	103.3	106.2	106.2	94.8	99.3	99.3	88.7
120	103.8	103.8	103.8	92.8	92.8	92.8	98.5	98.5	98.5	123.3	123.3	120.4	117.6	117.6	106.0	109.0	109.0	97.3	101.9	101.9	91.0
130	106.4	106.4	106.4	95.2	95.2	95.2	100.9	100.9	100.9	126.4	126.4	123.3	120.6	120.6	108.6	111.8	111.8	99.7	104.5	104.5	93.3
140	109.0	109.0	109.0	97.5	97.5	97.5	103.4	103.4	103.4	129.3	129.3	126.2	123.6	123.6	111.3	114.5	114.5	102.2	107.1	107.1	95.6
150	111.7	111.7	111.7	99.9	99.9	99.9	105.8	105.8	105.8	132.3	132.3	129.1	126.5	126.5	114.0	117.3	117.3	104.7	109.7	109.7	97.9
160	114.3	114.3	114.3	102.3	102.3	102.3	108.3	108.3	108.3	135.3	135.3	132.0	129.5	129.5	116.6	120.0	120.0	107.1	112.2	112.2	100.2
170	116.9	116.9	116.9	104.6	104.6	104.6	110.7	110.7	110.7	138.2	138.2	134.8	132.4	132.4	119.3	122.7	122.7	109.5	114.8	114.8	102.5
180	119.5	119.5	119.5	107.0	107.0	107.0	113.1	113.1	113.1	141.1	141.1	137.7	135.3	135.3	121.9	125.5	125.5	112.0	117.4	117.4	104.8
190	122.1	122.1	122.1	109.3	109.3	109.3	115.5	115.5	115.5	144.0	144.0	140.5	138.2	138.2	124.5	128.2	128.2	114.4	119.9	119.9	107.0

Appendix Table 4 (continued)

200	124.7	124.7	124.7	111.6	111.6	111.6	117.9	117.9	117.9	146.9	146.9	143.3	141.1	141.1	127.1	130.9	130.9	116.8	122.5	122.5	109.3
210	127.3	127.3	127.3	114.0	114.0	114.0	120.2	120.2	120.2	149.7	149.7	146.1	144.0	144.0	129.7	133.6	133.6	119.2	125.0	125.0	111.6
220	129.9	129.9	129.9	116.3	116.3	116.3	122.6	122.6	122.6	152.5	152.5	148.8	146.9	146.9	132.3	136.2	136.2	121.6	127.5	127.5	113.8
230	132.4	132.4	132.4	118.6	118.6	118.6	124.9	124.9	124.9	155.4	155.4	151.6	149.8	149.8	134.9	138.9	138.9	124.0	130.0	130.0	116.0
240	135.0	135.0	135.0	120.9	120.9	120.9	127.3	127.3	127.3	158.2	158.2	154.3	152.6	152.6	137.4	141.6	141.6	126.4	132.5	132.5	118.3
250	137.5	137.5	137.5	123.2	123.2	123.2	129.6	129.6	129.6	160.9	160.9	157.0	155.4	155.4	140.0	144.2	144.2	128.7	135.0	135.0	120.5
260	140.1	140.1	140.1	125.5	125.5	125.5	131.9	131.9	131.9	163.7	163.7	159.7	158.2	158.2	142.5	146.8	146.8	131.1	137.5	137.5	122.7
270	142.6	142.6	142.6	127.8	127.8	127.8	134.2	134.2	134.2	166.4	166.4	162.4	161.1	161.1	145.1	149.5	149.5	133.4	139.9	139.9	124.9
280	145.1	145.1	145.1	130.1	130.1	130.1	136.5	136.5	136.5	169.2	169.2	165.1	163.8	163.8	147.6	152.1	152.1	135.7	142.4	142.4	127.1
290	147.6	147.6	147.6	132.3	132.3	132.3	138.7	138.7	138.7	171.9	171.9	167.7	166.6	166.6	150.1	154.7	154.7	138.0	144.8	144.8	129.3
300	150.1	150.1	150.1	134.6	134.6	134.6	141.0	141.0	141.0	174.5	174.5	170.3	169.4	169.4	152.6	157.2	157.2	140.4	147.3	147.3	131.4

Appendix Table 5. Vapor viscosities (cP) computed from the Chung et al. method

Temp	Dimethyl carbonate			Diethyl carbonate			Diethyl ether			Dimethyl ether			Methyl acetate			Ethyl acetate			Methyl ethyl ketone		
°C	Exp	Cal	μ = 0	Exp	Cal	μ = 0	Exp	Cal	μ = 0	Exp	Cal	μ = 0	Exp	Cal	μ = 0	Exp	Cal	μ = 0	Exp	Cal	μ = 0
0	76.1	76.0	76.0	65.3	65.3	65.3	71.9	71.9	71.8	93.0	93.0	92.4	85.9	86.2	85.0	71.6	71.8	71.1	70.6	71.1	67.1
10	78.9	78.9	78.9	67.7	67.7	67.7	74.7	74.6	74.5	96.5	96.5	95.9	89.1	89.4	88.2	74.3	74.5	73.7	73.3	73.8	69.7
20	81.8	81.7	81.7	70.2	70.1	70.1	77.4	77.3	77.3	100.0	100.0	99.4	92.4	92.7	91.4	77.0	77.2	76.4	76.0	76.5	72.2
30	84.7	84.6	84.6	72.6	72.6	72.6	80.1	80.1	80.0	103.5	103.5	102.8	95.6	95.9	94.6	79.7	79.9	79.1	78.6	79.1	74.7
40	87.6	87.5	87.4	75.1	75.0	75.0	82.8	82.8	82.7	106.9	107.0	106.3	98.9	99.2	97.8	82.5	82.6	81.8	81.3	81.8	77.3
50	90.4	90.3	90.3	77.6	77.5	77.5	85.6	85.5	85.4	110.4	110.5	109.7	102.1	102.5	101.0	85.2	85.4	84.5	84.0	84.5	79.8
60	93.3	93.2	93.2	80.0	80.0	80.0	88.3	88.2	88.1	113.9	113.9	113.2	105.4	105.7	104.3	87.9	88.1	87.2	86.7	87.2	82.4
70	96.2	96.1	96.1	82.5	82.5	82.4	91.0	91.0	90.9	117.3	117.4	116.6	108.7	109.0	107.5	90.6	90.8	89.9	89.3	89.9	84.9
80	99.1	99.0	99.0	85.0	84.9	84.9	93.7	93.7	93.6	120.7	120.8	120.0	111.9	112.3	110.7	93.4	93.6	92.6	92.0	92.6	87.5
90	102.0	101.9	101.9	87.5	87.4	87.4	96.4	96.4	96.3	124.1	124.2	123.3	115.2	115.6	114.0	96.1	96.3	95.3	94.7	95.4	90.0
100	104.9	104.8	104.8	90.0	89.9	89.9	99.1	99.1	99.0	127.5	127.6	126.7	118.4	118.8	117.2	98.8	99.0	98.0	97.4	98.1	92.6
110	107.8	107.7	107.7	92.4	92.4	92.4	101.8	101.8	101.6	130.8	130.9	130.0	121.7	122.1	120.4	101.5	101.7	100.7	100.1	100.8	95.1
120	110.7	110.6	110.6	94.9	94.9	94.9	104.5	104.4	104.3	134.2	134.3	133.4	124.9	125.3	123.6	104.2	104.5	103.4	102.8	103.5	97.7
130	113.6	113.5	113.4	97.4	97.4	97.4	107.1	107.1	107.0	137.5	137.6	136.7	128.2	128.6	126.8	106.9	107.2	106.1	105.4	106.2	100.2
140	116.5	116.3	116.3	99.9	99.8	99.8	109.8	109.8	109.6	140.8	140.9	139.9	131.4	131.8	130.0	109.6	109.9	108.8	108.1	108.8	102.8
150	119.3	119.2	119.2	102.4	102.3	102.3	112.4	112.4	112.3	144.1	144.2	143.2	134.6	135.0	133.2	112.3	112.6	111.4	110.8	111.5	105.3
160	122.2	122.1	122.1	104.9	104.8	104.8	115.1	115.0	114.9	147.3	147.4	146.4	137.8	138.2	136.3	115.0	115.3	114.1	113.4	114.2	107.8
170	125.1	124.9	124.9	107.3	107.3	107.3	117.7	117.6	117.5	150.5	150.6	149.6	141.0	141.4	139.5	117.7	117.9	116.7	116.1	116.9	110.3
180	127.9	127.8	127.8	109.8	109.7	109.7	120.3	120.2	120.1	153.7	153.8	152.8	144.1	144.6	142.6	120.3	120.6	119.4	118.7	119.5	112.8
190	130.8	130.6	130.6	112.3	112.2	112.2	122.9	122.8	122.7	156.9	157.0	155.9	147.3	147.8	145.7	123.0	123.3	122.0	121.4	122.2	115.3
200	133.6	133.5	133.4	114.7	114.6	114.6	125.4	125.4	125.3	160.0	160.1	159.0	150.4	150.9	148.8	125.6	125.9	124.6	124.0	124.8	117.8
210	136.4	136.3	136.3	117.2	117.1	117.1	128.0	127.9	127.8	163.2	163.3	162.1	153.6	154.1	151.9	128.3	128.6	127.2	126.6	127.4	120.3
220	139.2	139.1	139.1	119.6	119.5	119.5	130.5	130.5	130.3	166.2	166.4	165.2	156.7	157.2	155.0	130.9	131.2	129.8	129.2	130.0	122.8
230	142.0	141.9	141.9	122.0	121.9	121.9	133.1	133.0	132.9	169.3	169.4	168.3	159.8	160.3	158.1	133.5	133.8	132.4	131.8	132.6	125.2
240	144.8	144.7	144.7	124.4	124.4	124.4	135.6	135.5	135.4	172.4	172.5	171.3	162.9	163.4	161.1	136.1	136.4	135.0	134.3	135.2	127.7
250	147.6	147.4	147.4	126.8	126.8	126.8	138.1	138.0	137.9	175.4	175.5	174.3	165.9	166.5	164.1	138.7	139.0	137.5	136.9	137.8	130.1
260	150.4	150.2	150.2	129.2	129.2	129.2	140.5	140.5	140.3	178.4	178.5	177.3	169.0	169.5	167.2	141.2	141.5	140.1	139.4	140.4	132.5

Appendix Table 5 (continued)

270	153.1	152.9	152.9	131.6	131.6	131.6	143.0	142.9	142.8	181.4	181.5	180.3	172.0	172.5	170.1	143.8	144.1	142.6	142.0	142.9	135.0
280	155.8	155.7	155.7	134.0	133.9	133.9	145.4	145.4	145.2	184.3	184.5	183.2	175.0	175.6	173.1	146.3	146.6	145.1	144.5	145.5	137.3
290	158.6	158.4	158.4	136.4	136.3	136.3	147.9	147.8	147.6	187.3	187.4	186.1	178.0	178.6	176.1	148.8	149.2	147.6	147.0	148.0	139.7
300	161.3	161.1	161.1	138.7	138.7	138.7	150.3	150.2	150.1	190.2	190.3	189.0	181.0	181.5	179.0	151.3	151.7	150.1	149.5	150.5	142.1

Appendix Table 6. Vapor viscosities (cP) computed from the Reichenberg method

Temp	Dimethyl carbonate			Diethyl carbonate			Diethyl ether			Dimethyl ether			Methyl acetate			Ethyl acetate			Methyl ethyl ketone		
°C	Exp	Cal	μ = 0	Exp	Cal	μ = 0	Exp	Cal	μ = 0	Exp	Cal	μ = 0	Exp	Cal	μ = 0	Exp	Cal	μ = 0	Exp	Cal	μ = 0
0	70.1	70.1	70.1	80.3	80.3	80.3	68.4	68.4	68.4	85.9	85.9	85.9	75.2	75.2	75.2	75.2	75.2	75.2	67.4	67.3	67.6
10	72.7	72.7	72.7	83.3	83.3	83.3	70.9	70.9	70.9	88.9	88.9	88.9	78.0	78.0	78.0	78.0	78.0	78.0	69.8	69.8	70.0
20	75.3	75.3	75.3	86.2	86.2	86.2	73.4	73.4	73.4	92.0	92.0	92.0	80.7	80.7	80.7	80.7	80.7	80.7	72.3	72.3	72.5
30	77.8	77.8	77.8	89.2	89.2	89.2	75.8	75.8	75.8	95.1	95.1	95.1	83.4	83.4	83.5	83.4	83.4	83.5	74.8	74.7	75.0
40	80.4	80.4	80.4	92.1	92.1	92.1	78.3	78.3	78.3	98.1	98.1	98.1	86.2	86.2	86.2	86.2	86.2	86.2	77.3	77.2	77.4
50	82.9	82.9	82.9	95.0	95.0	95.0	80.8	80.8	80.8	101.2	101.2	101.2	88.9	88.9	88.9	88.9	88.9	88.9	79.7	79.7	79.9
60	85.5	85.5	85.5	97.9	97.9	97.9	83.2	83.2	83.2	104.2	104.2	104.2	91.6	91.6	91.6	91.6	91.6	91.6	82.2	82.1	82.3
70	88.0	88.0	88.0	100.9	100.9	100.9	85.7	85.7	85.7	107.2	107.2	107.2	94.3	94.3	94.3	94.3	94.3	94.3	84.6	84.6	84.8
80	90.5	90.5	90.5	103.8	103.8	103.8	88.1	88.1	88.1	110.2	110.2	110.2	97.0	97.0	97.0	97.0	97.0	97.0	87.1	87.0	87.2
90	93.1	93.1	93.1	106.7	106.7	106.7	90.5	90.5	90.5	113.2	113.2	113.2	99.7	99.7	99.7	99.7	99.7	99.7	89.5	89.5	89.7
100	95.6	95.6	95.6	109.6	109.6	109.6	92.9	92.9	93.0	116.2	116.2	116.2	102.4	102.4	102.4	102.4	102.4	102.4	92.0	91.9	92.1
110	98.1	98.1	98.1	112.5	112.5	112.5	95.4	95.4	95.4	119.1	119.1	119.1	105.1	105.1	105.1	105.1	105.1	105.1	94.4	94.3	94.5
120	100.6	100.6	100.6	115.4	115.4	115.4	97.8	97.8	97.8	122.0	122.0	122.0	107.8	107.8	107.8	107.8	107.8	107.8	96.8	96.8	96.9
130	103.1	103.1	103.1	118.3	118.3	118.3	100.2	100.2	100.2	125.0	125.0	125.0	110.4	110.4	110.4	110.4	110.4	110.4	99.2	99.2	99.3
140	105.6	105.6	105.6	121.1	121.1	121.1	102.5	102.5	102.5	127.9	127.9	127.9	113.1	113.1	113.1	113.1	113.1	113.1	101.6	101.6	101.7
150	108.1	108.1	108.1	124.0	124.0	124.0	104.9	104.9	104.9	130.8	130.8	130.8	115.7	115.7	115.7	115.7	115.7	115.7	104.0	104.0	104.1
160	110.6	110.6	110.6	126.9	126.9	126.9	107.3	107.3	107.3	133.6	133.6	133.6	118.4	118.4	118.4	118.4	118.4	118.4	106.4	106.4	106.5
170	113.1	113.1	113.1	129.7	129.7	129.7	109.6	109.6	109.6	136.5	136.5	136.5	121.0	121.0	121.0	121.0	121.0	121.0	108.8	108.8	108.9
180	115.5	115.5	115.5	132.6	132.6	132.6	112.0	112.0	112.0	139.3	139.3	139.3	123.6	123.6	123.6	123.6	123.6	123.6	111.2	111.2	111.3
190	118.0	118.0	118.0	135.4	135.4	135.4	114.3	114.3	114.3	142.1	142.1	142.1	126.2	126.2	126.2	126.2	126.2	126.2	113.6	113.5	113.6

Appendix Table 6 (continued)

200	120.5	120.5	120.5	138.2	138.2	138.2	116.6	116.6	116.6	144.9	144.9	144.9	128.8	128.8	128.8	128.8	128.8	128.8	115.9	115.9	116.0
210	122.9	122.9	122.9	141.1	141.1	141.1	118.9	118.9	118.9	147.7	147.7	147.7	131.4	131.4	131.4	131.4	131.4	131.4	118.3	118.3	118.3
220	125.3	125.3	125.3	143.9	143.9	143.9	121.2	121.2	121.2	150.5	150.5	150.5	133.9	133.9	133.9	133.9	133.9	133.9	120.6	120.6	120.6
230	127.7	127.7	127.7	146.7	146.7	146.7	123.5	123.5	123.5	153.2	153.2	153.2	136.5	136.5	136.5	136.5	136.5	136.5	122.9	122.9	123.0
240	130.2	130.2	130.2	149.5	149.5	149.5	125.8	125.8	125.8	155.9	155.9	155.9	139.1	139.1	139.1	139.1	139.1	139.1	125.3	125.3	125.3
250	132.6	132.6	132.6	152.2	152.2	152.2	128.0	128.0	128.0	158.6	158.6	158.6	141.6	141.6	141.6	141.6	141.6	141.6	127.6	127.6	127.6
260	135.0	135.0	135.0	155.0	155.0	155.0	130.3	130.3	130.3	161.3	161.3	161.3	144.1	144.1	144.1	144.1	144.1	144.1	129.9	129.9	129.9
270	137.3	137.3	137.3	157.8	157.8	157.8	132.5	132.5	132.5	164.0	164.0	164.0	146.6	146.6	146.6	146.6	146.6	146.6	132.2	132.2	132.2
280	139.7	139.7	139.7	160.5	160.5	160.5	134.7	134.7	134.7	166.6	166.6	166.6	149.1	149.1	149.1	149.1	149.1	149.1	134.5	134.5	134.5
290	142.1	142.1	142.1	163.3	163.3	163.3	136.9	136.9	136.9	169.3	169.3	169.3	151.6	151.6	151.6	151.6	151.6	151.6	136.7	136.8	136.7
300	144.4	144.4	144.4	166.0	166.0	166.0	139.1	139.1	139.1	171.9	171.9	171.9	154.1	154.1	154.1	154.1	154.1	154.1	139.0	139.0	139.0

Appendix Table 7. Vapor viscosities (cP) computed from the Chapman et al. method

Temp	**Dimethyl carbonate**				**Diethyl carbonate**				**Octanoic acid**				**Maleic acid**			
°C	PURE 36*	Exp	Cal	$\mu = 0$	PURE 36*	Exp	Cal	$\mu = 0$	PURE 36*	Exp	Cal	$\mu = 0$	PURE 36*	Exp	Cal	$\mu = 0$
0	68.7	68.7	68.7	68.7	61.3	61.3	61.3	61.3	47.6	47.6	47.7	47.7	61.8	61.8	61.4	56.2
10	71.3	71.3	71.3	71.3	63.6	63.6	63.6	63.6	49.3	49.3	49.4	49.4	63.9	63.9	63.5	58.0
20	73.8	73.8	73.8	73.8	65.8	65.8	65.8	65.8	51.0	51.0	51.1	51.1	66.0	66.0	65.6	60.0
30	76.4	76.4	76.4	76.4	68.1	68.1	68.1	68.1	52.7	52.7	52.8	52.8	68.1	68.1	67.8	61.9
40	79.0	79.0	79.0	79.0	70.4	70.4	70.4	70.4	54.4	54.4	54.5	54.5	70.3	70.3	69.9	63.8
50	81.6	81.6	81.6	81.6	72.7	72.7	72.7	72.7	56.1	56.1	56.2	56.2	72.4	72.5	72.1	65.8
60	84.2	84.2	84.2	84.2	75.0	75.0	75.0	75.0	57.9	57.9	57.9	57.9	74.6	74.6	74.3	67.7
70	86.8	86.8	86.8	86.8	77.3	77.3	77.3	77.3	59.6	59.6	59.6	59.6	76.8	76.8	76.5	69.7
80	89.4	89.4	89.4	89.4	79.6	79.6	79.6	79.6	61.4	61.4	61.4	61.4	79.0	79.0	78.7	71.6
90	92.0	92.0	92.0	92.0	81.9	81.9	81.9	81.9	63.1	63.1	63.1	63.1	81.2	81.2	80.9	73.6
100	94.6	94.6	94.6	94.6	84.3	84.3	84.3	84.3	64.9	64.9	64.9	64.9	83.4	83.4	83.2	75.6
110	97.2	97.2	97.2	97.2	86.6	86.6	86.6	86.6	66.7	66.7	66.6	66.6	85.6	85.6	85.4	77.6
120	99.9	99.9	99.9	99.9	88.9	88.9	88.9	88.9	68.5	68.5	68.4	68.4	87.9	87.9	87.6	79.6
130	102.5	102.5	102.5	102.5	91.3	91.3	91.3	91.3	70.2	70.2	70.2	70.2	90.1	90.1	89.9	81.7
140	105.1	105.1	105.1	105.1	93.6	93.6	93.6	93.6	72.0	72.0	71.9	71.9	92.4	92.4	92.2	83.7
150	107.7	107.7	107.7	107.7	95.9	95.9	95.9	95.9	73.8	73.8	73.7	73.7	94.6	94.6	94.4	85.7
160	110.3	110.3	110.3	110.3	98.3	98.3	98.3	98.3	75.6	75.6	75.5	75.5	96.9	96.9	96.7	87.8
170	112.9	112.9	112.9	112.9	100.6	100.6	100.6	100.6	77.4	77.4	77.3	77.3	99.2	99.2	99.0	89.8
180	115.5	115.5	115.5	115.5	102.9	102.9	102.9	102.9	79.2	79.2	79.1	79.1	101.4	101.4	101.3	91.9
190	118.1	118.1	118.1	118.1	105.3	105.3	105.3	105.3	81.0	81.0	80.9	80.9	103.7	103.7	103.6	94.0
200	120.7	120.7	120.7	120.7	107.6	107.6	107.6	107.6	82.8	82.8	82.7	82.7	106.0	106.0	105.9	96.0
210	123.3	123.3	123.3	123.3	109.9	109.9	109.9	109.9	84.6	84.6	84.5	84.5	108.3	108.3	108.2	98.1
220	125.9	125.9	125.9	125.9	112.2	112.2	112.2	112.2	86.4	86.4	86.3	86.3	110.7	110.7	110.5	100.2
230	128.4	128.4	128.4	128.4	114.6	114.6	114.6	114.6	88.3	88.3	88.1	88.1	113.0	113.0	112.8	102.3
240	131.0	131.0	131.0	131.0	116.9	116.9	116.9	116.9	90.1	90.1	89.9	89.9	115.3	115.3	115.1	104.3
250	133.6	133.6	133.6	133.6	119.2	119.2	119.2	119.2	91.9	91.9	91.7	91.7	117.6	117.6	117.5	106.4
260	136.1	136.1	136.1	136.1	121.5	121.5	121.5	121.5	93.7	93.7	93.5	93.5	119.9	119.9	119.8	108.5

Appendix Table 7 (continued)

270	138.6	138.6	138.6	138.6	123.8	123.8	123.8	123.8	95.5	95.5	95.4	95.4	122.3	122.3	122.1	110.6
280	141.1	141.1	141.1	141.1	126.0	126.0	126.0	126.0	97.3	97.3	97.2	97.2	124.6	124.6	124.4	112.7
290	143.7	143.7	143.7	143.7	128.3	128.3	128.3	128.3	99.1	99.1	99.0	99.0	127.0	127.0	126.8	114.8
300	146.2	146.2	146.2	146.2	130.6	130.6	130.6	130.6	100.9	100.9	100.8	100.8	129.3	129.3	129.1	116.9

Appendix Table 8. Estimated Thermal Conductivity (10^{-3} Wm^{-1}K^{-1}) calculated from the Chung et al. method

Temp	**Dimethyl carbonate**				**Diethyl carbonate**				**Octanoic acid**				**Maleic acid**			
°C	PURE 36*	Exp	Cal	μ = 0	PURE 36*	Exp	Cal	μ = 0	PURE 36*	Exp	Cal	μ = 0	PURE 36*	Exp	Cal	μ = 0
0	8.78	8.78	8.78	8.78	8.17	8.17	8.17	8.17	7.56	7.56	7.58	7.58	7.00	7.00	6.95	6.36
10	9.33	9.33	9.33	9.33	8.71	8.71	8.71	8.71	8.04	8.04	8.06	8.06	7.36	7.36	7.31	6.68
20	9.90	9.90	9.90	9.90	9.27	9.27	9.27	9.27	8.54	8.54	8.56	8.56	7.74	7.74	7.69	7.03
30	10.49	10.49	10.49	10.49	9.85	9.85	9.85	9.85	9.06	9.06	9.08	9.08	8.13	8.13	8.09	7.39
40	11.09	11.09	11.09	11.09	10.45	10.45	10.45	10.45	9.60	9.60	9.61	9.61	8.55	8.55	8.50	7.76
50	11.72	11.72	11.72	11.72	11.07	11.07	11.07	11.07	10.15	10.15	10.15	10.15	8.97	8.97	8.93	8.15
60	12.35	12.35	12.35	12.35	11.71	11.71	11.71	11.71	10.71	10.71	10.71	10.71	9.42	9.42	9.38	8.55
70	13.01	13.01	13.01	13.01	12.36	12.36	12.36	12.36	11.29	11.29	11.29	11.29	9.88	9.88	9.84	8.96
80	13.68	13.68	13.68	13.68	13.03	13.03	13.03	13.03	11.87	11.87	11.87	11.87	10.35	10.35	10.32	9.39
90	14.36	14.36	14.36	14.36	13.71	13.71	13.71	13.71	12.47	12.47	12.47	12.47	10.84	10.84	10.80	9.83
100	15.06	15.06	15.06	15.06	14.41	14.41	14.41	14.41	13.09	13.09	13.08	13.08	11.34	11.34	11.30	10.28
110	15.77	15.77	15.77	15.77	15.12	15.12	15.12	15.12	13.71	13.71	13.70	13.70	11.85	11.85	11.82	10.74
120	16.49	16.49	16.49	16.49	15.84	15.84	15.84	15.84	14.34	14.34	14.33	14.33	12.37	12.37	12.34	11.21
130	17.22	17.22	17.22	17.22	16.58	16.58	16.58	16.58	14.99	14.99	14.97	14.97	12.90	12.90	12.87	11.69
140	17.96	17.96	17.96	17.96	17.32	17.32	17.32	17.32	15.64	15.64	15.62	15.62	13.44	13.44	13.41	12.18
150	18.71	18.71	18.71	18.71	18.08	18.08	18.08	18.08	16.30	16.30	16.28	16.28	13.99	13.99	13.96	12.68
160	19.47	19.47	19.47	19.47	18.85	18.85	18.85	18.85	16.97	16.97	16.95	16.95	14.54	14.54	14.52	13.18
170	20.23	20.23	20.23	20.23	19.62	19.62	19.62	19.62	17.65	17.65	17.63	17.63	15.11	15.11	15.08	13.68
180	21.01	21.01	21.01	21.01	20.41	20.41	20.41	20.41	18.34	18.34	18.31	18.31	15.67	15.67	15.65	14.20
190	21.79	21.79	21.79	21.79	21.20	21.20	21.20	21.20	19.03	19.03	19.01	19.01	16.25	16.25	16.23	14.71

Appendix Table 8 (continued)

200	22.58	22.58	22.58	22.58	22.01	22.01	22.01	22.01	19.74	19.74	19.71	19.71	16.83	16.83	16.80	15.24
210	23.38	23.38	23.38	23.38	22.82	22.82	22.82	22.82	20.45	20.45	20.42	20.42	17.41	17.41	17.39	15.76
220	24.18	24.18	24.18	24.18	23.63	23.63	23.63	23.63	21.17	21.17	21.14	21.14	17.99	17.99	17.97	16.29
230	24.99	24.99	24.99	24.99	24.46	24.46	24.46	24.46	21.89	21.89	21.86	21.86	18.58	18.58	18.56	16.82
240	25.80	25.80	25.80	25.80	25.29	25.29	25.29	25.29	22.63	22.63	22.59	22.59	19.18	19.18	19.15	17.36
250	26.62	26.62	26.62	26.62	26.13	26.13	26.13	26.13	23.37	23.37	23.33	23.33	19.77	19.77	19.75	17.89
260	27.45	27.45	27.45	27.45	26.97	26.97	26.97	26.97	24.11	24.11	24.08	24.08	20.37	20.37	20.34	18.43
270	28.27	28.27	28.27	28.27	27.82	27.82	27.82	27.82	24.87	24.87	24.83	24.83	20.97	20.97	20.94	18.97
280	29.11	29.11	29.11	29.11	28.67	28.67	28.67	28.67	25.62	25.62	25.59	25.59	21.57	21.57	21.54	19.52
290	29.94	29.94	29.94	29.94	29.53	29.53	29.53	29.53	26.39	26.39	26.36	26.36	22.17	22.17	22.14	20.06
300	30.78	30.78	30.78	30.78	30.40	30.40	30.40	30.40	27.16	27.16	27.13	27.13	22.78	22.78	22.74	20.60

Bibliography

1. Zimmerman, P. M. Single-Ended Transition State Finding with the Growing String Method. *J Comput Chem* 2015, 36, 601-11.

2. Zimmerman, P. Reliable Transition State Searches Integrated with the Growing String Method. *J. Chem. Theory Comput.* 2013, 9, 3043-3050.

3. Zimmerman, P. M. Growing String Method with Interpolation and Optimization in Internal Coordinates: Method and Examples. *J. Chem. Phys.* 2013, 138, 184102.

4. Odian, G. 4th ed.; John Wiley & Son, Inc: Hoboken, New Jersey, 2004; p 372.

5. Kostjuk, S. V. Recent Progress in the Lewis Acid Co-Initiated Cationic Polymerization of Isobutylene and 1, 3-Dienes. *RSC Advances* 2015, 5, 13125-13144.

6. Dimitrov, P.; Emert, J.; Faust, R. Polymerization of Isobutylene by Alcl3/Ether Complexes in Nonpolar Solvent. *Macromolecules* 2012, 45, 3318-3325.

7. Evans, A. G.; Meadows, G. W. The Polymerization of Isobutene by Boron Trifluoride. *Trans. Faraday Soc.* 1950, 46, 327-331.

8. Burrington, J. D.; Johnson, J. R.; Pudelski, J. K. Cationic Polymerization Using Heteropolyacid Salt Catalysts. *Top. Catal.* 2003, 23, 175-181.

9. Kennedy, J. P.; Gillham, J. K. In *Fortschritte Der Hochpolymeren-Forschung*, Springer: 1972; pp 1-33.

10. Kennedy, J. P. In *Novel Sequential Copolymers by Elucidating the Mechanism of Initiation and Termination of Carbocationic Polymerizations*, J. Polym. Sci., C Polym. symp., Wiley Online Library: 1976; pp 1-11.

11. Kennedy, J.; Squires, R. Fundamental Studies on Cationic Polymerization Iv—Homo-and Co-Polymerizations with Various Catalysts. *Polymer* 1965, 6, 579-587.

12. Liao, P.-Q.; Huang, N.-Y.; Zhang, W.-X.; Zhang, J.-P.; Chen, X.-M. Controlling Guest Conformation for Efficient Purification of Butadiene. *Science* 2017, 356, 1193.

13. Herm, Z. R.; Wiers, B. M.; Mason, J. A.; van Baten, J. M.; Hudson, M. R.; Zajdel, P.; Brown, C. M.; Masciocchi, N.; Krishna, R.; Long, J. R. Separation of Hexane Isomers in a Metal-Organic Framework with Triangular Channels. *Science* 2013, 340, 960.

14. Wang, G.; Sharp, C.; Plonka, A.; Wang, Q.; Frenkel, A.; Guo, W.; Hill, C.; Smith, C.; Kollar, J.; Troya, D. Mechanism and Kinetics for Reaction of the Chemical Warfare Agent Simulant, Dmmp (G), with Zirconium (Iv) Mofs: An Ultrahigh-Vacuum and Dft Study. *J. Phys. Chem. C* 2017, 121, 11261-11272.

15. Ruffley, J. P.; Goodenough, I.; Luo, T.-Y.; Richard, M.; Borguet, E.; Rosi, N. L.; Johnson, J. K. Design, Synthesis, and Characterization of Metal–Organic Frameworks for Enhanced Sorption of Chemical Warfare Agent Simulants. *J. Phys. Chem. C* 2019, 123, 19748-19758.

16. Tsonopoulos, C. An Empirical Correlation of Second Virial Coefficients. *AlChE J.* 1974, 20, 263-272.

17. Chung, T. H.; Ajlan, M.; Lee, L. L.; Starling, K. E. Generalized Multiparameter Correlation for Nonpolar and Polar Fluid Transport Properties. *Ind. Eng. Chem. Res.* 1988, 27, 671-679.

18. Calaminici, P.; Jug, K.; Köster, A. Density Functional Calculations of Molecular Polarizabilities and Hyperpolarizabilities. *J. Chem. Phys.* 1998, 109, 7756-7763.

19. Rashin, A.; Young, L.; Topol, I.; Burt, S. Molecular Dipole Moments Calculated with Density Functional Theory. *Chem. Phys. Lett.* 1994, 230, 182-188.

20. Kennedy, J. P.; Rengachary, S. In *Fortschritte Der Hochpolymeren-Forschung*, Springer: 1974; pp 1-48.

21. Chaffey-Millar, H.; Kühn, F. E. Quantum Chemical Insights into the Initiation Mechanism of Transition Metal Catalysed Polymerisation of Isobutene. *Appl. Catal., A* 2010, 384, 154-164.

22. Neese, F. The Orca Program System. *Wiley Interdiscip. Rev.: Comput. Mol. Sci.* 2012, 2, 73-78.

23. Perdew, J. P. Density-Functional Approximation for the Correlation Energy of the Inhomogeneous Electron Gas. *Phys. Rev. B* 1986, 33, 8822.

24. Weigend, F.; Ahlrichs, R. Balanced Basis Sets of Split Valence, Triple Zeta Valence and Quadruple Zeta Valence Quality for H to Rn: Design and Assessment of Accuracy. *PCCP* 2005, 7, 3297-3305.

25. Izsák, R.; Neese, F. An Overlap Fitted Chain of Spheres Exchange Method. *J. Chem. Phys.* 2011, 135, 144105.

26. Grimme, S.; Furche, F.; Ahlrichs, R. An Improved Method for Density Functional Calculations of the Frequency-Dependent Optical Rotation. *Chem. Phys. Lett.* 2002, 361, 321-328.

27. Ribeiro, R. F.; Marenich, A. V.; Cramer, C. J.; Truhlar, D. G. Use of Solution-Phase Vibrational Frequencies in Continuum Models for the Free Energy of Solvation. *J. Phys. Chem. B* 2011, 115, 14556-14562.

28. William, J. Process for the Production of Polyisobutylene. U.S. Patent 2,957,930, October 25, 1960.

29. Hariharan, P. C.; Pople, J. A. The Influence of Polarization Functions on Molecular Orbital Hydrogenation Energies. *Theor. Chim. Acta* 1973, 28, 213-222.

30. Francl, M. M.; Pietro, W. J.; Hehre, W. J.; Binkley, J. S.; Gordon, M. S.; DeFrees, D. J.; Pople, J. A. Self-Consistent Molecular Orbital Methods. Xxiii. A Polarization-Type Basis Set for Second-Row Elements. *J. Chem. Phys.* 1982, 77, 3654-3665.

31. Hutter, J.; Iannuzzi, M.; Schiffmann, F.; VandeVondele, J. Cp2k: Atomistic Simulations of Condensed Matter Systems. *Wiley Interdiscip. Rev.: Comput. Mol. Sci.* 2014, 4, 15-25.

32. VandeVondele, J.; Krack, M.; Mohamed, F.; Parrinello, M.; Chassaing, T.; Hutter, J. Quickstep: Fast and Accurate Density Functional Calculations Using a Mixed Gaussian and Plane Waves Approach. *Comput. Phys. Commun.* 2005, 167, 103-128.

33. Perdew, J. P.; Burke, K.; Ernzerhof, M. Generalized Gradient Approximation Made Simple. *Phys. Rev. Lett.* 1996, 77, 3865.

34. Goedecker, S.; Teter, M.; Hutter, J. Separable Dual-Space Gaussian Pseudopotentials. *Phys. Rev. B* 1996, 54, 1703.

35. Krack, M. Pseudopotentials for H to Kr Optimized for Gradient-Corrected Exchange-Correlation Functionals. *Theor. Chim. Acta* 2005, 114, 145-152.

36. VandeVondele, J.; Hutter, J. Gaussian Basis Sets for Accurate Calculations on Molecular Systems in Gas and Condensed Phases. *J. Chem. Phys.* 2007, 127, 114105.

37. Nosé, S. A Unified Formulation of the Constant Temperature Molecular Dynamics Methods. *J. Chem. Phys.* 1984, 81, 511-519.

38. Pepper, D. Ionic Polymerisation. *Q. Rev., Chem. Soc.* 1954, 8, 88-121.

39. Murthy, J. K.; Gross, U.; Rüdiger, S.; Rao, V. V.; Kumar, V. V.; Wander, A.; Bailey, C.; Harrison, N.; Kemnitz, E. Aluminum Chloride as a Solid Is Not a Strong Lewis Acid. *J. Phys. Chem. B* 2006, 110, 8314-8319.

40. . Air Filters for the Face. *Chemical & Engineering News Archive* 2014, 92, 34-38.

41. Bobbitt, N. S.; Mendonca, M. L.; Howarth, A. J.; Islamoglu, T.; Hupp, J. T.; Farha, O. K.; Snurr, R. Q. Metal–Organic Frameworks for the Removal of Toxic Industrial Chemicals and Chemical Warfare Agents. *Chem. Soc. Rev.* 2017, 46, 3357-3385.

42. Linders, M. J. G.; Baak, P. J.; van Bokhoven, J. J. G. M. Exploratory Investigation of the Risk of Desorption from Activated Carbon Filters in Respiratory Protective Devices. *Industrial & Engineering Chemistry Research* 2007, 46, 4034-4039.

43. Mondloch, J. E.; Katz, M. J.; Isley Iii, W. C.; Ghosh, P.; Liao, P.; Bury, W.; Wagner, G. W.; Hall, M. G.; DeCoste, J. B.; Peterson, G. W.; Snurr, R. Q.; Cramer, C. J.; Hupp, J. T.; Farha, O. K. Destruction of Chemical Warfare Agents Using Metal–Organic Frameworks. *Nature Materials* 2015, 14, 512-516.

44. Katz, M. J.; Brown, Z. J.; Colón, Y. J.; Siu, P. W.; Scheidt, K. A.; Snurr, R. Q.; Hupp, J. T.; Farha, O. K. A Facile Synthesis of Uio-66, Uio-67 and Their Derivatives. *Chem. Commun.* 2013, 49, 9449-9451.

45. Saleh, M.; Hofer, T. S. A Dftb/Mm Md Approach for Solid-State Interfaces: Structural and Dynamical Properties of H2o and Nh3 on R-Tio2 (001). *J. Phys. Chem. C* 2019, 123, 7230-7245.

46. Momeni, M. R.; Cramer, C. J. Computational Screening of Roles of Defects and Metal Substitution on Reactivity of Different Single- Vs Double-Node Metal–Organic Frameworks for Sarin Decomposition. *J. Phys. Chem. C* 2019, 123, 15157-15165.

47. Katz, M. J.; Mondloch, J. E.; Totten, R. K.; Park, J. K.; Nguyen, S. T.; Farha, O. K.; Hupp, J. T. Simple and Compelling Biomimetic Metal–Organic Framework Catalyst for the Degradation of Nerve Agent Simulants. *Angew. Chem. Int. Ed.* 2014, 53, 497-501.

48. Troya, D. Reaction Mechanism of Nerve-Agent Decomposition with Zr-Based Metal Organic Frameworks. *J. Phys. Chem. C* 2016, 120, 29312-29323.

49. Neese, F. The Orca Program System. *Wiley Interdisciplinary Reviews: Computational Molecular Science* 2012, 2, 73-78.

50. Nicklass, A.; Dolg, M.; Stoll, H.; Preuss, H. Ab Initio Energy-Adjusted Pseudopotentials for the Noble Gases Ne through Xe: Calculation of Atomic Dipole and Quadrupole Polarizabilities. *J. Chem. Phys.* 1995, 102, 8942-8952.

51. Hutter, J.; Iannuzzi, M.; Schiffmann, F.; VandeVondele, J. Cp2k: Atomistic Simulations of Condensed Matter Systems. *Wiley Interdisciplinary Reviews: Computational Molecular Science* 2014, 4, 15-25.

52. Krack, M. Pseudopotentials for H to Kr Optimized for Gradient-Corrected Exchange-Correlation Functionals. *Theoretical Chemistry Accounts: Theory, Computation, and Modeling (Theoretica Chimica Acta)* 2005, 114, 145-152.

53. Henkelman, G.; Jónsson, H. Improved Tangent Estimate in the Nudged Elastic Band Method for Finding Minimum Energy Paths and Saddle Points. *J. Chem. Phys.* 2000, 113, 9978-9985.

54. Henkelman, G.; Uberuaga, B. P.; Jónsson, H. A Climbing Image Nudged Elastic Band Method for Finding Saddle Points and Minimum Energy Paths. *J. Chem. Phys.* 2000, 113, 9901-9904.

55. Vo, M. N.; Basdogan, Y.; Derksen, B. S.; Proust, N.; Cox, G. A.; Kowall, C.; Keith, J. A.; Johnson, J. K. Mechanism of Isobutylene Polymerization: Quantum Chemical Insight into Alcl3/H2o-Catalyzed Reactions. *ACS Catal.* 2018, 8, 8006-8013.

56. De Vos, A.; Hendrickx, K.; Van Der Voort, P.; Van Speybroeck, V.; Lejaeghere, K. Missing Linkers: An Alternative Pathway to Uio-66 Electronic Structure Engineering. *Chem. Mater.* 2017, 29, 3006-3019.

57. Harvey, J. A.; Greathouse, J. A.; Sava Gallis, D. F. Defect and Linker Effects on the Binding of Organophosphorous Compounds in Uio-66 and Rare-Earth Mofs. *J. Phys. Chem. C* 2018, 122, 26889-26896.

58. Vieira Soares, C.; Maurin, G.; Leitão, A. A. Computational Exploration of the Catalytic Degradation of Sarin and Its Simulants by a Titanium Metal–Organic Framework. *J. Phys. Chem. C* 2019, 123, 19077-19086.

59. Bromley, L.; Wilke, C. Viscosity Behavior of Gases. *Ind. Eng. Chem. Fundam.* 1951, 43, 1641-1648.

60. Licht Jr, W.; Stechert, D. G. The Variation of the Viscosity of Gases and Vapors with Temperature. *J. Phys. Chem.* 1944, 48, 23-47.

61. Assael, M. J. In *The Importance of Thermophysical Properties in Optimum Design and Energy Saving*, Tokyo, Springer Japan: Tokyo, 2001; pp 162-178.

62. Groves, L.; Baker, J. 251. The Determination of Dipole Moments in the Vapour Phase. Part I. An Improved Apparatus. Part Ii. The Moments of Alkylbenzenes and Alkylcyclohexanes. *J. Chem. Soc. (Resumed)* 1939, 1144-1150.

63. Kubo, M. Studies on the Dielectric Constants of Gases and Vapours. I. *Sci. Papers Inst. Phys. Chem. Res. Tokyo* 1935, 26, 242-257.

64. Nelson Jr, R. D.; Lide Jr, D. R.; Maryott, A. A. *Selected Values of Electric Dipole Moments for Molecules in the Gas Phase*; National Standard Reference Data System: 1967.

65. Bak, K. L.; Gauss, J.; Helgaker, T.; Jørgensen, P.; Olsen, J. The Accuracy of Molecular Dipole Moments in Standard Electronic Structure Calculations. *Chem. Phys. Lett.* 2000, 319, 563-568.

66. Hickey, A. L.; Rowley, C. N. Benchmarking Quantum Chemical Methods for the Calculation of Molecular Dipole Moments and Polarizabilities. *J. Phys. Chem. A* 2014, 118, 3678-3687.

67. Adam, C.; Clark, S.; Ackland, G.; Crain, J. Conformation-Dependent Dipoles of Liquid Crystal Molecules and Fragments from First Principles. *Phys. Rev. E* 1997, 55, 5641.

68. O'Boyle, N. M.; Vandermeersch, T.; Flynn, C. J.; Maguire, A. R.; Hutchison, G. R. Confab - Systematic Generation of Diverse Low-Energy Conformers. *J. Cheminformatics* 2011, 3, 8.

69. Becke, A. D. Density-Functional Thermochemistry. Iii. The Role of Exact Exchange. *J. Chem. Phys.* 1993, 98, 5648-5652.

70. O'Boyle, N. M.; Banck, M.; James, C. A.; Morley, C.; Vandermeersch, T.; Hutchison, G. R. Open Babel: An Open Chemical Toolbox. *J. Cheminformatics* 2011, 3, 33.

71. Halgren, T. A. Mmff Vii. Characterization of Mmff94, Mmff94s, and Other Widely Available Force Fields for Conformational Energies and for Intermolecular-Interaction Energies and Geometries. *J. Comput. Chem.* 1999, 20, 730-748.

72. Poling, B. E.; Prausnitz, J. M.; O'Connell, J. P. In *The Properties of Gases and Liquids*, 4 ed.; McGraw-Hill Education: 1987; p 392.

73. Poling, B. E.; Prausnitz, J. M.; O'Connell, J. P. In *The Properties of Gases and Liquids*, 5 ed.; McGraw-Hill Education: 2000; pp 9.7-9.8.

74. Chung, T. H.; Lee, L. L.; Starling, K. E. Applications of Kinetic Gas Theories and Multiparameter Correlation for Prediction of Dilute Gas Viscosity and Thermal Conductivity. *Ind. Eng. Chem. Fundam.* 1984, 23, 8-13.

75. Poling, B. E.; Prausnitz, J. M.; O'Connell, J. P. In *The Properties of Gases and Liquids*, 5 ed.; McGraw-Hill Education: 2000; p 9.12.

76. Poling, B. E.; Prausnitz, J. M.; O'Connell, J. P. In *The Properties of Gases and Liquids*, 5 ed.; McGraw-Hill Education: 2000; pp 9.12-9.14.

77. Reichenberg, D., Dcs Report 11. National Physical Laboratory: Teddington, England, 1971.

78. Poling, B. E.; Prausnitz, J. M.; O'Connell, J. P. In *The Properties of Gases and Liquids*, 4 ed.; McGraw-Hill Education: 1987; pp 505, 523.

79. Johnson III, R. D.; NIST, E. Computational Chemistry Comparison and Benchmark Database. *NIST standard reference database* 2018, 101.

80. Kubo, M. Studies on the Dielectric Constants of Gases and Vapours. Vi. *Sci. Papers Inst. Phys. Chem. Res. Tokyo* 1936, 29, 169-179.

81. Okada, O. Conformational Analysis of Liquid Dimethyl Carbonate by Molecular Dynamics Calculations. *Mol. Phys.* 1998, 93, 153-158.

82. Reddy, S. K.; Balasubramanian, S. Liquid Dimethyl Carbonate: A Quantum Chemical and Molecular Dynamics Study. *J. Phys. Chem. B* 2012, 116, 14892-14902.

83. Bohets, H.; van der Veken, B. J. On the Conformational Behavior of Dimethyl Carbonate. *PCCP* 1999, 1, 1817-1826.

84. Poling, B. E.; Prausnitz, J. M.; O'Connell, J. P. In *The Properties of Gases and Liquids*, 5 ed.; McGraw-Hill Education: 2000; pp 9.10-9.11.

85. Pracht, P.; Bohle, F.; Grimme, S. Automated Exploration of the Low-Energy Chemical Space with Fast Quantum Chemical Methods. *PCCP* 2020.

86. Klamt, A.; Schuurmann, G. Cosmo: A New Approach to Dielectric Screening in Solvents with Explicit Expressions for the Screening Energy and Its Gradient. *Journal of the Chemical Society, Perkin Transactions 2* 1993, 799-805.

87. Ho, J.; Coote, M. L. First-Principles Prediction of Acidities in the Gas and Solution Phase. *Wiley Interdisciplinary Reviews: Computational Molecular Science* 2011, 1, 649-660.

88. Keith, J. A.; Carter, E. A. Quantum Chemical Benchmarking, Validation, and Prediction of Acidity Constants for Substituted Pyridinium Ions and Pyridinyl Radicals. *Journal of chemical theory and computation* 2012, 8, 3187-3206.